

Geometrical investigation on escape dynamics in the presence of dissipative and gyroscopic forces

Jun Zhong

Dissertation submitted to the Faculty of the
Virginia Polytechnic Institute and State University
in partial fulfillment of the requirements for the degree of

Doctor of Philosophy
in
Engineering Mechanics

Shane D. Ross, Chair
Lawrence N. Virgin
Raymond H. Plaut
Nicole Abaid
Pablo A. Tarazaga

February 17, 2020
Blacksburg, Virginia

Keywords: Escape dynamics, Invariant manifold, Transition tube, Transition ellipsoid,
Hamiltonian system, Dissipative system, Gyroscopic system
Copyright 2020, Jun Zhong

Geometrical investigation on escape dynamics in the presence of dissipative and gyroscopic forces

Jun Zhong

ABSTRACT

This dissertation presents innovative unified approaches to understand and predict the motion between potential wells. The theoretical-computational framework, based on the tube dynamics, will reveal how the dissipative and gyroscopic forces change the phase space structure that governs the escape (or transition) from potential wells.

In higher degree of freedom systems, the motion between potential wells is complicated due to the existence of multiple escape routes usually through an index-1 saddle. Thus, this dissertation firstly studies the local behavior around the index-1 saddle to establish the criteria of escape taking into account the dissipative and gyroscopic forces. In the analysis, an idealized ball rolling on a surface is selected as an example to show the linearized dynamics due to its special interests that the gyroscopic force can be easily introduced by rotating the surface. Based on the linearized dynamics, we find that the boundary of the initial conditions of a given energy for the trajectories that transit from one side of a saddle to the other is a cylinder and ellipsoid in the conservative and dissipative systems, respectively.

Compared to the linear systems, it is much more challenging or sometimes impossible to get analytical solutions in the nonlinear systems. Based on the analysis of linearized dynamics, the second goal of this study is developing a bisection method to compute the transition boundary in the nonlinear system using the dynamic snap-through buckling of a buckled beam as an example. Based on the Euler-Bernoulli beam theory, a two degree of freedom Hamiltonian system can be generated via a two mode-shape truncation. The transition boundary on the Poincaré section at the well can be obtained by the bisection method. The numerical results prove the efficiency of the bisection method and show that the amount of trajectories that escape from the potential well will be smaller if the damping of the system is increasing.

Finally, we present an alternative idea to compute the transition boundary of the nonlinear system from the perspective of the invariant manifold. For the conservative systems, the transition boundary of a given energy is the invariant manifold of a periodic orbit. The process of obtaining such invariant manifold comprises two parts, including the computation of the periodic orbit by solving a proper boundary-value problem (BVP) and the globalization of the manifold. For the dissipative systems, however, the transition boundary of a given energy becomes the invariant manifold of an index-1 saddle. We present a BVP approach using the small initial sphere in the stable subspace of the linearized system at one end and the energy at the other end as the boundary conditions. By using these algorithms, we obtain the nonlinear transition tube and transition ellipsoid for the conservative and dissipative systems, respectively, which are topologically the same as the linearized dynamics.

Geometrical investigation on escape dynamics in the presence of dissipative and gyroscopic forces

Jun Zhong

GENERAL AUDIENCE ABSTRACT

Transition or escape events are very common in daily life, such as the snap-through of plant leaves and the flipping over of umbrellas on a windy day, the capsize of ships and boats on a rough sea. Some other engineering problems related to escape, such as the collapse of arch bridges subjected to seismic load and moving trucks, and the escape and recapture of the spacecraft, are also widely known. At first glance, these problems seem to be unrelated. However, from the perspective of mechanics, they have the same physical principle which essentially can be considered as the escape from the potential wells. A more specific exemplary representative is a rolling ball on a multi-well surface where the potential energy is from gravity. The purpose of this dissertation is to develop a theoretical-computational framework to understand how a transition event can occur if a certain energy is applied to the system.

For a multi-well system, the potential wells are usually connected by saddle points so that the motion between the wells generally occurs around the saddle. Thus, knowing the local behavior around the saddle plays a vital role in understanding the global motion of the nonlinear system. The first topic aims to study the linearized dynamics around the saddle. In this study, an idealized ball rolling on both stationary and rotating surfaces will be used to reveal the dynamics. The effect of the gyroscopic force induced by the rotation of the surface and the energy dissipation will be considered.

In the second work, the escape dynamics will be extended to the nonlinear system applied to the snap-through of a buckled beam. Due to the nonlinear behavior existing in the system, it is hard to get the analytical solutions so that numerical algorithms are needed. In this study, a bisection method is developed to search the transition boundary. By using such method, the transition boundary on a specific Poincaré section is obtained for both the conservative and dissipative systems.

Finally, we revisit the escape dynamics in the snap-through buckling from the perspective of the invariant manifold. The treatment for the conservative and dissipative systems is different. In the conservative system, we compute the invariant manifold of a periodic orbit, while in the dissipative system we compute the invariant manifold of a saddle point. The computational process for the conservative system consists of the computation of the periodic orbit and the globalization of the corresponding manifold. In the dissipative system, the invariant manifold can be found by solving a proper boundary-value problem. Based on these algorithms, the nonlinear transition tube and transition ellipsoid in the phase space can be obtained for the conservative and dissipative systems, respectively, which are qualitatively the same as the linearized dynamics.

Acknowledgments

First of all, I would like to thank my advisor, Prof. Shane Ross, who is always there when I have questions, giving me help, addressing my concerns, and encouraging me when I doubt myself. He introduced me to the area of dynamical systems and escape dynamics, expanding my understanding about dynamics. I'm very grateful that he gave me tremendous free time and didn't put any pressure on my research which provides me a good opportunity to learn what I'm interested in. This experience solidifies my foundation to do independent study so that I can go further in my research career. I'm very proud of being a member of Ross Dynamics Lab.

I would also like to thank other committee members for the kind help, especially Prof. Raymond Plaut and Prof. Lawire Virgin for inspired discussion.

Thank you Engineering Mechanics Program for giving me the opportunity to be a member of this warm and sweet family; I got tremendous help and learned so much here. I want to extend the special thanks to Jessica Grimes, Lisa Smith, and Jody Humphreys for their continuous help. I also want to thank the colleagues for the wonderful discussion and assistance.

I also wish to thank my friends for the long term assistance: Fred and Mary Kay Eichelman, Steve and Stacy Wilkin, Bob and Carole Dellinger, to name but a few.

Finally, I would like to thank my parents for their unconditional love and encouragement, and my girlfriend, Bingqi Hou, for standing by my side, supporting and inspiring me. This thesis is dedicated to you all.

Contents

List of Figures	viii
1 Introduction	1
1.1 Escape and transition dynamics	1
1.2 Research Overview	3
Bibliography	5
2 Linearized dynamics for escape and transition in the presence of dissipative and gyroscopic forces	8
2.1 Introduction	9
2.2 Transition region for the conservative case	11
2.2.1 Boundary of transit and non-transit orbits	12
2.2.2 McGehee representation of the equilibrium region	15
2.3 Uncoupled system in the dissipative case: Ball rolling on a stationary surface	18
2.3.1 Analysis in the conservative system	23
2.3.2 Analysis in the dissipative system	27
2.3.3 Transition tube and transition ellipsoid	36
2.4 Coupled system in the dissipative case: Ball rolling on a rotating surface . .	39
2.4.1 Governing equations	39
2.4.2 Analysis in the conservative system	42
2.4.3 Analysis in the dissipative system.	46
2.4.4 Transition tube and transition ellipsoid	55

2.5	Conclusions and future work	56
	Bibliography	59
3	A tube dynamics perspective governing stability transitions: An example based on snap-through buckling	62
3.1	Introduction	63
3.2	The Paradigm: Snap-through of an Arch/Buckled Beam	64
3.3	Transition Tubes	74
3.3.1	Algorithm for computing transition tubes	74
3.3.2	Numerical results and discussion	77
3.4	Conclusions	83
	Bibliography	85
4	On the invariant manifold governing transition in snap-through buckling	88
4.1	Introduction	89
4.2	Algorithms for computing the invariant manifolds	91
4.2.1	Invariant manifold of a periodic orbit	91
4.2.2	Invariant manifold of an equilibrium point	93
4.3	Numerical results	96
4.3.1	Conservative systems	98
4.3.2	Dissipative systems	98
4.4	Conclusion	101
	Bibliography	102
5	Conclusion and future work	104
5.1	Summary	104
5.2	Future work	105
	Bibliography	107

List of Figures

2.1	The flow in the equilibrium region for the conservative system has the form saddle \times center. On the left is shown a schematic of the projection onto the (q_1, p_1) -plane, the saddle projection. For the conservative dynamics, the Hamiltonian function \mathcal{H}_2 remains constant at $h > 0$. Shown are the periodic orbit (black dot at the center), the asymptotic orbits (labeled A), two transit orbits (T) and two non-transit orbits (NT).	13
2.2	(a) The projection onto the (q_1, p_1) -plane, the saddle projection, with labels consistent with the text and (b) and (c). (b) The cross-section of the flow in the \mathcal{R} region of the energy surface. The north and south poles of bounding sphere n_i are labeled as N_i and S_i , respectively. (c) The McGehee representation of the flow on the boundaries of the \mathcal{R} region, highlighting the features on the bounding spheres n_1 and n_2 for $h > 0$	16
2.3	The graph of the example saddle surface considered, based on (2.12). The contours of the surface are projected on the bottom plane. The z direction is shown scaled by a factor of 2 compared to x and y in order to highlight the saddle nature of the surface.	19
2.4	The flow in the equilibrium region \mathcal{R} projected onto position space (\bar{q}_1, \bar{q}_2) in the conservative system with fixed positive energy, $\mathcal{H}_2 = h > 0$, for a ball rolling on a stationary surface. Shown are the unstable periodic orbit (vertical segment in the center), a typical asymptotic orbit winding onto the periodic orbit; two transit orbits (blue); and two non-transit orbits (red). At each point on the bounding lines n_1 or n_2 (dashed) inside the strip S , there is a wedge of velocity dividing different types of orbits, inside of which are transit orbits, and outside of which are non-transit orbits; specifically, the trajectories with initial conditions on the boundary are the orbits asymptotic to the unstable periodic orbit. See the text for the explanation of the details.	26

2.5	The flow in the equilibrium region for the dissipative system has the form saddle \times focus. On the left is shown the saddle projection onto the (q_1, p_1) -plane. The black dot at the origin represents focus-type asymptotic orbits with only a focus projection, thus oscillatory dynamics decaying towards the equilibrium point. The asymptotic orbits (labeled A) are the saddle-type asymptotic orbits which are tilted clockwise compared to the conservative system. They still form the separatrix between transit orbits (T) and non-transit orbits (NT). The hyperbolas, $q_1 p_1 = h/\lambda$, are no longer the boundary of trajectories with initial conditions on the bounding sphere (n_1 or n_2) due to the dissipation of the energy. The boundary of the shaded region are still the fastest trajectories with initial conditions on the bounding sphere, but are not strictly hyperbolas. Note that the saddle projection and focus projection are uncoupled in this dissipative system.	29
2.6	(a) The projection onto the (q_1, p_1) -plane, the saddle projection, with labels consistent with the text and (b) and (c). (b) The cross-section of the flow in the \mathcal{R} region of the energy surface. The north and south poles of bounding sphere n_i are labeled as N_i and S_i , respectively. (c) The McGehee representation of the flow in the region \mathcal{R}	31
2.7	The flow in the equilibrium region \mathcal{R} projected onto position space (\bar{q}_1, \bar{q}_2) in the dissipative system with fixed positive energy, $\mathcal{H}_2 = h > 0$, for a ball rolling on a stationary surface. Shown are different types of orbits as discussed in the text. Notice that due to the dissipation of energy, the periodic orbit in the conservative system does not exist, but is replaced by the initial conditions of initial energy h of the focus-type asymptotic orbits. Moreover, the strip for the conservative system—which is the position space projection of the tubes of transition at initial energy h —is replaced by the ellipse of transition. It means that the existence of transit orbits are constrained by the ellipse so that the wedge of velocity, determining the permissible direction of the transit orbits, only exists inside the ellipse. For a given fixed energy h , the wedge of velocity for the dissipative system is a subset of the wedge for the conservative system which is shown as a darker wedge.	35
2.8	Transition region boundary $\partial\mathcal{T}_h$ which is a tube (cylinder) for the conservative system of an idealized ball rolling on a stationary surface with initial energy h . The left figure shows the tube boundary (the ellipse) separating the transit and non-transit orbits on the Poincaré section Σ , where the dots are the initial conditions for the corresponding trajectories. The right figure shows the transition tube for a given energy. The critical surface divides the transition tubes into two parts whose left part gives the initial conditions for orbits transitioning to the right, and right part gives the initial conditions for orbits transitioning to the left. Some trajectories are given to show how the transition tube controls the transition whose initial conditions are shown as dots on the left Poincaré section with the same color.	37

2.9	Transition ellipsoid for the dissipative system of a rolling ball on a stationary surface. The left figure shows the Poincaré section Σ , where the dots are the initial conditions for the corresponding trajectories with the same color in the right figure and the solid ellipse is the set of initial conditions for saddle-type asymptotic orbits. For comparison, the dashed ellipse of the tube boundary for the conservative system with the same energy h is also given. On the right is the ellipsoid giving the initial conditions for all transit orbits. The critical surface divides the ellipsoid into two parts. Each side of the ellipsoid gives the initial conditions of transit orbits passing through the critical surface to the other side. In this figure, SA and FA denote the saddle-type and focus-type asymptotic orbits, respectively.	38
2.10	Inertial and rotating frames. The rotating coordinate system of x and y axes moves counterclockwise with constant angular velocity ω relative to the inertial frame with X and Y axes. The z axis coincides with the Z axis which is pointing out of the plane and is not shown here. We denote the unit vectors along x, y, z by $\mathbf{e}_1, \mathbf{e}_2$ and \mathbf{e}_3 , respectively. . . .	40
2.11	The flow in the equilibrium region \mathcal{R} projected onto position space (\bar{q}_1, \bar{q}_2) in the conservative system with fixed positive energy, $\mathcal{H}_2 = h > 0$, for a ball rolling on a rotating surface. Shown are the periodic orbit acting as an ellipse; one asymptotic orbit gradually approaching the periodic orbit; two transit orbits; and two non-transit orbits, one starting inside the strips and the other outside the strips. Note that the dynamic behavior in the position space is identical to those in the circular restricted three-body problem [15, 16].	44
2.12	The flow in the equilibrium region \mathcal{R} projected onto (q_1, p_1) plane and (q_2, p_2) plane which are coupled has form saddle \times focus. Shown are the saddle-type asymptotic orbits (labeled A), transit orbits (labeled T) and non-transit orbits (labeled NT). The dot at the origin of (q_1, p_1) plane is the focus-type asymptotic orbits with projection only on (q_2, p_2) plane which is a damped oscillator decaying to the origin. Due to the coupling between (q_1, p_2) plane and (q_2, p_2) plane, the initial conditions for the three-dimensional stable asymptotic orbit are dependent on the angle in focus projection. The one dimensional unstable asymptotic orbits are a straight line in the saddle projection.	50
2.13	The McGehee representation of the equilibrium region for dissipative system of rolling ball on a rotating surface. (a) The projection of flow onto (q_1, p_1) plane. (b) The projection of the flow in the \mathcal{R} region of the energy surface onto a cross-section. (c) The McGehee representation of the flow on the boundaries of the \mathcal{R} region, highlighting the features on the bounding spheres n_1 and n_2 , the “inner” and “outer” spheres, respectively.	51
2.14	The flow in the equilibrium region \mathcal{R} of position space. Shown are the saddle-type asymptotic orbit; two transit orbits; three non-transit orbits. For the same given energy, the wedges of velocity for the dissipative system (the smaller light grey shaded wedges), restricted by the ellipse of transition, partially cover the wedges of velocity for the conservative system (the larger dark grey shaded wedges) restricted by a strip.	54

2.15	Transition tube for the ball rolling on a rotating surface. The left figure gives the region for initial conditions of transit orbits on the Poincaré section Σ with three initial conditions (the dots) for three types of orbits. The right shows the transition tube for a given energy. The critical surface playing the same role as the ball rolling on a stationary surface also exists here. Three types of orbits with initial conditions on the left figure are given. . . .	55
2.16	Transition ellipsoid for the dissipative system in the rolling ball on a rotating surface. The left figure shows the Poincaré section Σ , where the dots are the initial conditions for the corresponding trajectories and the solid ellipse is the boundary of initial conditions for the transit orbits. For comparison, the dashed ellipse of tube boundary for the conservative system is also given. The right figure shows the transition tube with three different types of orbits with initial conditions on the left figure.	57
3.1	(a) A schematic load-deflection characteristic, (b) the two dominant degrees of freedom. .	65
3.2	Contours of potential energy: (a) the symmetric system, $\gamma_1 = \gamma_2 = 0$, (b) with small initial imperfections in both modes, i.e., γ_1 and γ_2 are nonzero.	70
3.3	For a representative energy above the saddle point S_1 , we show the unstable periodic orbit in the neck region around S_1 . It projects to a single line going between the upper and lower energy boundary curves, and arrows are shown for convenience. We show the Poincaré sections Σ_1 and Σ_2 which are defined by X values equal to that of the two stable equilibria in the center of the left and right side wells, W_1 and W_2 , respectively. The arrows on the vertical lines indicate that these Poincaré sections are also defined by positive X momentum.	75
3.4	A transition tube from the left well to the right well, obtained using the method described in the text. The upper figure shows the configuration space projection. The lower left shows the tube boundary (closed curve) on Poincaré section Σ_1 , which separates transit and non-transit trajectories. The lower right shows the corresponding tube boundary (closed curve) on Poincaré section Σ_2	78
3.5	A transition tube from the left well to the right well, obtained using the method described in the text, for the case of damping. The upper figure shows the configuration space projection. The lower left shows the tube boundary (closed curve) on Poincaré section Σ_1 which separates transit and non-transit trajectories for initial conditions all with a given fixed initial energy. The lower right shows the corresponding image under the flow on Poincaré section Σ_2 . Due to the damping, and a range of times spent in the neck region, spiraling is visible in this 2D projection since trajectories which spend longer in the neck will be at lower total energies. Compare with Figure 3.4.	79
3.6	A transition tube from the left side boundary (n_1) to the right side boundary (n_2) of the equilibrium region around saddle point S_1 , obtained for the linear damped system. Notice that the shrinking of the tube is observed as in the nonlinear system, Figure 3.5, here seen in terms of the width of the projected strip onto configuration space.	80

3.7	The effect of the damping coefficient C_H on the area of the transition tube on Poincaré section Σ_1 is shown. For a fixed initial energy above the saddle, the projection on the canonical plane (Y, p_Y) is shown in (a) and the area is plotted in (b). In (b), the shaded region indicates the experimentally observed range of damping coefficients, which correspond to non-dimensional damping factor ξ_d less than 5%.	81
3.8	Several example trajectories are shown, starting from the stable well point W_1 . The initial conditions from Poincaré section Σ_1 are shown in (a) for a fixed initial energy, along with the transition tube boundaries for the conservative case and a damped case. In (b), we show the trajectories for points A and B, for the conservative case where A is just outside the tube boundary and B is just inside. In (c), we show the trajectories for points B and C, for the damped case where B is just outside the tube boundary and C is just inside. In (d), we illustrate the effect of damping by starting the same initial condition, B, but showing the trajectory in the conservative case as trajectory B and the damped case as trajectory B'.	82
4.1	Illustration of selecting an extra Poincaré section to reduce the two-parameter continuation to a one-parameter continuation: (a) Select the initial condition of the fastest trajectory on the initial sphere (with radius r_0) in the stable subspace of the linearized system and numerically integrate the nonlinear equations until the trajectory reaches the given energy h . For the selection of the points, the easiest way is meshing by arc-length. Of course, for the area with large curvature, more points can be selected; (2) Select some points on the fastest trajectory and compute the tangent vector at each point along the fastest trajectory; (3) Finally the plane normal to the tangent vector at each point can be selected as the Poincaré section; (4) After we determine the Poincaré sections, we can obtain the intersection of the fastest trajectory on one Poincaré section, labeled by A. In general point A has lower energy than the given energy h . We can fix p_Y and commit the continuation along Y direction until the Hamiltonian reaches h so that we can obtain point B on the transition boundary. Then we can use Point B as the starting solution and do the continuation by fixing the Hamiltonian as h by which we can obtain the transition boundary on the Poincaré section.	96
4.2	A transition tube from the left well to the right well in the conservative system obtained by the BVP approach: (a) shows the transition tube projected onto configuration space. (b) and (c) give the transition boundaries on the Poincaré sections Σ_1 and Σ_2 in the conservative systems. In order to compare the efficiency of the current method, we also present the transition boundary obtained by the bisection method.	97

4.3	Transition ellipsoids in dissipative system obtained by the BVP approach: (a) and (c) show the three-dimensional transition ellipsoids with excess energy $\Delta E = 1.0 \times 10^{-4}$ J and $\Delta E = 2.0 \times 10^{-4}$ J, respectively; (b) and (d) show the corresponding configuration space projections.	99
4.4	A transition ellipsoid in the dissipative system obtained by the BVP approach: the right figure shows the transition ellipsoid; the lower left shows the configuration space projection; the upper left shows the transition boundary, a closed curve, on the Poincaré section Σ_1 which separates the initial conditions with a given fixed energy for the transit and non-transit trajectories. A transit orbit and a non-transit trajectory starting with initial conditions labeled by A and B are shown, which are inside and outside of the transition boundary on the Poincaré section Σ_1 , respectively.	100

Chapter 1

Introduction

1.1 Escape and transition dynamics

Transition events are very common in both the natural world, daily life, and even industrial applications. Examples of transition are the snap-through of plant leaves and engineering structures responding to stimuli [1, 2], the flipping over of umbrellas on a windy day, reaction rates in chemical reaction dynamics [3], the escape and recapture of comets and spacecraft in celestial mechanics [4, 5, 6], and the capsize of ships [7, 8]. Better understanding and prediction of transitions, or escape, have significance in both utilization and evasion of such events, such as how to transfer spacecraft in specific space missions from one prescribed initial orbit to a desired final orbit with lower energy, or in structural mechanics, how to avoid the collapse of structures. From the perspective of mechanics, such behavior can be interpreted as the escape from one local minimum of potential energy (i.e., a potential well) to another, which has been widely studied as ‘escape dynamics’ [9, 10, 11, 12, 13]. Escape in a one degree of freedom system, like a double-well oscillator, is unambiguous, as the phase space is two dimensional and the hilltop equilibrium becomes a saddle point in phase space. The only way the system state can escape from the potential energy minimum is by passing over the hilltop to another local minimum. Therefore, all trajectories which have an energy above that of the hilltop, as evaluated as they pass through the location of the hilltop, transit from one side to the other. This situation has been studied by both experiments and theory with good agreement between the two [14, 15, 16]. Higher degree of freedom systems, however, are more complicated since there are multiple paths to transition through

an index-1 saddle equilibrium point, as the phase space is now four dimensions or more. For such systems, it is of importance to establish systematic methods and criteria to predict the escape from a potential well.

Generally, escape can occur only when the system has energy higher than the escape energy which is the critical energy that allows escape, the energy of the saddle point [2, 8, 11, 12]. If the energy is lower than the escape energy, the zero velocity curve (or surface)—which is the boundary of the projection of the energy manifold onto position space—is closed, allowing no open neck region around the saddle point. In this case, all of the trajectories are bounded to only evolve within their potential wells of origin and no trajectory can escape from the well. For initial conditions with energy higher than the escape energy, the equipotential surfaces open around the saddle point in a neck region, and trajectories have a chance to escape the potential well to another or even to infinity. However, the energy criterion alone is not sufficient to guarantee escape. The dynamic boundary between transition and non-transition of a system with energy higher than critical energy can be thoroughly understood under the conceptual framework of transition dynamics or sometimes known as tube dynamics [2, 8, 17, 18, 19]. In conservative two degrees of freedom systems with energy higher than the critical energy, there is an unstable periodic orbit in the bottleneck region. Emanating from the periodic orbit are its stable and unstable manifolds which have cylindrical or “tube” geometry within the conserved energy manifold. The tube manifold, sometimes called a transition tube in tube dynamics, consists of pieces of asymptotic orbits. As stated in [10], the best systematic way to study the escape from such a system is by calculating the asymptotic orbits of the periodic orbit. The reason is that the transition tube, acting like a separatrix, separates two distinct types of orbits: transit orbits and non-transit orbits. Transit orbits are those inside of the tube which can escape from one potential well to another, while non-transit, those outside of the tube, cannot pass through the bottleneck region, and thus return to their region of origin.

The algorithms for computing the transition tubes for the conservative system are relatively well developed [6]. The general process is first computing the periodic orbits, and then globalizing the corresponding invariant manifold. As for the computation of the periodic orbit, there are many advanced methods. Of course, there are some other approaches which do not compute the periodic orbit, but directly compute the invariant set and invariant manifold, such as GAIO [20], cell mapping [21] and Lagrangian descriptor [22], et al. However, the study about the transition boundary in the dissipative systems are still lacking. We even

just know little about the geometry of the phase space structure that governs the transition, not to mention the algorithm for computing such boundaries. In this dissertation, we focus on two degree of freedom systems, an intermediate situation, to develop the algorithms for computing the transition boundary and consider the effect of dissipative and gyroscopic forces both in isolation and in combination. We take a Hamiltonian point of view and use canonical Hamiltonian variables, even when dissipation is included.

1.2 Research Overview

This dissertation comprises three topics, aiming to develop theoretical and computational tools to understand and predict the escape and transition events.

In Chapter 2, we study the local dynamics near a saddle point using the idealized ball rolling on a saddle surface as an example to study the escape dynamics in the presence of dissipative and gyroscopic forces. The system can be either an inertial system or gyroscopic system, depending on whether the surface is stationary or rotating. It reveals, both theoretically and computationally, that the boundary of the initial conditions for the escape trajectories in dissipative systems is governed by a $(2N - 2)$ -dimensional hyper-ellipsoid in $2N$ -dimensional dynamical systems which is the first time such criteria have been found in the geometric theory of transition dynamics.

In Chapter 3, we develop a bisection-based algorithm to compute the transition boundary. The computational algorithm is applied to the snap-through of a shallow arch. Based on the Euler-Bernoulli beam theory, the governing partial differential equations of the shallow arch are derived which then are converted to a two-degree of freedom Hamiltonian system via a two-mode truncation. Using the results from the linearization around the rank-1 saddle as approximations, the transition tubes for both conservative and dissipative systems in the nonlinear text can be obtained by the bisection method. This framework can be applied to both conservative and dissipative systems.

In Chapter 4, we present a new idea of translating the computation of the invariant manifolds into a two-point boundary value problem (BVP) to determine the transition boundary. For the conservative system, we get the transition boundary by computing the invariant manifold of a periodic orbit. For the dissipative system, we get the transition boundary by computing the invariant manifold of a rank-1 saddle by BVP approach where the boundary conditions

at one end lay on a hyper-sphere (or hyper-ellipsoid) with a small radius in the stable and unstable subspaces of the linearized system about the rank-1 saddle, while the boundary conditions at the other end are determined by the given energy and the position in the phase space. The computation is implemented via an off-the-shelf numerical continuation package Continuation Core and Toolboxes (COCO) [23]. The topological transition tube and transition ellipsoid that governs the initial conditions of escape trajectories of a given energy in the conservative and dissipative systems are obtained which is qualitatively the same as those in the linearized dynamics.

Bibliography

- [1] L. N. Virgin, Y. Guan, R. H. Plaut, On the geometric conditions for multiple stable equilibria in clamped arches, *International Journal of Non-Linear Mechanics* 92 (2017) 8–14.
- [2] J. Zhong, L. N. Virgin, S. D. Ross, A tube dynamics perspective governing stability transitions: An example based on snap-through buckling, *International Journal of Mechanical Sciences* 149 (2018) 413–428.
- [3] S. Wiggins, L. Wiesenfeld, C. Jaffé, T. Uzer, Impenetrable barriers in phase-space, *Physical Review Letters* 86 (24) (2001) 5478.
- [4] C. Jaffé, S. D. Ross, M. W. Lo, J. Marsden, D. Farrelly, T. Uzer, Statistical theory of asteroid escape rates, *Physical Review Letters* 89 (1) (2002) 011101.
- [5] W. S. Koon, M. W. Lo, J. E. Marsden, S. D. Ross, Heteroclinic connections between periodic orbits and resonance transitions in celestial mechanics, *Chaos* 10 (2000) 427–469.
- [6] W. S. Koon, M. W. Lo, J. E. Marsden, S. D. Ross, *Dynamical Systems, the Three-Body Problem and Space Mission Design*, Marsden Books, ISBN 978-0-615-24095-4, 2011.
- [7] M. S. Soliman, J. M. T. Thompson, Transient and steady state analysis of capsizing phenomena, *Applied Ocean Research* 13 (2) (1991) 82–92.
- [8] S. Naik, S. D. Ross, Geometry of escaping dynamics in nonlinear ship motion, *Communications in Nonlinear Science and Numerical Simulation* 47 (2017) 48 – 70, ISSN 1007-5704.

- [9] H. Waalkens, A. Burbanks, S. Wiggins, Efficient procedure to compute the microcanonical volume of initial conditions that lead to escape trajectories from a multidimensional potential well, *Physical Review Letters* 95 (8) (2005) 084301.
- [10] G. Contopoulos, *Order and Chaos in Dynamical Astronomy*, Springer Science & Business Media, 2013.
- [11] E. E. Zotos, Escapes in Hamiltonian systems with multiple exit channels: Part I, *Nonlinear Dynamics* 78 (2) (2014) 1389–1420.
- [12] E. E. Zotos, An overview of the escape dynamics in the Hénon-Heiles Hamiltonian system, *Meccanica* 52 (11-12) (2017) 2615–2630.
- [13] R. Barrio, F. Blesa, S. Serrano, Bifurcations and safe regions in open Hamiltonians, *New Journal of Physics* 11 (5) (2009) 053004.
- [14] J. A. Gottwald, L. N. Virgin, E. H. Dowell, Routes to escape from an energy well, *Journal of Sound and Vibration* 187 (1) (1995) 133–144.
- [15] L. N. Virgin, *Introduction to Experimental Nonlinear Dynamics*, Cambridge University Press, 2000.
- [16] B. P. Mann, Energy criterion for potential well escapes in a bistable magnetic pendulum, *Journal of Sound and Vibration* 323 (3) (2009) 864–876.
- [17] F. Gabern, W. S. Koon, J. E. Marsden, S. D. Ross, T. Yanao, Application of tube dynamics to non-statistical reaction processes, *Few-Body Systems* 38 (2006) 167–172.
- [18] S. D. Ross, *Cylindrical manifolds and tube dynamics in the restricted three-body problem*, Ph.D. thesis, California Institute of Technology, 2004.
- [19] K. Onozaki, H. Yoshimura, S. D. Ross, Tube dynamics and low energy Earth-Moon transfers in the 4-body system, *Advances in Space Research* 60 (2017) 2117–2132.
- [20] M. Dellnitz, G. Froyland, O. Junge, The algorithms behind GAIOSet oriented numerical methods for dynamical systems, in: *Ergodic theory, analysis, and efficient simulation of dynamical systems*, Springer, 145–174, 2001.
- [21] C. S. Hsu, A theory of cell-to-cell mapping dynamical systems, *Journal of Applied Mechanics* 47 (4) (1980) 931–939.

- [22] A. M. Mancho, S. Wiggins, J. Curbelo, C. Mendoza, Lagrangian descriptors: A method for revealing phase space structures of general time dependent dynamical systems, *Communications in Nonlinear Science and Numerical Simulation* 18 (12) (2013) 3530–3557.
- [23] H. Dankowicz, F. Schilder, *Recipes for continuation*, vol. 11, SIAM, 2013.

Chapter 2

Linearized dynamics for escape and transition in the presence of dissipative and gyroscopic forces

Attribution

This chapter represents part of a collaborative work with Shane D. Ross which is published in the *Communications in Nonlinear Science and Numerical Simulation*, 82 (2020), 105033. The online version of the article can be found at <https://doi.org/10.1016/j.cnsns.2019.105033>.

Abstract

Escape from a potential well can occur in different physical systems, such as capsizing of ships, resonance transitions in celestial mechanics, and dynamic snap-through of arches and shells, as well as molecular reconfigurations in chemical reactions. The criteria and routes of escape in one-degree of freedom systems has been well studied theoretically with reasonable agreement with experiment. The trajectory can only transit from the hilltop of the one-dimensional potential energy surface. The situation becomes more complicated when the system has higher degrees of freedom since it has multiple routes to escape through an

equilibrium of saddle-type, specifically, an index-1 saddle. This chapter studies the geometry of escape across a saddle in the idealized rolling ball on a surface and establishes the criteria of escape providing both a methodology and results under the conceptual framework known as tube dynamics. This system can be classified into two categories based on whether the saddle projection and focus projection in the symplectic eigenspace are coupled or not when damping and/or gyroscopic effects are considered. For simplicity, only the linearized system around the saddle points is analyzed, but the results generalize to the nonlinear system. We define a transition region, \mathcal{T}_h , as the region of initial conditions of a given initial energy h which transit from one side of a saddle to the other. We find that in conservative systems, the boundary of the transition region, $\partial\mathcal{T}_h$, is a cylinder, while in dissipative systems, $\partial\mathcal{T}_h$ is an ellipsoid.

2.1 Introduction

We have made it clear that the phase space structure, known as a transition tube, governs the escape in conservative systems of two degrees of freedom. The transition tube is the stable invariant manifold emanating from a periodic orbit around an index-1 saddle. The transition tube separates the two distinct types of orbits: transit orbits and non-transit orbits corresponding to escape and non-escape. However, the conservative system is just an ideal case since energy fluctuations and dissipation cannot be avoided in the real world. Thus, it is natural to consider how the situation will change if dissipative forces are considered. In this chapter, we continue this study and answer in more detail the concern of how the situation changes when dissipation is present, finding that the transition tube in the conservative system becomes a transition ellipsoid in the dissipative system.

On the other hand, when the system is rotating or magnetic forces are present, gyroscopic forces must be considered. Gyroscopic forces, widely found in rotating systems [1, 2, 3, 4, 5] as well as electromagnetic systems, are non-dissipative and the gyroscopic coefficients enter the equations of motion in a skew-symmetric manner [1]. Some researchers have studied escape in conservative gyroscopic systems (e.g., [6, 7]). There exist transition tubes controlling the escape which are topologically the same as in an inertial system [8, 9, 10]. However, to the best knowledge of the authors, no study has been carried out to study the escape in systems with *both* dissipative and gyroscopic forces present. In fact, gyroscopic systems are interesting due to some unexpected phenomena which have some uncommon features. In conservative

gyroscopic systems, motion near an unstable point of the potential energy surface, such as an index-1 saddle point, can be stabilized via gyroscopic forces, e.g., rotation with large enough angular velocity [4, 5, 11, 12]. But small dissipation can make the system lose the stability which is called dissipation-induced instability [3], different from the common notion that dissipation makes a system more stable. Considering this difference in dynamical behavior, another concern is whether the dynamical behavior of the dissipative system will be the same if the gyroscopic forces are included. This study will also partially answer this concern.

In this chapter, we will establish criteria and present methods to estimate the transition in two degrees of freedom. The focus of this analysis is on the local behavior near the neck region around the saddle point, obtained via the linearized dynamics. The corresponding global behavior is discussed in the following chapters. In such linearized systems, the equilibrium point is of type saddle \times center in the conservative system (i.e., an index-1 saddle) which becomes a saddle \times focus when dissipation is considered. In other words, the equilibrium point changes from one with a one-dimensional stable, one-dimensional unstable, and two-dimensional center manifold, to one with a three-dimensional stable and one-dimensional unstable manifold. To compare the similarities and differences between the conservative and dissipative system in each setting, we introduce the same change of variables that uses the generalized eigenvectors of the corresponding conservative system, which we refer to as the *symplectic eigenspace*.

In the symplectic eigenspace, the dynamics in the saddle and focus projections are coupled for some dissipative systems, while for others, they remain uncoupled. Ref. [13] classified different systems into two categories depending on the resulting linear coupling between the saddle and focus variables of the transformed dissipative system. Those systems are: an idealized rolling ball on both stationary and rotating saddle surfaces, the pitch and roll dynamics of a ship near the capsize state with equal and unequal damping, the snap-through of a shallow arch, and potential well transitions in the planar circular restricted three-body problem (PCR3BP). The example problems considered share the same dynamic behavior so that we only need to give the full analysis for just one as an exemplar representative. Among the problems we discussed in [13], the idealized ball rolling on a saddle surface is of special interest since it can be either an inertial system or gyroscopic system, depending on whether the surface is stationary or rotating so that it can have the properties of both types of problems. Thus, we will focus on analyzing the idealized ball rolling on a surface in this chapter, where the rotation is about the saddle point itself. The other examples will be

shown to be equivalent to a standard form derived for the idealized ball rolling on a surface. The readers are referred to [13] for more details.

2.2 Transition region for the conservative case

A linear two degrees of freedom conservative system with a saddle-center type equilibrium point (i.e., index-1 or rank-1 saddle) [8, 9, 14, 15, 16] can be transformed via a canonical transformation to normal form coordinates (q_1, q_2, p_1, p_2) such that the quadratic Hamiltonian, \mathcal{H}_2 , can be written in the normal form,

$$\mathcal{H}_2 = \lambda q_1 p_2 + \frac{1}{2} \omega_p (q_2^2 + p_2^2), \quad (2.1)$$

where q_i and p_i are the generalized coordinates and corresponding momenta. The Hamiltonian equations are defined as

$$\dot{q}_i = \frac{\partial \mathcal{H}_2}{\partial p_i}, \quad \dot{p}_i = -\frac{\partial \mathcal{H}_2}{\partial q_i}, \quad (2.2)$$

which yields the following equations of motion,

$$\begin{aligned} \dot{q}_1 &= \lambda q_1, & \dot{p}_1 &= -\lambda p_1, \\ \dot{q}_2 &= \omega_p p_2, & \dot{p}_2 &= -\omega_p q_2, \end{aligned} \quad (2.3)$$

where the dot over the variable denotes the derivative with respect to time. In the above equations, λ is the real eigenvalue corresponding to the saddle coordinates spanned by (q_1, p_1) and ω_p is the frequency associated with the center coordinates (q_2, p_2) . The solutions can be written as,

$$\begin{aligned} q_1 &= q_1^0 e^{\lambda t}, & p_1 &= p_1^0 e^{-\lambda t}, \\ q_2 + ip_2 &= (q_2^0 + ip_2^0) e^{-i\omega_p t}. \end{aligned} \quad (2.4)$$

Note that,

$$f_1 = q_1 p_1, \quad f_2 = q_2^2 + p_2^2 \quad (2.5)$$

are two independent constants of motion under the Hamiltonian system (2.1) with \mathcal{H}_2 itself trivially a constant of motion.

2.2.1 Boundary of transit and non-transit orbits

The linearized phase space. For positive h and c , the equilibrium or bottleneck region \mathcal{R} (sometimes just called the neck region), which is determined by,

$$\mathcal{H}_2 = h, \quad \text{and} \quad |p_1 - q_1| \leq c,$$

where $c > 0$, is homeomorphic to the product of a 2-sphere and an interval $I \in \mathbb{R}$, $S^2 \times I$; namely, for each fixed value of $p_1 - q_1$ in the interval $I = [-c, c]$, we see that the equation $\mathcal{H}_2 = h$ determines a 2-sphere,

$$\frac{\lambda}{4}(q_1 + p_1)^2 + \frac{1}{2}\omega_p(q_2^2 + p_2^2) = h + \frac{\lambda}{4}(p_1 - q_1)^2. \quad (2.6)$$

Suppose $a \in I$, then (2.6) can be re-written as,

$$x_1^2 + q_2^2 + p_2^2 = r^2, \quad (2.7)$$

where $x_1 = \sqrt{\frac{1}{2}\frac{\lambda}{\omega_p}}(q_1 + p_1)$ and $r^2 = \frac{2}{\omega_p}(h + \frac{\lambda}{4}a^2)$, which defines a 2-sphere of radius r in the three variables x_1 , q_2 , and p_2 .

The bounding 2-sphere of \mathcal{R} for which $p_1 - q_1 = c$ will be called n_1 (the “left” bounding 2-sphere), and where $p_1 - q_1 = -c$, n_2 (the “right” bounding 2-sphere). Therefore, $\partial\mathcal{R} = \{n_1, n_2\}$. See Figure 2.1.

We call the set of points on each bounding 2-sphere where $q_1 + p_1 = 0$ the equator, and the sets where $q_1 + p_1 > 0$ or $q_1 + p_1 < 0$ will be called the northern and southern hemispheres, respectively.

The linear flow in \mathcal{R} . To analyze the flow in \mathcal{R} , consider the projections on the (q_1, p_1) -plane and the (q_2, p_2) -plane, respectively. In the first case we see the standard picture of a saddle point in two dimensions, and in the second, of a center consisting of harmonic oscillator motion. Figure 2.1 schematically illustrates the flow. With regard to the first projection we see that \mathcal{R} itself projects to a set bounded on two sides by the hyperbolas $q_1 p_1 = h/\lambda$ (corresponding to $q_2^2 + p_2^2 = 0$, see (2.1)) and on two other sides by the line segments $p_1 - q_1 = \pm c$, which correspond to the bounding 2-spheres, n_1 and n_2 , respectively.

Since $q_1 p_1$ is an integral of the equations in \mathcal{R} , the projections of orbits in the (q_1, p_1) -plane

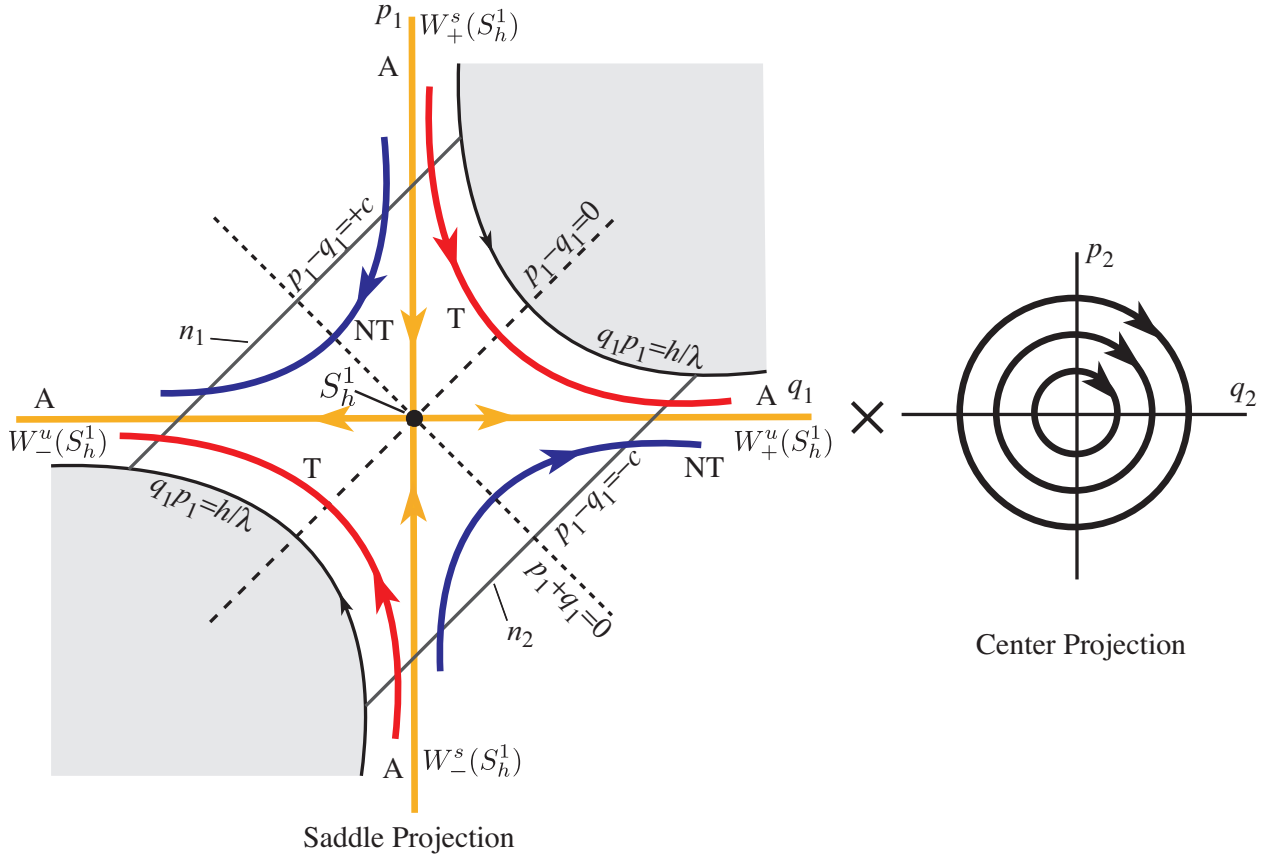


Figure 2.1: The flow in the equilibrium region for the conservative system has the form saddle \times center. On the left is shown a schematic of the projection onto the (q_1, p_1) -plane, the saddle projection. For the conservative dynamics, the Hamiltonian function \mathcal{H}_2 remains constant at $h > 0$. Shown are the periodic orbit (black dot at the center), the asymptotic orbits (labeled A), two transit orbits (T) and two non-transit orbits (NT).

move on the branches of the corresponding hyperbolas $q_1 p_1 = \text{constant}$, except in the case $q_1 p_1 = 0$, where $q_1 = 0$ or $p_1 = 0$. If $q_1 p_1 > 0$, the branches connect the bounding line segments $p_1 - q_1 = \pm c$ and if $q_1 p_1 < 0$, they have both end points on the same segment. A check of equation (2.4) shows that the orbits move as indicated by the arrows in Figure 2.1.

To interpret Figure 2.1 as a flow in \mathcal{R} , notice that each point in the (q_1, p_1) -plane projection corresponds to a 1-sphere, S^1 , or circle, in \mathcal{R} given by,

$$q_2^2 + p_2^2 = \frac{2}{\omega_p}(h - \lambda q_1 p_1).$$

Of course, for points on the bounding hyperbolic segments ($q_1 p_1 = h/\lambda$), the 1-sphere collapses to a point. Thus, the segments of the lines $p_1 - q_1 = \pm c$ in the projection correspond to the 2-spheres bounding \mathcal{R} . This is because each corresponds to a 1-sphere crossed with an interval where the two end 1-spheres are pinched to a point.

We distinguish nine classes of orbits grouped into the following four categories:

1. The point $q_1 = p_1 = 0$ corresponds to an invariant 1-sphere S_h^1 , an unstable **periodic orbit** in \mathcal{R} of energy $\mathcal{H}_2 = h$. This 1-sphere is given by,

$$q_2^2 + p_2^2 = \frac{2}{\omega_p} h, \quad q_1 = p_1 = 0. \quad (2.8)$$

It is an example of a normally hyperbolic invariant manifold (NHIM) (see [17]). Roughly, this means that the stretching and contraction rates under the linearized dynamics transverse to the 1-sphere dominate those tangent to the 1-sphere. This is clear for this example since the dynamics normal to the 1-sphere are described by the exponential contraction and expansion of the saddle point dynamics. Here the 1-sphere acts as a “big saddle point”. See the black dot at the center of the (q_1, p_1) -plane on the left side of Figure 2.1.

2. The four half open segments on the axes, $q_1 p_1 = 0$, correspond to four cylinder surfaces of orbits asymptotic to this invariant 1-sphere S_h^1 either as time increases ($q_1 = 0$) or as time decreases ($p_1 = 0$). These are called **asymptotic** orbits and they are the stable and the unstable manifolds of S_h^1 . The stable manifolds, $W_{\pm}^s(S_h^1)$, are given by,

$$q_2^2 + p_2^2 = \frac{2}{\omega_p} h, \quad q_1 = 0, \quad p_1 \text{ arbitrary.} \quad (2.9)$$

$W_+^s(S_h^1)$ (with $p_1 > 0$) is the branch entering from n_1 and $W_-^s(S_h^1)$ (with $p_1 < 0$) is the branch entering from n_2 . The unstable manifolds, $W_{\pm}^u(S_h^1)$, are given by,

$$q_2^2 + p_2^2 = \frac{2}{\omega_p} h, \quad p_1 = 0, \quad q_1 \text{ arbitrary} \quad (2.10)$$

$W_+^u(S_h^1)$ (with $q_1 > 0$) is the branch exiting from n_2 and $W_-^u(S_h^1)$ (with $q_1 < 0$) is the branch exiting from n_1 . See the four orbits labeled A of Figure 2.1.

3. The hyperbolic segments determined by $q_1 p_1 = \text{constant} > 0$ correspond to two solid cylinders of orbits which cross \mathcal{R} from one bounding 2-sphere to the other, meeting

both in the same hemisphere; the northern hemisphere if they go from $p_1 - q_1 = +c$ to $p_1 - q_1 = -c$, and the southern hemisphere in the other case. Since these orbits transit from one realm to another, we call them **transit** orbits. See the two orbits labeled T of Figure 2.1.

4. Finally the hyperbolic segments determined by $q_1 p_1 = \text{constant} < 0$ correspond to two cylinders of orbits in \mathcal{R} each of which runs from one hemisphere to the other hemisphere on the same bounding 2-sphere. Thus if $q_1 > 0$, the 2-sphere is n_2 ($p_1 - q_1 = -c$) and orbits run from the southern hemisphere ($q_1 + p_1 < 0$) to the northern hemisphere ($q_1 + p_1 > 0$) while the converse holds if $q_1 < 0$, where the 2-sphere is n_1 . Since these orbits return to the same realm, we call them **non-transit** orbits. See the two orbits labeled NT of Figure 2.1.

We define the transition region, \mathcal{T}_h , as the region of initial conditions of a given initial energy h which transit from one side of the neck region to the other. This is the set of all transit orbits, which has the geometry of a solid cylinder. The transition region, \mathcal{T}_h , is made up of one half which goes to the right (from n_1 to n_2), \mathcal{T}_{h+} , defined by $q_1 p_1 = \text{constant} > 0$ with both $q_1 > 0$ and $p_1 > 0$, and the other half which goes to the left (from n_2 to n_1), \mathcal{T}_{h-} , defined by $q_1 p_1 = \text{constant} > 0$ with both $q_1 < 0$ and $p_1 < 0$. The boundaries are $\partial\mathcal{T}_{h+}$ and $\partial\mathcal{T}_{h-}$, respectively. The closure of $\partial\mathcal{T}_h$, $\overline{\partial\mathcal{T}_h}$, is equal to the boundaries $\partial\mathcal{T}_{h+}$ and $\partial\mathcal{T}_{h-}$, along with the periodic orbit S_h^1 , i.e., $\partial\mathcal{T}_h \cup \overline{\partial\mathcal{T}_h} = \partial\mathcal{T}_{h+} \cup \partial\mathcal{T}_{h-} \cup S_h^1$.

In summary, for the conservative case, the boundary of the transition region, $\partial\mathcal{T}_h$, has the topology of a cylinder. The topology of $\partial\mathcal{T}_h$ will be different for the dissipative case, as will be shown in later sections. For convenience, we may refer to $\partial\mathcal{T}_h$ and $\overline{\partial\mathcal{T}_h}$ interchangeably.

2.2.2 McGehee representation of the equilibrium region

McGehee [18], building on the work of Conley [19], proposed a representation which makes it easier to visualize the region \mathcal{R} . Recall that \mathcal{R} is a 3-dimensional manifold that is homeomorphic to $S^2 \times I$. In [18], it is represented by a spherical annulus bounded by the two 2-spheres n_1, n_2 , as shown in Figure 2.2(c).

Figure 2.2(a) is a cross-section of \mathcal{R} . Notice that this cross-section is qualitatively the same as the saddle projection illustration in Figure 2.1. The full picture (Figure 2.2(c)) is obtained by rotating this cross section, Figure 2.2(b), about the indicated axis, where the azimuthal

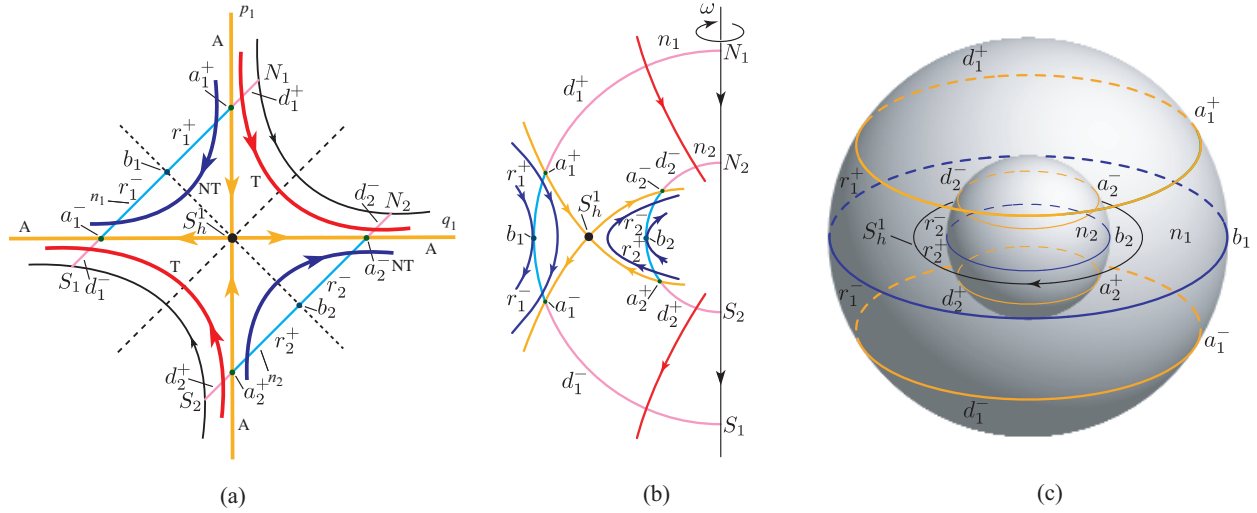


Figure 2.2: (a) The projection onto the (q_1, p_1) -plane, the saddle projection, with labels consistent with the text and (b) and (c). (b) The cross-section of the flow in the \mathcal{R} region of the energy surface. The north and south poles of bounding sphere n_i are labeled as N_i and S_i , respectively. (c) The McGehee representation of the flow on the boundaries of the \mathcal{R} region, highlighting the features on the bounding spheres n_1 and n_2 for $h > 0$.

angle ω roughly describes the angle in the center projection in Figure 2.1. The following classifications of orbits correspond to the previous four categories:

1. There is an invariant 1-sphere S_h^1 , a *periodic orbit* in the region \mathcal{R} corresponding to the black dot in the middle of Figure 2.2(a). Notice that this 1-sphere is the equator of the central 2-sphere given by $p_1 - q_1 = 0$.
2. Again let n_1, n_2 be the bounding 2-spheres of region \mathcal{R} , and let n denote either n_1 or n_2 . We can divide n into two hemispheres: n^+ , where the flow enters \mathcal{R} , and n^- , where the flow leaves \mathcal{R} . There are four cylinders of orbits asymptotic to the invariant 1-sphere S_h^1 . They form the stable and unstable manifolds which are *asymptotic* to the invariant 1-sphere S_h^1 . Topologically, both invariant manifolds look like 2-dimensional cylinders or “tubes” ($S^1 \times \mathbb{R}$) inside a 3-dimensional energy manifold. The interior of

the stable manifolds $W_{\pm}^s(S_h^1)$ and unstable manifolds $W_{\pm}^u(S_h^1)$ can be given as follows

$$\begin{aligned} \text{int}(W_+^s(S_h^1)) &= \{(q_1, p_1, q_2, p_2) \in \mathcal{R} \mid p_1 > q_1 > 0\}, \\ \text{int}(W_-^s(S_h^1)) &= \{(q_1, p_1, q_2, p_2) \in \mathcal{R} \mid p_1 < q_1 < 0\}, \\ \text{int}(W_+^u(S_h^1)) &= \{(q_1, p_1, q_2, p_2) \in \mathcal{R} \mid q_1 > p_1 > 0\}, \\ \text{int}(W_-^u(S_h^1)) &= \{(q_1, p_1, q_2, p_2) \in \mathcal{R} \mid q_1 < p_1 < 0\}. \end{aligned} \tag{2.11}$$

The exterior of these invariant manifolds can be given similarly from studying Figure 2.2(a) and (b).

- Let a^+ and a^- (where $q_1 = 0$ and $p_1 = 0$ respectively) be the intersections of the stable and unstable manifolds with the bounding sphere n . Then a^+ appears as a 1-sphere in n^+ , and a^- appears as a 1-sphere in n^- . Consider the two spherical caps on each bounding 2-sphere given by

$$\begin{aligned} d_1^+ &= \{(q_1, p_1, q_2, p_2) \in \mathcal{R} \mid p_1 - q_1 = +c, p_1 > q_1 > 0\}, \\ d_1^- &= \{(q_1, p_1, q_2, p_2) \in \mathcal{R} \mid p_1 - q_1 = +c, q_1 < p_1 < 0\}, \\ d_2^+ &= \{(q_1, p_1, q_2, p_2) \in \mathcal{R} \mid p_1 - q_1 = -c, p_1 < q_1 < 0\}, \\ d_2^- &= \{(q_1, p_1, q_2, p_2) \in \mathcal{R} \mid p_1 - q_1 = -c, q_1 > p_1 > 0\}. \end{aligned}$$

Since d_1^+ is the spherical cap in n_1^+ bounded by a_1^+ , then the *transit* orbits entering \mathcal{R} on d_1^+ exit on d_2^- of the other bounding sphere. Similarly, since d_1^- is the spherical cap in n_1^- bounded by a_1^- , the transit orbits leaving on d_1^- have come from d_2^+ on the other bounding sphere. Note that all spherical caps where the transit orbits pass through are in the interior of stable and unstable manifold tubes.

- Let b be the intersection of n^+ and n^- (where $q_1 + p_1 = 0$). Then, b is a 1-sphere of tangency points. Orbits tangent at this 1-sphere “bounce off,” i.e., do not enter \mathcal{R} locally. Moreover, if we let r^+ be a spherical zone which is bounded by a^+ and b , then *non-transit* orbits entering \mathcal{R} on r^+ exit on the same bounding 2-sphere through r^- which is bounded by a^- and b . It is easy to show that all the spherical zones where non-transit orbits bounce off are in the exterior of stable and unstable manifold tubes.

The McGehee representation provides an additional, perhaps clearer, visualization of the dynamics in the equilibrium region. In particular, the features on the two spheres, n_1 and

n_2 , which form $\partial\mathcal{R}$ for a constant $h > 0$, can be considered in the dissipative case as well, and compared with the situation in the conservative case, as shown for some examples below. The spheres n_1 and n_2 can be considered as spherical Poincaré sections parametrized by their distance from the saddle point, c , which reveal the topology of the transition region boundary, $\partial\mathcal{T}_h$, particularly through how the geometry of a_i^+ and a_i^- (for $i = 1, 2$) change as c changes.

2.3 Uncoupled system in the dissipative case: Ball rolling on a stationary surface

As pointed out in the introduction, when applying the symplectic change of variables consisting of the generalized eigenvectors of the conservative system to the dissipative system, the saddle projection and focus projection are coupled in some systems, while in others systems they are not. According to the coupling conditions, the systems are classified into two categories: uncoupled systems and coupled systems. In this section, we will discuss the uncoupled systems first.

Among the examples of escape from potential wells, a small ball or particle moving in an idealized fashion on a surface is an easy one from the perspective of both theory and experiment. The tracking of the moving object is easily executed by using a high-speed digital camera which is much easier than measurements of structural snap-through or ship motion, not to mention the motion of spacecraft in space. It can be either an inertial system or a gyroscopic system depending on whether the surface is stationary or rotating, due to a turntable, for instance [20]. The easy switch between non-gyroscopic system and gyroscopic system makes it easy to compare their similarities and differences in escape from potential wells. The mathematical model of a rolling ball on a stationary surface was established in [21]. Experiments [10, 22] regarding escape from the potential wells on similar surfaces were shown to validate the theory of the phase space conduits predicted by the mathematical model, which mediate the transitions between wells in the system. The dissipation of energy cannot be avoided in any physical experiment, but over small enough time-scales of interest, [10] justified that dissipation could be ignored. The good agreement between the theory and experiment to within 1% indicates the robustness of the transition tube in the conservative systems. However, it is still not clear how dissipation affects the transition of a rolling ball on

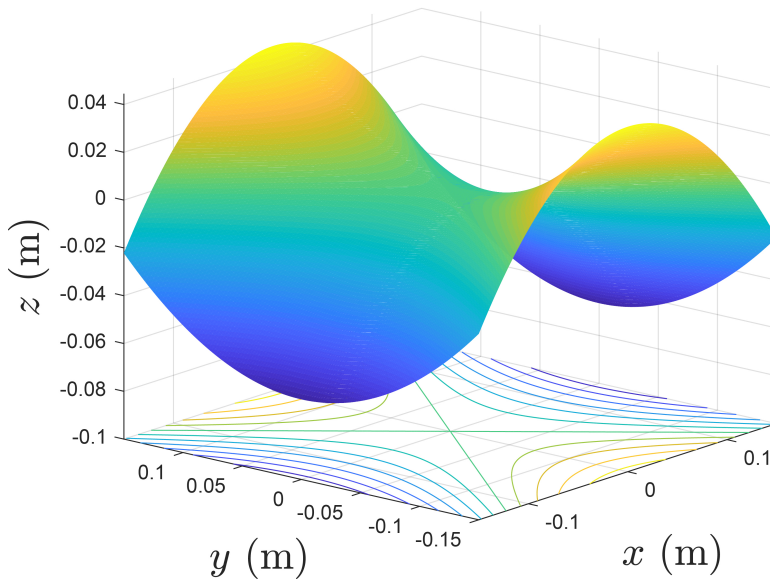


Figure 2.3: The graph of the example saddle surface considered, based on (2.12). The contours of the surface are projected on the bottom plane. The z direction is shown scaled by a factor of 2 compared to x and y in order to highlight the saddle nature of the surface.

a surface and what the phase space structure controlling the transition in the corresponding dissipative system is. In the current example, we will present the answers.

Here we consider a ball with unit mass rolling on a surface without slipping. Before analyzing the dynamical behavior of the rolling ball, a Cartesian coordinate system $o-xyz$ with z oriented upward is established. Thus, the equations of the surface can be determined by $z = H(x, y)$. In the current study, a saddle surface of the following form is selected,

$$H(x, y) = \frac{1}{2} (k_1 x^2 + k_2 y^2), \quad k_1 = -5.91 \text{ m}^{-1}, k_2 = 3.94 \text{ m}^{-1}, \quad (2.12)$$

which is shown in Figure 2.3.

Before analyzing the dynamical behavior of the system, one needs to obtain the equations of motion. To do so, one can use either the Lagrangian approach or Hamiltonian approach [1]. In the Lagrangian approach, the kinetic energy and potential energy are needed to get the Lagrangian function which will yield the Euler-Lagrangian equations. In the Hamiltonian approach, the generalized momenta should be defined by introducing a Legendre transformation from the Lagrangian and then the Hamiltonian function can be given which will generate the Hamilton's equations. In Section 2.4, we will consider a more complicated sys-

tem where the surface is not stationary, but it is rotating with a constant angular velocity ω where the gyroscopic force is included. Since the stationary surface is just a special case of the rotating surface where one takes angular velocity as zero, we do not separately derive the governing equations for the stationary surface and rotating surface. The derivation of the equations of motion will be briefly described for the current problem and readers can refer to Section 2.4 for more details.

From the analysis in Section 2.4, one can set the angular velocity of the rotating surface as zero to obtain the kinetic energy (the translational plus rotational without slipping), $\mathcal{K} = \frac{1}{2}I(\dot{x}^2 + \dot{y}^2 + \dot{z}^2)$, and potential energy, $\mathcal{U} = gz$, where $g = 9.81\text{m/s}^2$ is the gravitational acceleration and z and \dot{z} are written in terms of x , y , \dot{x} and \dot{y} via the relationship $z = H(x, y)$. The factor $I = 7/5$ is introduced by including rotational kinetic energy for a ball rolling without slipping. See details in the supplemental material in [10]. If we consider a particle sliding on the surface, we have $I = 1$. The kinetic energy \mathcal{K} and potential energy \mathcal{U} are,

$$\begin{aligned}\mathcal{K}(x, y) &= \frac{1}{2}I [\dot{x}^2 + \dot{y}^2 + (H_{,x}\dot{x} + H_{,y}\dot{y})^2], \\ \mathcal{U}(x, y) &= gH(x, y),\end{aligned}\tag{2.13}$$

where $H_{,x} = \partial H/\partial x$ and $H_{,y} = \partial H/\partial y$. Thus, one can define the Lagrangian function by,

$$\mathcal{L}(x, y) = \mathcal{K}(x, y, \dot{x}, \dot{y}) - \mathcal{U}(x, y),\tag{2.14}$$

which generates the Euler-Lagrange equations,

$$\frac{d}{dt} \left(\frac{\partial \mathcal{L}}{\partial \dot{q}_i} \right) - \frac{\partial \mathcal{L}}{\partial q_i} = Q_i,\tag{2.15}$$

where q_i are the generalized coordinates (x, y) and Q_i are the non-conservative forces. In the current problem, a small linear viscous damping, proportional to the magnitude of the inertial velocity, is considered, with the form given via a Rayleigh dissipation function as,

$$\begin{aligned}Q_x &= -c_d [(1 + H_{,x}^2) \dot{x} + H_{,x}H_{,y}\dot{y}], \\ Q_y &= -c_d [(1 + H_{,y}^2) \dot{y} + H_{,x}H_{,y}\dot{x}],\end{aligned}\tag{2.16}$$

where c_d is the coefficient of damping. The equations of motion for the current problem are,

$$\begin{aligned} I(1+k_1^2x^2)\ddot{x} + Ik_1k_2xy\ddot{y} + Ik_1^2x\dot{x}^2 + Ik_1k_2x\dot{y}^2 + gk_1x + c_d[(1+k_1^2x^2)\dot{x} + k_1k_2xy\dot{y}] &= 0, \\ Ik_1k_2xy\ddot{x} + I(1+k_2^2y^2)\ddot{y} + Ik_1k_2y\dot{x}^2 + Ik_2^2y\dot{y}^2 + gk_2y + c_d[(1+k_2^2y^2)\dot{y} + k_1k_2xy\dot{x}] &= 0. \end{aligned} \quad (2.17)$$

Once the Lagrangian system is established, one can transform it to a Hamiltonian system by use of the Legendre transformation,

$$p_i = \frac{\partial \mathcal{L}}{\partial \dot{q}_i}, \quad \mathcal{H}(q_i, p_i) = \sum_{i=1}^n p_i \dot{q}_i - \mathcal{L}(q_i, p_i), \quad (2.18)$$

where p_i are called the generalized momenta conjugate to the generalized coordinates q_i and \mathcal{H} the Hamiltonian function. In the current case, the Legendre transformation is given by,

$$\begin{aligned} p_x &= \frac{\partial \mathcal{L}}{\partial \dot{x}} = \dot{x} - y\omega + H_{,x}^2 \dot{x} + H_{,x} H_{,y} \dot{y}, \\ p_y &= \frac{\partial \mathcal{L}}{\partial \dot{y}} = \dot{y} + x\omega + H_{,x} H_{,y} \dot{x} + H_{,y}^2 \dot{y}. \end{aligned} \quad (2.19)$$

Therefore, one obtains the Hamiltonian function,

$$\mathcal{H} = \frac{[p_x^2(1+H_{,y}^2) - 2p_x p_y H_{,x} H_{,y} + p_y^2(1+H_{,x}^2)]}{2I(1+H_{,x}^2+H_{,y}^2)} + gH, \quad (2.20)$$

where p_x and p_y are the momenta conjugate to x and y , respectively. The comma in the subscript means the partial derivative with respect to the following coordinate. The general form of the Hamilton's equations with damping [1] are given by,

$$\dot{q}_i = \frac{\partial \mathcal{H}}{\partial p_i}, \quad \dot{p}_i = -\frac{\partial \mathcal{H}}{\partial q_i} + Q_i. \quad (2.21)$$

where Q_i is the same non-conservative generalized force written in terms of (q, p) variables. For simplicity, the specific form of Hamilton's equations for the current problem is not listed here.

For the surface adopted in (2.12), it has a saddle type equilibrium point at the origin $(0, 0)$. To study the transition from one side of the bottleneck to the other, the local dynamical behavior near the equilibrium point plays a critical role. Thus, we will obtain the linearized Hamiltonian equations around the equilibrium point to study the local properties. A short

computation for (2.21) gives the linearized equations of motion in Hamiltonian form as,

$$\begin{aligned}
 \dot{x} &= p_x/I, \\
 \dot{y} &= p_y/I, \\
 \dot{p}_x &= -gk_1x - c_d p_x/I, \\
 \dot{p}_y &= -gk_2y - c_d p_y/I.
 \end{aligned} \tag{2.22}$$

We introduce the following re-scaled parameters,

$$(\bar{q}_1, \bar{q}_2) = (x, y), (\bar{p}_1, \bar{p}_2) = (p_x, p_y)/I, (c_x, c_y) = -g(k_1, k_2)/I, c_h = c_d/I, \tag{2.23}$$

and the equations of motion can be rewritten in the simpler re-scaled form,

$$\begin{aligned}
 \dot{\bar{q}}_1 &= \bar{p}_1, \\
 \dot{\bar{q}}_2 &= \bar{p}_2, \\
 \dot{\bar{p}}_1 &= c_x \bar{q}_1 - c_h \bar{p}_1, \\
 \dot{\bar{p}}_2 &= c_y \bar{q}_2 - c_h \bar{p}_2.
 \end{aligned} \tag{2.24}$$

Written in matrix form, with column vector $\bar{z} = (\bar{q}_1, \bar{q}_2, \bar{p}_1, \bar{p}_2)^T$, we have $\dot{\bar{z}} = A\bar{z}$, where $A = M + D$, i.e.,

$$\dot{\bar{z}} = M\bar{z} + D\bar{z}, \tag{2.25}$$

where,

$$M = \begin{pmatrix} 0 & 0 & 1 & 0 \\ 0 & 0 & 0 & 1 \\ c_x & 0 & 0 & 0 \\ 0 & c_y & 0 & 0 \end{pmatrix}, \quad D = c_h \begin{pmatrix} 0 & 0 & 0 & 0 \\ 0 & 0 & 0 & 0 \\ 0 & 0 & -1 & 0 \\ 0 & 0 & 0 & -1 \end{pmatrix}. \tag{2.26}$$

The corresponding quadratic Hamiltonian for the linearized system is,

$$\mathcal{H}_2(\bar{q}_1, \bar{q}_2, \bar{p}_1, \bar{p}_2) = \frac{1}{2} (\bar{p}_1^2 + \bar{p}_2^2) - \frac{1}{2} (c_x \bar{q}_1^2 + c_y \bar{q}_2^2). \tag{2.27}$$

2.3.1 Analysis in the conservative system

First we analyze the behavior in the conservative system which can be obtained by taking zero damping, $c_h = 0$. It is straightforward to obtain the eigenvalues of the conservative system which are of the form $\pm\lambda$ and $\pm i\omega_p$ as expected, since the linearization matrix $A = M$ is an infinitesimal symplectic matrix (also known as a Hamiltonian matrix) [23, 24] where λ and ω_p are positive constants given by $\lambda = \sqrt{c_x}$ and $\omega_p = \sqrt{-c_y}$. The corresponding eigenvectors are defined as $u_{\pm\lambda}$ and $u_{\omega_p} \pm iv_{\omega_p}$, where $u_{\pm\lambda}$, u_{ω_p} , and v_{ω_p} are real vectors with the following form,

$$\begin{aligned} u_{+\lambda} &= (\lambda^2 - c_y, 0, \lambda^3 - \lambda c_y, 0), \\ u_{-\lambda} &= (-\lambda^2 + c_y, 0, \lambda^3 - \lambda c_y, 0), \\ u_{\omega_p} &= (0, \omega_p^2 + c_x, 0, 0), \\ v_{\omega_p} &= (0, 0, 0, \omega_p^3 + \omega_p c_x). \end{aligned} \tag{2.28}$$

Considering the change of variables defined by,

$$\bar{z} = Cz, \tag{2.29}$$

where $\bar{z} = (\bar{q}_1, \bar{q}_2, \bar{p}_1, \bar{p}_2)^T$ and $z = (q_1, q_2, p_1, p_2)^T$, with $C = (u_\lambda, u_{\omega_p}, u_{-\lambda}, v_{\omega_p})$ where u_λ , etc, are understood as column vectors, one can find,

$$C^T J C = \begin{pmatrix} 0 & \bar{D} \\ -\bar{D} & 0 \end{pmatrix}, \quad \bar{D} = \begin{pmatrix} d_\lambda & 0 \\ 0 & d_{\omega_p} \end{pmatrix},$$

where,

$$\begin{aligned} d_\lambda &= 2\lambda [(c_x - c_y)\lambda^2 - c_x c_y + c_y^2], \\ d_{\omega_p} &= \omega_p [(c_x - c_y)\omega_p^2 + c_x^2 - c_x c_y], \end{aligned}$$

and J is the 4×4 canonical symplectic matrix,

$$J = \begin{pmatrix} 0 & I_2 \\ -I_2 & 0 \end{pmatrix}, \tag{2.30}$$

where I_2 is the 2×2 identity matrix.

We can introduce two factors $s_1 = \sqrt{d_\lambda}$ and $s_2 = \sqrt{d_{\omega_p}}$ to the columns in C which makes it a symplectic matrix, i.e., satisfying $C^T J C = J$. The final form of the symplectic matrix is,

$$C = \begin{pmatrix} \frac{\lambda^2 - c_y}{s_1} & 0 & \frac{-\lambda^2 + c_y}{s_1} & 0 \\ 0 & \frac{\omega_p^2 + c_x}{s_2} & 0 & 0 \\ \frac{\lambda^3 - \lambda c_y}{s_1} & 0 & \frac{\lambda^3 - \lambda c_y}{s_1} & 0 \\ 0 & 0 & 0 & \frac{\omega_p^3 + \omega_p c_x}{s_2} \end{pmatrix}. \quad (2.31)$$

The equations of motion in the **symplectic eigenspace** (i.e., the z variables) can be obtained as,

$$\dot{z} = \Lambda z, \quad (2.32)$$

where $\Lambda = C^{-1} M C$ is the conservative part of the dynamics,

$$\Lambda = \begin{pmatrix} \lambda & 0 & 0 & 0 \\ 0 & 0 & 0 & \omega_p \\ 0 & 0 & -\lambda & 0 \\ 0 & -\omega_p & 0 & 0 \end{pmatrix}. \quad (2.33)$$

Thus, via the transformation (2.29), the equations of motion in the conservative system can be rewritten in a normal form given in (2.3) with Hamiltonian (2.1) whose solutions are given by (2.4).

Behavior in the position space Recalling the solutions in (2.4) and the symplectic matrix C in (2.31), we obtain the general (real) solutions of the conservative system in phase space in the form,

$$\begin{aligned} \bar{z}(t) &= (\bar{q}_1, \bar{q}_2, \bar{p}_1, \bar{p}_2)^T \\ &= q_1^0 e^{\lambda t} u_{+\lambda} + p_1^0 e^{-\lambda t} u_{-\lambda} + \text{Re} \left[\beta_0 e^{-i\omega_p t} (u_{\omega_p} - i v_{\omega_p}) \right], \end{aligned} \quad (2.34)$$

where $q_1^0, p_1^0, q_2^0, p_2^0$ are real and determined by initial conditions, where $\beta_0 = q_2^0 + i p_2^0$. In particular, we have,

$$\begin{aligned} \bar{q}_1(t) &= \frac{\lambda^2 - c_y}{s_1} q_1^0 e^{\lambda t} - \frac{\lambda^2 - c_y}{s_1} p_1^0 e^{-\lambda t}, \\ \bar{q}_2(t) &= \frac{\omega_p^2 + c_x}{s_2} (q_2^0 \cos \omega_p t + p_2^0 \sin \omega_p t). \end{aligned} \quad (2.35)$$

Notice that all trajectories in the configuration space in \mathcal{R} must evolve within the energy manifold which is bounded by the **zero velocity curve** (corresponding to $\bar{p}_1 = \bar{p}_2 = 0$) [8, 16, 25, 26] given by solving (2.27) as,

$$\bar{q}_2 = \pm \sqrt{\frac{-2h - c_x \bar{q}_1^2}{c_y}}. \quad (2.36)$$

By examining the general solution, we can see the solutions on the energy surface fall into different classes depending upon the limiting behavior of \bar{q}_1 as t goes to plus or minus infinity according to the fact that $\bar{q}_1(t)$ is dominated by the q_1^0 and p_1^0 terms when $t \rightarrow +\infty$ and $t \rightarrow -\infty$, respectively. Thus, the nine classes of orbits determined by varying the signs of q_1^0 and p_1^0 are classified into four categories.

1. If $q_1^0 = p_1^0 = 0$, we obtain a periodic solution with energy h . The periodic orbit, S_h^1 , projects onto the (\bar{q}_1, \bar{q}_2) plane as a segment with length $\sqrt{-2h/c_y}$.
2. Orbits with $q_1^0 p_1^0 = 0$ are asymptotic orbits. They are asymptotic to the periodic orbit, which is the origin, labeled S_h^1 in Figure 2.1. Asymptotic orbits with either $q_1^0 = 0$ or $p_1^0 = 0$ project into a strip S , as shown in Figure 2.4, bounded by lines,

$$\bar{q}_2 = \pm \frac{\omega_p^2 + c_x}{s_2} \sqrt{\frac{2h}{\omega_p}}. \quad (2.37)$$

3. Orbits with $q_1^0 p_1^0 > 0$ are transit orbits because they cross the equilibrium region \mathcal{R} from $-\infty$ (the left-hand side) to $+\infty$ (the right-hand side) or vice versa.
4. Orbits with $q_1^0 p_1^0 < 0$ are non-transit orbits.

Figure 2.4 gives the four categories of orbits mentioned above. In the figure, S is the strip confining the asymptotic orbits. Outside of the strip, the situation is simple and only non-transit orbits exist which means the signs of q_1^0 and p_1^0 are independent of the direction of the velocity and we always have $q_1^0 p_1^0 < 0$. The signs in each component of the equilibrium region \mathcal{R} complementary to the strip can be determined by limiting behavior of \bar{q}_1 for positive and negative infinite time. For example, in the left two components the non-transit orbits stay on the left side for $t \rightarrow \pm\infty$ which indicates $q_1^0 < 0$ and $p_1^0 > 0$. Similarly, in the right two components are $q_1^0 > 0$ and $p_1^0 < 0$. As one can determine from the discussions in the

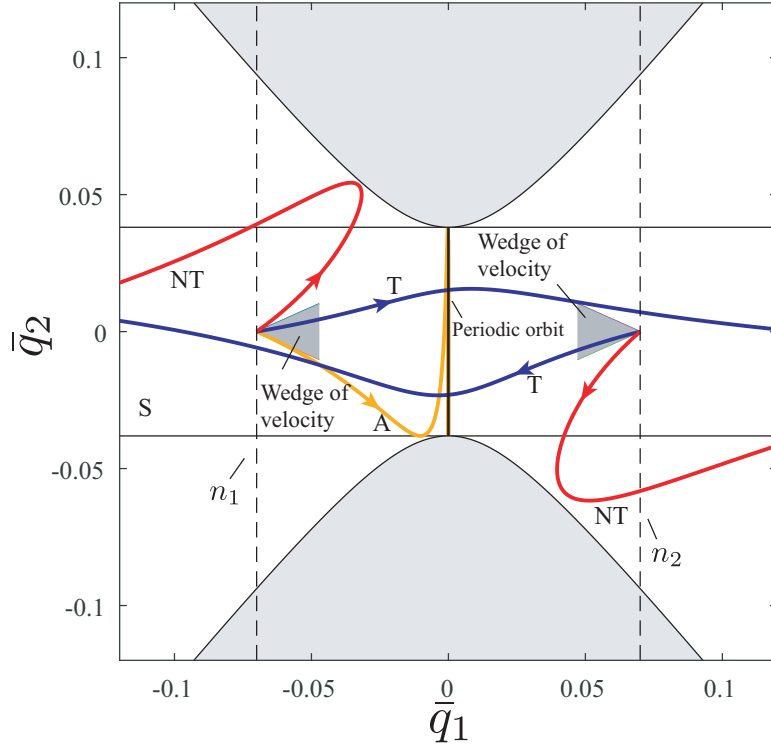


Figure 2.4: The flow in the equilibrium region \mathcal{R} projected onto position space (\bar{q}_1, \bar{q}_2) in the conservative system with fixed positive energy, $\mathcal{H}_2 = h > 0$, for a ball rolling on a stationary surface. Shown are the unstable periodic orbit (vertical segment in the center), a typical asymptotic orbit winding onto the periodic orbit; two transit orbits (blue); and two non-transit orbits (red). At each point on the bounding lines n_1 or n_2 (dashed) inside the strip S , there is a wedge of velocity dividing different types of orbits, inside of which are transit orbits, and outside of which are non-transit orbits; specifically, the trajectories with initial conditions on the boundary are the orbits asymptotic to the unstable periodic orbit. See the text for the explanation of the details.

phase space of the equilibrium region, the asymptotic orbits are the stable and unstable manifolds of a periodic orbit, which acts as a separatrix, the boundary of transition orbits and non-transit orbits. Denoting $(\bar{q}_{10}, \bar{q}_{20}, \bar{p}_{10}, \bar{p}_{20})$ as the initial conditions in phase space, the Hamiltonian function for asymptotic orbits in the phase space for the conservative system can be rewritten using the initial conditions as,

$$\frac{\bar{q}_{20}^2}{b_e^c} + \frac{\bar{p}_{20}^2}{c_e^2} = 0, \quad (2.38)$$

where b_e and c_e can be found in (2.49). The form of (2.38) is a cylinder or tube which will be discussed later.

Inside the strip, the situation is more complicated because the signs of $q_1^0 p_1^0$ are no longer independent of the direction of velocity. At each position inside the strip, there is a **wedge of velocity**, as proved in [7, 8, 16, 19, 27], separating the transit orbits and non-transit orbits whose two boundaries are given by the angles $\theta_{\pm} = \arctan(\bar{p}_{20\pm}/\bar{p}_{10})$ with respect to the \bar{q}_1 -axis, where,

$$\bar{p}_{10} = -\bar{q}_{10}\sqrt{c_x}, \quad \bar{p}_{20\pm} = \pm\sqrt{2h + c_y\bar{q}_{20}^2}, \quad (2.39)$$

See the shaded wedges in Figure 2.4. Here, the derivations are ignored for simplicity (they can be found in the analysis for the dissipative system in [8]). As a visualization and example, wedges on the two vertical bounding line segments are given. For example, consider the intersection of strip S with the left-most vertical line, n_1 . On this subsegment, there exists a non-empty wedge of velocity at each position. Orbits with their velocity inside the wedge are transit orbits ($q_1^0 p_1^0 > 0$), while orbits with velocity outside of the wedge are non-transit ($q_1^0 p_1^0 < 0$). Orbits with their velocity on the boundary of the wedge are asymptotic ($q_1^0 p_1^0 = 0$). The situation on the right-hand side subsegment is similar. Notice that the magnitude of the wedge depends on the initial positions ($\bar{q}_{10}, \bar{q}_{20}$). On the boundary of the strip, only one result of $\bar{p}_{20\pm}$ exists which indicates the wedge becomes a line along the boundary.

2.3.2 Analysis in the dissipative system

For the dissipative system, we still use the symplectic matrix C in (2.31) to perform a transformation, via (2.29), to the symplectic eigenspace, even though this is no longer the true eigenspace of the dissipative linearization matrix $A = M + D$. The equations of motion in the symplectic eigenspace are,

$$\dot{z} = \Lambda z + \Delta z, \quad (2.40)$$

where $\Lambda = C^{-1}MC$ is the conservative part of the dynamics, as before, and the transformed damping matrix is,

$$\Delta = C^{-1}DC = -c_h \begin{pmatrix} \frac{1}{2} & 0 & \frac{1}{2} & 0 \\ 0 & 0 & 0 & 0 \\ \frac{1}{2} & 0 & \frac{1}{2} & 0 \\ 0 & 0 & 0 & 1 \end{pmatrix}. \quad (2.41)$$

To analyze the behavior in the dissipative eigenspace (as opposed to the symplectic eigenspace),

the eigenvalues and eigenvectors, β_i and u_{β_i} , respectively, ($i = 1, \dots, 4$), are,

$$\begin{aligned} \beta_{1,2} &= -\delta \mp \frac{1}{2}\sqrt{c_h^2 + 4\lambda^2}, & u_{\beta_{1,2}} &= \left(\delta, 0, \lambda \pm \frac{1}{2}\sqrt{c_h^2 + 4\lambda^2}, 0 \right), \\ \beta_{3,4} &= -\delta \pm i\omega_d, & u_{\beta_{3,4}} &= (0, \omega_p, 0, -\delta \pm i\omega_d), \end{aligned} \quad (2.42)$$

where $\delta = \frac{1}{2}c_h$, $\omega_d = \omega_p\sqrt{1 - \xi_d^2}$ and $\xi_d = \delta/\omega_p$. Thus, the general (real) solutions are,

$$\begin{aligned} q_1(t) &= k_1 e^{\beta_{1t}} + k_2 e^{\beta_{2t}}, & p_1(t) &= k_3 e^{\beta_{1t}} + k_4 e^{\beta_{2t}}, \\ q_2(t) &= k_5 e^{-\delta t} \cos \omega_d t + k_6 e^{-\delta t} \sin \omega_d t, \\ p_2(t) &= \frac{k_5}{\omega_p} e^{-\delta t} (-\delta \cos \omega_d t - \omega_d \sin \omega_d t) + \frac{k_6}{\omega_p} e^{-\delta t} (\omega_d \cos \omega_d t - \delta \sin \omega_d t), \end{aligned} \quad (2.43)$$

where,

$$\begin{aligned} k_1 &= \frac{q_1^0 (2\lambda + \sqrt{c_1^2 + 4\lambda^2}) - c_1 p_1^0}{2\sqrt{c_1^2 + 4\lambda^2}}, & k_2 &= \frac{q_1^0 (-2\lambda + \sqrt{c_1^2 + 4\lambda^2}) + c_1 p_1^0}{2\sqrt{c_1^2 + 4\lambda^2}}, \\ k_3 &= \frac{p_1^0 (-2\lambda + \sqrt{c_1^2 + 4\lambda^2}) - c_1 q_1^0}{2\sqrt{c_1^2 + 4\lambda^2}}, & k_4 &= \frac{p_1^0 (2\lambda + \sqrt{c_1^2 + 4\lambda^2}) + c_1 q_1^0}{2\sqrt{c_1^2 + 4\lambda^2}}, \\ k_5 &= q_2^0, & k_6 &= \frac{p_2^0 \omega_p + q_2^0 \delta}{\omega_d}. \end{aligned}$$

Taking the total derivative of the Hamiltonian with respect to time along trajectories and using (2.40), we have,

$$\frac{d\mathcal{H}_2}{dt} = -\frac{1}{2}c_h \lambda (q_1 + p_1)^2 - c_h \omega_p p_2^2 \leq 0,$$

which means the Hamiltonian is generally decreasing (more precisely, non-increasing) due to damping.

The linear flow in \mathcal{R} . Similar to the discussions in the conservative system, we still choose the same equilibrium region \mathcal{R} to consider the projections on the (q_1, p_1) -plane and (q_2, p_2) -plane, respectively. Different from the saddle \times center projections in the conservative system, here we see saddle \times focus projections in the dissipative system. The stable focus is a damped oscillator with frequency of $\omega_d = \omega_p\sqrt{1 - \xi_d^2}$. Different classes of orbits can also be grouped into the following four categories:

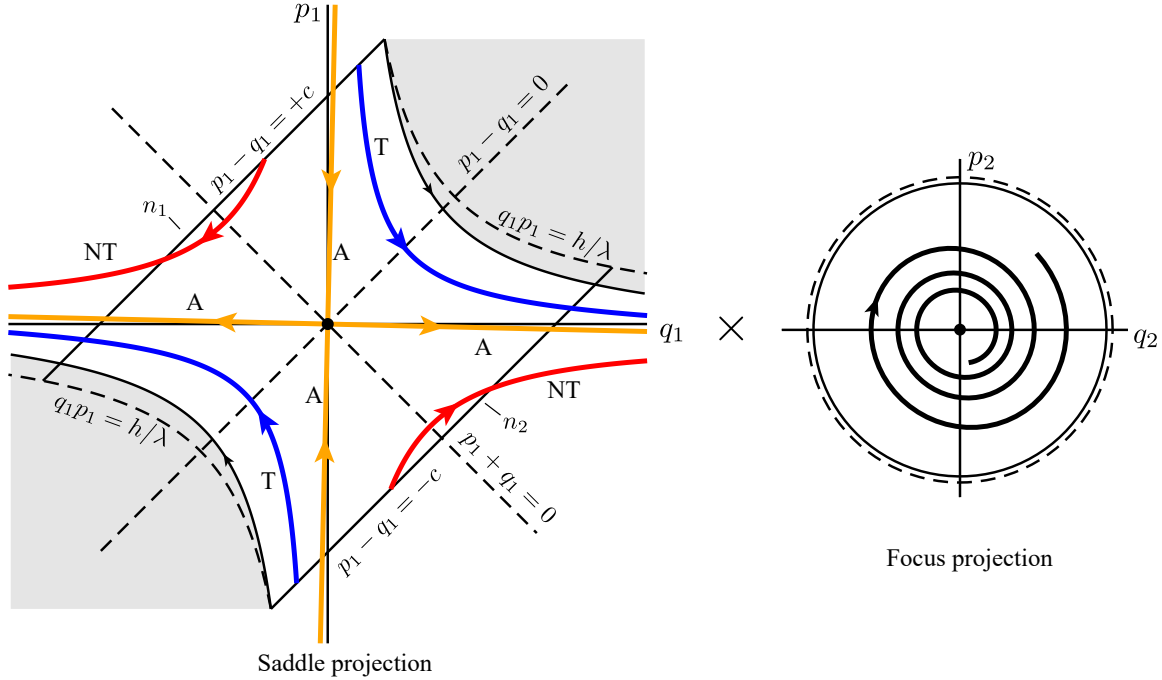


Figure 2.5: The flow in the equilibrium region for the dissipative system has the form saddle \times focus. On the left is shown the saddle projection onto the (q_1, p_1) -plane. The black dot at the origin represents focus-type asymptotic orbits with only a focus projection, thus oscillatory dynamics decaying towards the equilibrium point. The asymptotic orbits (labeled A) are the saddle-type asymptotic orbits which are tilted clockwise compared to the conservative system. They still form the separatrix between transit orbits (T) and non-transit orbits (NT). The hyperbolas, $q_1 p_1 = h/\lambda$, are no longer the boundary of trajectories with initial conditions on the bounding sphere (n_1 or n_2) due to the dissipation of the energy. The boundary of the shaded region are still the fastest trajectories with initial conditions on the bounding sphere, but are not strictly hyperbolas. Note that the saddle projection and focus projection are uncoupled in this dissipative system.

1. The point $q_1 = p_1 = 0$ corresponds to a **focus-type asymptotic** orbit with motion purely in the (q_2, p_2) -plane (see black dot at the origin of the (q_1, p_1) -plane in Figure 2.5). Such orbits are asymptotic to the equilibrium point itself, rather than a periodic orbit of energy h as in the conservative case. Due to the effect of damping, the periodic orbits on each energy manifold of energy h do not exist. The 1-sphere S_h^1 still exists, but is no longer invariant. Instead, it corresponds to all the initial conditions of initial energy h which are focus-type asymptotic orbits. The projection of S_h^1 to the configuration space in the dissipative system is the same as the projection of the periodic

orbit in the conservative system.

2. The four half open segments on the lines governed by $q_1 = c_h p_1 / (2\lambda \pm \sqrt{c_1^2 + 4\lambda^2})$ correspond to **saddle-type asymptotic** orbits. See the four orbits labeled A in Figure 2.5.
3. The segments which cross \mathcal{R} from one boundary to the other, i.e., from $p_1 - q_1 = +c$ to $p_1 - q_1 = -c$ in the northern hemisphere, and vice versa in the southern hemisphere, correspond to *transit* orbits. See the two orbits labeled T of Figure 2.5.
4. Finally the segments which run from one hemisphere to the other hemisphere on the same boundary, namely which start from $p_1 - q_1 = \pm c$ and return to the same boundary, correspond to *non-transit* orbits. See the two orbits labeled NT of Figure 2.5.

As done in Section 2.2.1, we define the transition region, \mathcal{T}_h , as the region of initial conditions of a given initial energy h which transit from one side of the neck region to the other. As before, the transition region, \mathcal{T}_h , is made up of one half which goes to the right, \mathcal{T}_{h+} , and the other half which goes to the left, \mathcal{T}_{h-} . The boundaries are $\partial\mathcal{T}_{h+}$ and $\partial\mathcal{T}_{h-}$, respectively. The closure of $\partial\mathcal{T}_h$, $\overline{\partial\mathcal{T}_h}$, is equal to the boundaries $\partial\mathcal{T}_{h+}$ and $\partial\mathcal{T}_{h-}$, along with the focus-type asymptotic initial conditions S_h^1 , i.e., as before, $\partial\mathcal{T}_{h-} \cup \partial\mathcal{T}_{h+} \cup S_h^1$.

As shown below, for the dissipative case, the closure of the boundary of the transition region, $\partial\mathcal{T}_h$, has the topology of an ellipsoid, rather than a cylinder as in the conservative case. As before, for convenience, we may refer to $\partial\mathcal{T}_h$ and $\overline{\partial\mathcal{T}_h}$ interchangeably.

McGehee representation. Similar to the McGehee representation for the conservative system given in Section 2.2.2 to visualize the region \mathcal{R} , here we utilize the McGehee representation again to illustrate the behavior in same region for the dissipative system. All labels are consistent throughout the study.

Note that since the McGehee representation uses spheres with the same energy to show the dynamical behavior in phase space, while the energy of any particular trajectory in the dissipative system decreases gradually during evolution, Figures 2.6(b) and 2.6(c) show only the initial conditions at a given initial energy. Therefore, in the present McGehee representation, only the initial conditions on the two bounding spheres are shown and discussed in the next part. In addition, the black dot near the orange dots a_i^\pm and b_i^\pm ($i = 1, 2$) in Figure 2.6(b)

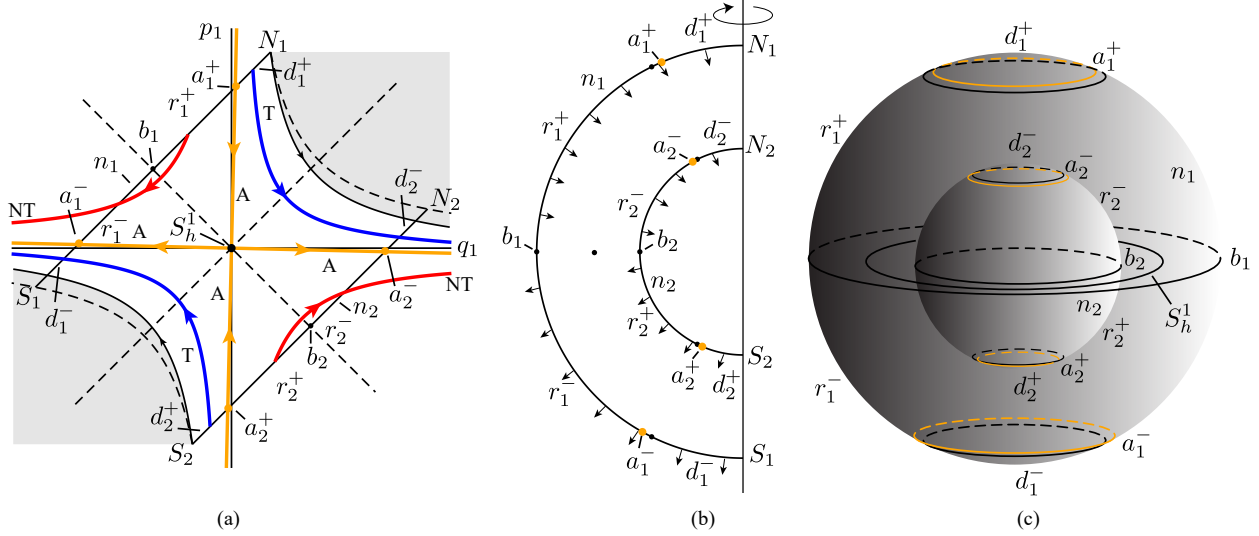


Figure 2.6: (a) The projection onto the (q_1, p_1) -plane, the saddle projection, with labels consistent with the text and (b) and (c). (b) The cross-section of the flow in the \mathcal{R} region of the energy surface. The north and south poles of bounding sphere n_i are labeled as N_i and S_i , respectively. (c) The McGehee representation of the flow in the region \mathcal{R} .

are the corresponding dots in the conservative system which are used to show how damping affects the transition.

The following classifications of orbits correspond to the previous four categories:

1. 1-sphere S_h^1 exists in the region \mathcal{R} corresponding to the black dot in the middle of Figure 2.6(b) and the equator of the central 2-sphere given by $p_1 - q_1 = 0$ in 2.6(c). The 1-sphere gives the initial conditions of the initial energy h for all focus-type asymptotic orbits. The same 1-sphere in the conservative system is invariant under the flow, that is, a periodic orbit of constant energy h . However, the corresponding S_h^1 is not invariant in the dissipative system, since the energy is decreasing during evolution due to the damping.
2. There are four 1-spheres in the region \mathcal{R} starting in the bounding 2-spheres n_1 and n_2 which give the initial conditions for orbits asymptotic to the equilibrium point. Two of them in n^+ , labeled by a^+ , are stable saddle-type asymptotic orbits and the other two in n^- , labeled by a^- , are unstable asymptotic orbits, where a^+ and a^- are given

by,

$$\begin{aligned}
 a_1^+ &= \{(q_1, p_1, q_2, p_2) \in \mathcal{R} \mid (q_1, p_1) = (k_p, 1)c/(1 - k_p)\}, \\
 a_1^- &= \{(q_1, p_1, q_2, p_2) \in \mathcal{R} \mid (q_1, p_1) = (-1, k_p)c/(1 + k_p)\}, \\
 a_2^+ &= \{(q_1, p_1, q_2, p_2) \in \mathcal{R} \mid (q_1, p_1) = (k_p, 1)c/(k_p - 1)\}, \\
 a_2^- &= \{(q_1, p_1, q_2, p_2) \in \mathcal{R} \mid (q_1, p_1) = (1, -k_p)c/(1 + k_p)\},
 \end{aligned} \tag{2.44}$$

where $k_p = c_h/(2\lambda + \sqrt{c_h^2 + 4\lambda^2})$. As shown in Figure 2.6(c), a^+ appears as an orange circle in n^+ , and a^- appears as an orange circle in n^- . The corresponding curves for the same energy in the conservative system are shown as black curves.

3. Consider the two spherical caps on each bounding 2-sphere, n_1 and n_2 , given by,

$$\begin{aligned}
 d_1^+ &= \{(q_1, p_1, q_2, p_2) \in \mathcal{R} \mid p_1 - q_1 = c, \quad q_1 > ck_p/(1 - k_p)\}, \\
 d_1^- &= \{(q_1, p_1, q_2, p_2) \in \mathcal{R} \mid p_1 - q_1 = c, \quad q_1 < -c/(1 + k_q)\}, \\
 d_2^+ &= \{(q_1, p_1, q_2, p_2) \in \mathcal{R} \mid p_1 - q_1 = -c, \quad q_1 < ck_p/(k_p - 1)\}, \\
 d_2^- &= \{(q_1, p_1, q_2, p_2) \in \mathcal{R} \mid p_1 - q_1 = -c, \quad q_1 > c/(1 + k_p)\}.
 \end{aligned} \tag{2.45}$$

The spherical cap d_1^+ , bounded by the a_1^+ on n_1^+ , gives all initial conditions of initial energy h for the transit orbits starting from the bounding sphere n_1^+ and entering \mathcal{R} . Similarly, the spherical cap b_1^- in n_1^- , bounded by a_1^- , determines all initial conditions of initial energy h for transit orbits starting on the bounding sphere n_1^- and leaving \mathcal{R} . The spherical caps d_2^+ and d_2^- on n_2 have similar dynamical behavior. Note that in the conservative system the transit orbits entering \mathcal{R} on d^+ will leave on d^- in the same 2-sphere. However, those transit orbits with the same initial conditions in the dissipative system will not leave on the corresponding 2-sphere, but leave on another sphere with lower energy. Moreover, the spherical caps d^+ shrink and d^- expand compared to that of the conservative system. Since the area of the caps d^+ and b^- determines the amount of transit orbits and non-transit orbits respectively, the shrinkage of the caps d^+ and expansion of the caps d^- means the damping reduces the probability of transition and increases the probability of non-transition, respectively.

4. Let b be the intersection of n^+ and n^- (where $q_1 + p_1 = 0$). Then, b is a 1-sphere of tangency points. Orbits tangent at this 1-sphere “bounce off”, i.e., do not enter \mathcal{R} locally. The spherical zones r_1 and r_2 , bounded by a_i^+ and a_i^- , give the initial conditions for non-transit orbits zone. r^+ , bounded by a_i^+ and b_i , are the initial conditions of initial

energy h for non-transit orbits entering \mathcal{R} and r_i^- are the initial conditions of initial energy h for non-transit orbits leaving \mathcal{R} . Note that unlike the shift of the spherical caps in the dissipative system compared to that of the conservative system, the tangent spheres b_1 and b_2 do not move when damping is taken into account. Moreover, in the conservative system, non-transit orbits enter \mathcal{R} on r^+ and then exit on the same energy bounding 2-sphere through r^- , but the non-transit orbits in the dissipative system exit on a different 2-sphere with different energy determined by the damping and the initial conditions.

Trajectories in the equilibrium region. From the analysis in the eigenspace, we obtain the general solution for the dissipative system in the original coordinates, that is,

$$\begin{aligned}\bar{q}_1(t) &= \frac{\lambda^2 - c_y}{s_1} (\bar{k}_1 e^{\beta_1 t} - \bar{k}_2 e^{\beta_2 t}), \\ \bar{q}_2(t) &= \frac{\omega_p^2 + c_x}{s_2} e^{-\delta t} (k_5 \cos \omega_d t + k_6 \sin \omega_d t),\end{aligned}\tag{2.46}$$

where $\bar{k}_1 = k_1 - k_3$ and $\bar{k}_2 = k_4 - k_2$.

Analogous to the situation in the conservative system, we can still classify the orbits into different classes depending on the limiting behavior of \bar{q}_1 as t tends to plus or minus infinity. Four different categories of orbits can be obtained:

1. Orbits with $\bar{k}_1 = \bar{k}_2 = 0$ are *focus-type asymptotic* orbits.
2. Orbits with $\bar{k}_1 \bar{k}_2 = 0$ are *saddle-type asymptotic* orbits.
3. Orbits with $\bar{k}_1 \bar{k}_2 > 0$ are *transit* orbits.
4. Orbits with $\bar{k}_1 \bar{k}_2 < 0$ are *non-transit* orbits.

Wedge of velocity and ellipse of transition. As discussed in Section 2.3.2, the initial conditions of stable asymptotic orbits in the saddle projection of the phase space should be governed by,

$$q_1 = k_p p_1,\tag{2.47}$$

which governs the stable asymptotic orbits which is the boundary of the transit orbits. For the initial conditions in the position space and symplectic eigenspace, denoted by

$(\bar{q}_{10}, \bar{q}_{20}, \bar{p}_{10}, \bar{p}_{20})$ and $(q_{10}, q_{20}, p_{10}, p_{20})$, respectively, they can be connected by the symplectic matrix (2.31). By using (2.47) and the change of variables (2.29), the Hamiltonian function for asymptotic orbits in the symplectic eigenspace can be rewritten by eliminating $q_{10}, q_{20}, p_{10}, p_{20}$ and \bar{p}_{10} , as,

$$\frac{\bar{q}_{10}^2}{a_e^2} + \frac{\bar{q}_{20}^2}{b_e^2} + \frac{\bar{p}_{20}^2}{c_e^2} = 1, \quad (2.48)$$

where,

$$a_e = \sqrt{\frac{h(k_p - 1)^2(\lambda^2 - c_y)^2}{k_p s_1^2 \lambda}}, \quad b_e = \sqrt{\frac{2h(\omega_p^2 + c_x)^2}{s_2^2 \omega_p}}, \quad c_e = \sqrt{\frac{2h\omega_p(\omega_p^2 + c_x)^2}{s_2^2}}, \quad (2.49)$$

which is geometrically an ellipsoid (topologically a 2-sphere). As (2.48) is the boundary between transit and non-transit orbits starting at an initial energy h , we therefore refer to the object described by (2.48) as the **transition ellipsoid** of energy h . The critical condition for the existence of real solutions for \bar{p}_{20} requires zero discriminant for (2.48), that is,

$$\frac{\bar{q}_{10}^2}{a_e^2} + \frac{\bar{q}_{20}^2}{b_e^2} = 1, \quad \bar{p}_{20} = 0, \quad (2.50)$$

which is an ellipse in the configuration space called the **ellipse of transition**, and is merely the configuration space projection of the transition ellipsoid (2.48), first found in [8]. The ellipse of the transition confines the existence of transit orbits of a given initial energy which means the transit orbits can just exist inside the ellipse. For a specific position $(\bar{q}_{10}, \bar{q}_{20})$ inside the ellipse, $(\bar{q}_{10}/a_e)^2 + (\bar{q}_{20}/b_e)^2 < 1$, the solutions of $(\bar{p}_{10}, \bar{p}_{20})$ are written as,

$$\bar{p}_{20} = \pm c_e \sqrt{1 - \frac{\bar{q}_{10}^2}{a_e^2} - \frac{\bar{q}_{20}^2}{b_e^2}}, \quad \bar{p}_{10} = \frac{k_p + 1}{k_p - 1} \lambda \bar{q}_{10}. \quad (2.51)$$

Each pair of $(\bar{p}_{10}, \bar{p}_{20})$ determines an angle: $\theta = \arctan(\bar{p}_{20}/\bar{p}_{10})$, which together defines the wedge of velocity. The boundary of the wedge gives the two asymptotic orbits at that position.

Figure 2.7 gives the projection on the position space in the equilibrium region. The strip projected onto configuration space in the conservative system which is the boundary of the asymptotic orbits is replaced by the ellipse of transition, which restricts the existence of transition for initial conditions of initial energy h to a locally bounded region. Outside the ellipse, the situation is simple: only non-transit orbits exist. Inside the ellipse, the situation is

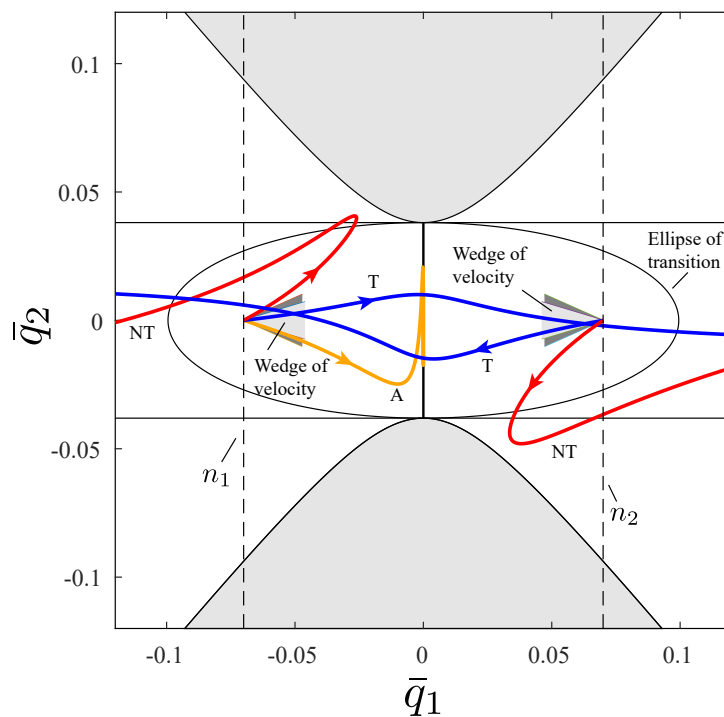


Figure 2.7: The flow in the equilibrium region \mathcal{R} projected onto position space (\bar{q}_1, \bar{q}_2) in the dissipative system with fixed positive energy, $\mathcal{H}_2 = h > 0$, for a ball rolling on a stationary surface. Shown are different types of orbits as discussed in the text. Notice that due to the dissipation of energy, the periodic orbit in the conservative system does not exist, but is replaced by the initial conditions of initial energy h of the focus-type asymptotic orbits. Moreover, the strip for the conservative system—which is the position space projection of the tubes of transition at initial energy h —is replaced by the ellipse of transition. It means that the existence of transit orbits are constrained by the ellipse so that the wedge of velocity, determining the permissible direction of the transit orbits, only exists inside the ellipse. For a given fixed energy h , the wedge of velocity for the dissipative system is a subset of the wedge for the conservative system which is shown as a darker wedge.

more complicated since there is a wedge of velocity restricting the direction of transit orbits. The orbits with velocity interior to the wedge are transit orbits, while orbits with velocity outside the wedge are non-transit orbits. The boundary of the wedge gives the velocity for the asymptotic orbits. Note that for different points in the position space, the size of the wedge of velocity varies. The closer the wedge is to the boundary of the ellipse of transition, the smaller it is. Clearly, on the ellipse the wedge becomes a line which means only one asymptotic orbit exists there. Note that in the figure, the light grey shaded wedges are the wedges for the dissipative system, while the dark grey shaded wedges partially covered by the

light grey ones are for the conservative system of the same initial energy h . The significant shrinking of the wedges from the conservative system to the dissipative system is caused by damping. It means an increase in damping decreases the size of the ellipse of transition and wedges on a specific point, which confirms our expectation.

2.3.3 Transition tube and transition ellipsoid

In the position space, we discussed how damping affects the transition. In fact, the strip in the conservative system and ellipse in the dissipative system associated with respective wedges of velocity can predict the transition and non-transition in the corresponding system for a given energy in the position space.

To obtain the initial conditions for asymptotic orbits, the Hamiltonian function for asymptotic orbits has been rewritten in the form of a tube in (2.38) for the conservative system and the form of an ellipsoid in (2.48) for the dissipative system, respectively. Here we refer to them as the *transition tube* and *transition ellipsoid*, respectively. Compactly, both are $\partial\mathcal{T}_h$. See the tube and ellipsoid in Figure 2.8 and Figure 2.9, respectively. In the figures, the tube and the ellipsoid give the boundaries of the initial conditions for transit orbits starting with a given initial energy h in the conservative and the dissipative systems, respectively; all transit orbits must have initial conditions inside the transition tube or transition ellipsoid, respectively; non-transit orbits have initial conditions outside the boundary and asymptotic orbits have initial conditions on the boundary; of course, the periodic orbit not only has initial conditions on the boundary of the transition tube, but also evolves on the boundary. Note that there is a **critical surface boundary**, given by S_h^1 , dividing the tube and ellipsoid into two parts. The left side part is composed of transit orbits *going to the right* and the right part for transit orbits *going to the left*.

The orbits with initial conditions on the critical surface S_h^1 are periodic orbits if in the conservative system or focus-type asymptotic orbits if in the dissipative system. The periodic orbit keeps evolving on the critical surface, while the focus-type asymptotic orbit gradually approaches the equilibrium point and finally stops there. The critical surface also plays another important role separating the motion of transit orbits and non-transit orbits. Transit orbits can cross the surface, while non-transit orbits will bounce back before reaching it. Of course, the asymptotic orbits move asymptotically towards the surface.

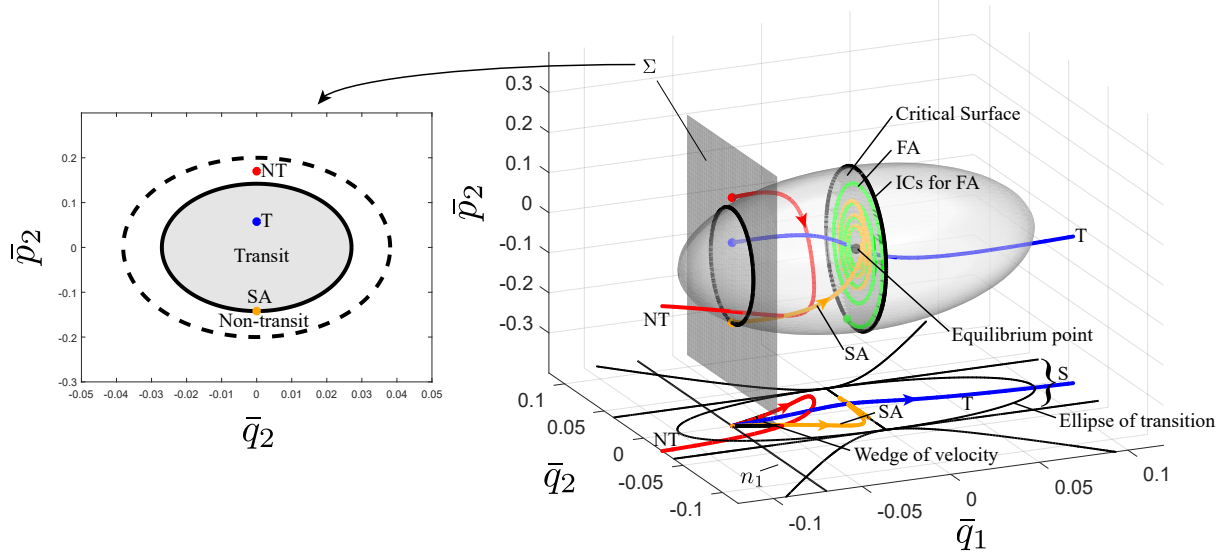


Figure 2.9: Transition ellipsoid for the dissipative system of a rolling ball on a stationary surface. The left figure shows the Poincaré section Σ , where the dots are the initial conditions for the corresponding trajectories with the same color in the right figure and the solid ellipse is the set of initial conditions for saddle-type asymptotic orbits. For comparison, the dashed ellipse of the tube boundary for the conservative system with the same energy h is also given. On the right is the ellipsoid giving the initial conditions for all transit orbits. The critical surface divides the ellipsoid into two parts. Each side of the ellipsoid gives the initial conditions of transit orbits passing through the critical surface to the other side. In this figure, SA and FA denote the saddle-type and focus-type asymptotic orbits, respectively.

for the dissipative system (see the area encompassed by the solid closed curve) is smaller than the transit region for the conservative system (see the area encompassed by the dashed closed curve) for the same initial energy h . The decrease in the area for the transition is caused by the dissipation of the energy. In fact the transit orbit in the conservative system and the non-transit orbit in the dissipative system plotted in the figure have the same initial conditions which means the dissipation of energy can make a transit orbit in the conservative system become a non-transit orbit if dissipation is added.

Up to now, we give the geometry governing the transition in both the position space and phase space. In the position space the strip in the conservative system and the ellipse in the dissipative system are the projections of the outline of the transition tube and transition ellipsoid, respectively. The wedge of velocity on a specific position (\bar{q}_1, \bar{q}_2) has two boundaries. The boundaries are the projections of the upper and lower bounds on the corresponding

Poincaré section at \bar{q}_2 .

2.4 Coupled system in the dissipative case: Ball rolling on a rotating surface

In Section 2.3, we investigated the geometry of escape/transition in uncoupled systems (in the symplectic eigenspace) which are generally inertial systems with equal damping in each degree of freedom. Due to the uncoupled property, it is easy to obtain the analytical solutions and the dynamical behavior. We have found the transition tube and transition ellipsoid governing the escape in the conservative and dissipative systems, respectively. Another category of system is one in which the saddle and focus are coupled with each other when the system is transformed to the corresponding eigenspace. The situation is more complicated but important and interesting. The first kind is an inertial system with unequal damping, like the ship motion discussed in [13]. Another one is a system with both gyroscopic and dissipative forces present. Such systems can display non-intuitive phenomena, like dissipation-induced instabilities [3] as discussed in the introduction. In this section, we establish the mathematical models for some physical problems and reveal the geometry of escape/transition in such systems.

In Section 2.3, the rolling ball on a stationary surface was studied and the effect of dissipative forces was considered. We established it as a standard example to investigate the escape from a potential well in inertial systems with equal damping and revealing the escape mechanism in such systems. Here we further expand the framework regarding escape to a more complicated situation where the surface is rotating such that gyroscopic forces exist. Several researchers have investigated a ball or particle moving on a rotating surface [3, 4, 5, 28, 29], mainly due to the unexpected dissipation-induced instabilities. The combination of the dissipative and gyroscopic forces enriches the behavior in escape dynamics.

2.4.1 Governing equations

Consider a rotating surface with counterclockwise angular velocity ω as shown in Figure 2.10. Let X - Y - Z be an inertial frame, denoted as the N frame, with origin O , where X - Y plane is horizontal and Z is vertical to the plane. Establish another rotating frame x - y - z ,

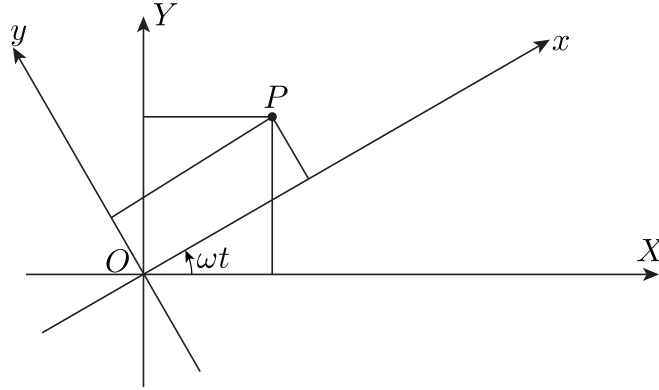


Figure 2.10: Inertial and rotating frames. The rotating coordinate system of x and y axes moves counterclockwise with constant angular velocity ω relative to the inertial frame with X and Y axes. The z axis coincides with the Z axis which is pointing out of the plane and is not shown here. We denote the unit vectors along x , y , z by \mathbf{e}_1 , \mathbf{e}_2 and \mathbf{e}_3 , respectively.

denoted as the R frame, with the same origin O fixed on the rotating surface, where Oz coincides with OZ . In this study, the geometrical parameters of the rotating surface are the same as before given in (2.12).

The angular velocity vector of the R frame relative to the N frame is,

$$\boldsymbol{\omega}^{R/N} = \omega \mathbf{e}_3. \quad (2.52)$$

A particle (or ball), denoted by P , with unit mass, moves on the rotating surface, with a position vector described in the R frame as,

$$\mathbf{P}(x, y, z, t) = x(t)\mathbf{e}_1 + y(t)\mathbf{e}_2 + z(t)\mathbf{e}_3, \quad (2.53)$$

where (x, y, z) is the position of the mass in the R frame. The inertial velocity of the mass can be written in the R frame as,

$$\begin{aligned} {}^N \mathbf{v}^P &= \dot{x}\mathbf{e}_1 + \dot{y}\mathbf{e}_2 + \dot{z}\mathbf{e}_3 + \boldsymbol{\omega}^{R/N} \times \mathbf{P} \\ &= (\dot{x} - y\omega)\mathbf{e}_1 + (\dot{y} + x\omega)\mathbf{e}_2 + \dot{z}\mathbf{e}_3. \end{aligned} \quad (2.54)$$

Considering the motion is constrained on the rotating surface, here z is not an independent variable, but depends on x and y via $z = H(x, y)$. Thus, the kinetic energy \mathcal{K} and potential energy \mathcal{U} are,

$$\begin{aligned}\mathcal{K}(x, y) &= \frac{1}{2}I|{}^N\mathbf{v}^P|^2 = \frac{1}{2}I [(\dot{x} - y\omega)^2 + (\dot{y} + x\omega)^2 + (H_{,x}\dot{x} + H_{,y}\dot{y})^2], \\ \mathcal{U}(x, y) &= gH(x, y).\end{aligned}\tag{2.55}$$

After obtaining the Lagrangian function, $\mathcal{L} = \mathcal{K} - \mathcal{U}$, we can derive the Euler-Lagrange equations given in (2.15). As discussed in [4], two types of damping can be considered in the rotating surface system, i.e., **internal damping** and **external damping**. Internal damping is proportional to the relative velocity measured in the rotating frame, while external damping is proportional to the inertial velocity. Thus, the mathematical form of two types of the generalized damping forces are,

$$\begin{aligned}Q_x^{\text{int}} &= -c_d [(1 + H_{,x}^2) \dot{x} + H_{,x}H_{,y}\dot{y}], \\ Q_y^{\text{int}} &= -c_d [(1 + H_{,y}^2) \dot{y} + H_{,x}H_{,y}\dot{x}],\end{aligned}\quad \text{for internal damping}\tag{2.56}$$

and,

$$\begin{aligned}Q_x^{\text{ext}} &= -c_d [(1 + H_{,x}^2) \dot{x} + H_{,x}H_{,y}\dot{y} - \omega y], \\ Q_y^{\text{ext}} &= -c_d [(1 + H_{,y}^2) \dot{y} + H_{,x}H_{,y}\dot{x} + \omega x],\end{aligned}\quad \text{for external damping}\tag{2.57}$$

where c_d is the coefficient of damping. In the current problem, we only consider internal damping, $(Q_x, Q_y) = (Q_x^{\text{int}}, Q_y^{\text{int}})$, due to the friction between the mass and the moving surface, as the most physically relevant.

The equations of motion can be written in non-dimensional Hamiltonian form, using a Hamiltonian function \mathcal{H} as given in Appendix A. Following the same procedure as for the ball rolling on a stationary surface, we linearize the equations of motion around the saddle point at the origin which gives the linearized non-dimensional Hamilton's equation in matrix form,

$$\dot{\bar{z}} = M\bar{z} + D\bar{z},\tag{2.58}$$

where $\bar{z} = (\bar{q}_1, \bar{q}_2, \bar{p}_1, \bar{p}_2)^T$ is the displacement from the saddle point, and where,

$$M = \begin{pmatrix} 0 & \omega & 1 & 0 \\ -\omega & 0 & 0 & 1 \\ c_x & 0 & 0 & \omega \\ 0 & c_y & -\omega & 0 \end{pmatrix}, \quad D = c_h \begin{pmatrix} 0 & 0 & 0 & 0 \\ 0 & 0 & 0 & 0 \\ 0 & -\omega & -1 & 0 \\ \omega & 0 & 0 & -1 \end{pmatrix}. \quad (2.59)$$

The quadratic Hamiltonian function corresponding to matrix M is,

$$\mathcal{H}_2(\bar{q}_1, \bar{q}_2, \bar{p}_1, \bar{p}_2) = \frac{1}{2} (\bar{p}_1^2 + \bar{p}_2^2) + \omega \bar{p}_1 \bar{q}_2 - \omega \bar{p}_2 \bar{q}_1 - \frac{1}{2} (c_x \bar{q}_1^2 + c_y \bar{q}_2^2). \quad (2.60)$$

2.4.2 Analysis in the conservative system

In this section, the dynamic behavior in the conservative system will be analyzed. Here the damping c_h is set to zero which gives,

$$\dot{\bar{z}} = M\bar{z}. \quad (2.61)$$

Curiously, we are able to use the eigenvectors of M in (2.59) and use them to construct a symplectic linear change of variables which changes (2.61) into the simple normal form (2.3), with the simple Hamiltonian function (2.1) and with solutions as given in (2.4). The details are in Appendix A.

Trajectories in the equilibrium region. The flow in the equilibrium region \mathcal{R} in the symplectic eigenspace was performed for the normal form in Section 2.2 and will not be repeated here. However, it is instructive to study the appearance of the orbits in the position space for this particular problem, i.e., the (\bar{q}_1, \bar{q}_2) plane. Note that the evolution of all trajectories must be restricted by the given energy h which forms the zero velocity curves [7] (corresponding to $\dot{v}_x = \dot{v}_y = 0$) which bound the motion in the position space projection and are determined by the following function,

$$\bar{q}_2(\bar{q}_1) = \pm \sqrt{\frac{-2h - (c_x + \omega^2) \bar{q}_1^2}{c_y + \omega^2}}, \quad (2.62)$$

which is obtained from (2.60).

From the solutions in the symplectic eigenspace (2.4), we can obtain the general (real) solutions in the position space by using the transformation matrix C in (A.16) which yields the general (real) solutions with the form (2.34). Thus, we can obtain the solutions for \bar{q}_1 and \bar{q}_2 , given the initial conditions in the eigenspace, $(q_1^0, q_2^0, p_1^0, p_2^0)$,

$$\begin{aligned}\bar{q}_1(t) &= \frac{\lambda^2 - c_y - \omega^2}{s_1} q_1^0 e^{\lambda t} - \frac{\lambda^2 - c_y - \omega^2}{s_1} p_1^0 e^{-\lambda t} - \frac{2\omega\omega_p}{s_2} (p_2^0 \cos \omega_p t - q_2^0 \sin \omega_p t), \\ \bar{q}_2(t) &= -\frac{2\lambda\omega}{s_1} q_1^0 e^{\lambda t} - \frac{2\lambda\omega}{s_1} p_1^0 e^{-\lambda t} - \frac{\omega_p^2 + c_x + \omega^2}{s_2} (q_2^0 \cos \omega_p t + p_2^0 \sin \omega_p t).\end{aligned}\quad (2.63)$$

Upon inspecting the general solution, we see that the solutions on the energy surface fall into different classes depending upon the limiting behavior of $\bar{q}_1(t)$ as t tends to plus or minus infinity. As the $\bar{q}_1(t)$ expression is dominated by the q_1^0 term as $t \rightarrow +\infty$, \bar{q}_1 tends to minus infinity (staying on the left-hand side), is bounded (staying around the equilibrium point), or tends to plus infinity (staying on the right-hand side) for $q_1^0 > 0$, $q_1^0 = 0$ and $q_1^0 < 0$, respectively. The statement holds if $t \rightarrow -\infty$ and $-p_1^0$ replaces q_1^0 . Varying the signs of q_1^0 and p_1^0 , and following the procedures described in [8, 19], one can also obtain the same nine classes of orbits grouped into the same four categories as in Section 2.3.

1. If $q_1^0 = p_1^0 = 0$, we obtain a periodic solution with the following projection onto the position space,

$$\frac{\bar{q}_1^2}{\left(\frac{2\omega\omega_p}{s_2} \sqrt{\frac{2h}{\omega_p}}\right)^2} + \frac{\bar{q}_2^2}{\left(\frac{\omega_p^2 + c_x + \omega^2}{s_2} \sqrt{\frac{2h}{\omega_p}}\right)^2} = 1. \quad (2.64)$$

Here, the initial energy is $h = \frac{1}{2}\omega_p [(q_2^0)^2 + (p_2^0)^2]$. Identical to what has been proved by Conley [19] for the restricted three-body problem, this periodic orbit, shown in Figure 2.11, projects onto the (\bar{q}_1, \bar{q}_2) plane as an ellipse. Note that the size of the ellipse goes to zero with h . It is different from the non-gyroscopic system where the periodic orbit projects to a straight segment in the position space.

2. Orbits with $q_1^0 p_1^0 = 0$ are asymptotic orbits. They are asymptotic to the periodic orbits of category 1. The asymptotic orbit with $q_1^0 = 0$ projects into the strip S_1 in the (\bar{q}_1, \bar{q}_2) plane bounded by the lines,

$$\bar{q}_2 = \frac{2\lambda\omega}{\lambda^2 - c_y - \omega^2} \bar{q}_1 \pm \sqrt{\left(\frac{4\lambda\omega_p\omega^2}{s_2(\lambda^2 - c_y - \omega^2)}\right)^2 + \left(\frac{\omega_p^2 + c_x + \omega^2}{s_2}\right)^2} \sqrt{\frac{2h}{\omega_p}}, \quad (2.65)$$

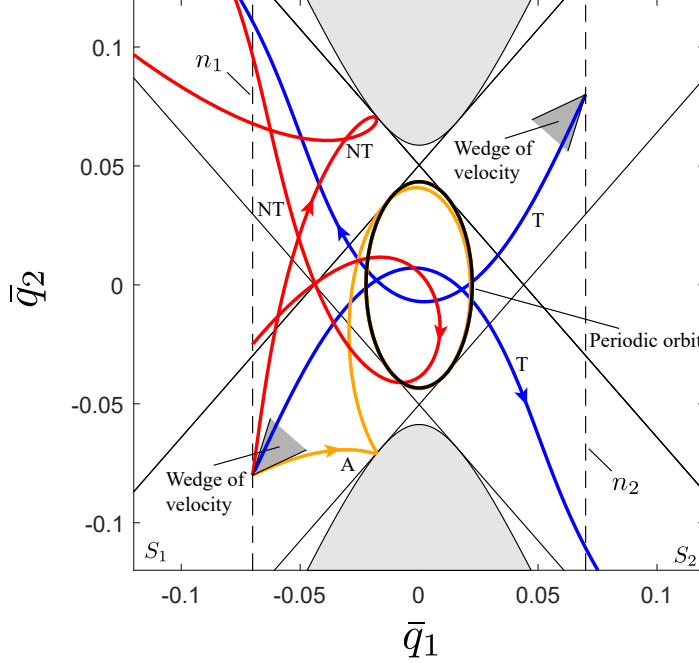


Figure 2.11: The flow in the equilibrium region \mathcal{R} projected onto position space (\bar{q}_1, \bar{q}_2) in the conservative system with fixed positive energy, $\mathcal{H}_2 = h > 0$, for a ball rolling on a rotating surface. Shown are the periodic orbit acting as an ellipse; one asymptotic orbit gradually approaching the periodic orbit; two transit orbits; and two non-transit orbits, one starting inside the strips and the other outside the strips. Note that the dynamic behavior in the position space is identical to those in the circular restricted three-body problem [15, 16].

while orbits with $p_1^0 = 0$ project into the strip S_2 bounded by the lines,

$$\bar{q}_2 = -\frac{2\lambda\omega}{\lambda^2 - c_y - \omega^2}\bar{q}_1 \pm \sqrt{\left(\frac{4\lambda\omega_p\omega^2}{s_2(\lambda^2 - c_y - \omega^2)}\right)^2 + \left(\frac{\omega_p^2 + c_x + \omega^2}{s_2}\right)^2} \sqrt{\frac{2h}{\omega_p}}. \quad (2.66)$$

In fact, S_1 is for stable asymptotic orbits, while S_2 is for unstable asymptotic orbits. Notice the width of the strips depends on h and goes to zero as $h \rightarrow 0$.

3. Orbits with $q_1^0 p_1^0 > 0$ are transit orbits because they cross the equilibrium region \mathcal{R} from $-\infty$ (the left-hand side) to $+\infty$ (the right-hand side) or vice versa.
4. Orbits with $q_1^0 p_1^0 < 0$ are non-transit orbits.

The wedge of velocity. To study the projection of the last two categories of orbits in the restricted three-body problem, Conley [19] proved a couple of propositions to determine whether at each position, (\bar{q}_1, \bar{q}_2) , the wedge of velocity exists, in which $q_1^0 p_1^0 > 0$. See the shaded wedges in Figure 2.11. In the current problem, the same behavior is observed. In the next part, the derivation will be given by a more direct method than Conley's, developed in [8] for the more general dissipative system. Note that the orbits with velocity on the boundary of a wedge satisfy $q_1^0 p_1^0 = 0$, making them asymptotic orbits (which will be used in the derivation).

For initial conditions $(\bar{q}_1^0, \bar{q}_2^0, \bar{p}_1^0, \bar{p}_2^0)$ in the original phase space and $(q_1^0, q_2^0, p_1^0, p_2^0)$ in the symplectic eigenspace, we can establish their relations by the symplectic matrix C in (A.16), i.e., $(\bar{q}_1^0, \bar{q}_2^0, \bar{p}_1^0, \bar{p}_2^0)^T = C (q_1^0, q_2^0, p_1^0, p_2^0)^T$. Note that we have $q_1^0 = 0$ and $p_1^0 = 0$ for stable and unstable asymptotic orbits, respectively. We can then express p_1^0 (or q_1^0), q_2^0 , p_2^0 and \bar{p}_2^0 in terms of \bar{q}_1^0 , \bar{q}_2^0 and \bar{p}_1^0 . After substituting q_2^0 and p_2^0 as a function of \bar{q}_1^0 , \bar{q}_2^0 and \bar{p}_1^0 into the Hamiltonian normal form (2.1) we can rewrite (2.1) for asymptotic orbits as,

$$a_p (\bar{p}_1^0)^2 + b_p \bar{p}_1^0 + c_p = 0, \quad (2.67)$$

where a_p , b_p , and c_p are found in Appendix A and depend on $i = 1, 2$ for stable ($q_1^0 = 0$) and unstable ($p_1^0 = 0$) asymptotic orbits, respectively. Thus, we can obtain the strips S_i ($i = 1, 2$) by taking the determinant, $\bar{\Delta} = b_p^2 - 4a_p c_p$, of the quadratic equation (2.67) to be zero (i.e., $\bar{\Delta} = 0$) which are exactly the same expressions as those in (2.65) and (2.66).

For $\bar{\Delta} > 0$, we obtain two real values for \bar{p}_1^0 as,

$$\bar{p}_1^0 = \frac{-b_p \pm \sqrt{b_p^2 - 4a_p c_p}}{2a_p}, \quad (2.68)$$

and then the expression for \bar{p}_2^0 is obtained as,

$$\bar{p}_2^0 = \frac{\bar{p}_1^0 \lambda (1 + c_x + \omega_p^2)}{2(1 + c_x)} + \frac{(1 + c_x - \omega_p^2) [\bar{q}_2^0 \lambda + (1 + c_x) \bar{q}_1^0]}{2(1 + c_x)}. \quad (2.69)$$

Therefore, the two initial velocities formed by the two asymptotic orbits can result in the wedge of velocity with wedge angle $\theta = \arctan(\bar{p}_2^0/\bar{p}_1^0)$.

Up to now, we have obtained the strips and wedge of velocity. In Figure 2.11, S_1 and S_2 are the two strips mentioned above. Outside of each strip S_i ($i = 1, 2$), the sign of q_1^0 and

p_1^0 is independent of the direction of the velocity. These signs can be determined in each of the components of the equilibrium region \mathcal{R} complementary to both strips. For example, in the left-most central components, q_1^0 is negative and p_1^0 is positive, while in the right-most central components q_1^0 is positive and p_1^0 is negative. Therefore, $q_1^0 p_1^0 < 0$ in both components and only non-transit orbits project onto these two components.

Inside the strips the situation is more complicated since the sign of $q_1^0 p_1^0$ depends on the direction of the velocity. For simplicity we have indicated this dependence only on the two vertical bounding line segments in Figure 2.11. For example, consider the intersection of strip S_1 with the left most vertical line. On this subsegment, there is at each point a wedge of velocity in which q_1^0 is positive. The sign of p_1^0 is always positive on this segment, so orbits with velocity interior to the wedge of velocity are transit orbits ($q_1^0 p_1^0 > 0$). Of course, orbits with velocity on the boundary of the wedge are asymptotic ($q_1^0 p_1^0 = 0$), while orbits with velocity outside of the wedge are non-transit ($q_1^0 p_1^0 < 0$). In Figure 2.11, only one transit and one asymptotic orbit starting on this subsegment are illustrated. The situation on the remaining three subsegments is similar.

2.4.3 Analysis in the dissipative system.

Recall that in the dissipative system of the rolling ball on a stationary surface the saddle projection and focus projection in the eigenspace of the conservative system (i.e., the symplectic eigenspace) are uncoupled. The transition is only determined by the location in the saddle projection and energy. However, when the surface is rotating, the situation is different. To compare the behavior in the different systems, we utilize the same change of variables as in (A.16), i.e., $\bar{z} = Cz$, and the equations of motion in the symplectic eigenspace are,

$$\dot{z} = \Lambda z + \Delta z, \tag{2.70}$$

where $\Lambda = C^{-1}MC$ from before, (2.33), but the transformed damping matrix is now,

$$\Delta = C^{-1}DC = c_h K, \tag{2.71}$$

where K is a 4×4 matrix with many non-zero components, given in (A.18).

Notice that for the rolling ball on a stationary surface discussed in Section 2.3.2 and the dynamical buckling of a shallow arch [8] in the dissipative system, the canonical planes

(q_1, p_1) and (q_2, p_2) have their dynamics uncoupled. Here, however, the dynamics on the (q_1, p_1) and (q_2, p_2) planes *are coupled* due to the combination of dissipative and gyroscopic forces. We see this coupling via several coupling terms which are no longer zero in (A.18), e.g., K_{12} , K_{14} , K_{21} and K_{23} , etc. Because of the coupling between the (q_1, p_1) and (q_2, p_2) planes, it is difficult to obtain simple analytical solutions in the symplectic eigenspace variables. Thus, the semi-analytical method which substitutes all the parameters into the equations will be used to analyze the linear behavior near the saddle point.

One can obtain a fourth-order characteristic polynomial for the matrix $\Lambda + \Delta$ from which to obtain eigenvalues. Here we denote the four eigenvalues as $\beta_1, -\beta_2, \beta_{3,4} = -\delta \pm i\omega_d$, where β_1, β_2, δ and ω_d are all positive real numbers. Note that the saddle \times center type equilibrium point in the conservative system becomes a saddle \times focus type equilibrium point in the dissipative system. The four corresponding generalized eigenvectors are denoted as u_1, u_2 and $u_3 \pm iu_4$, where u_i are all real vectors. Thus, the general solutions to system (2.70) can be expressed as,

$$z(t) = k_1^0 u_1 e^{\beta_1 t} + k_2^0 u_2 e^{-\beta_2 t} + e^{-\delta t} \text{Re} [k_0 e^{-i\omega_d t} (u_3 - iu_4)], \quad (2.72)$$

where k_1^0 and k_2^0 are real and $k_0 = k_3^0 + ik_4^0$ is complex (k_3^0 and k_4^0 are real).

The flow in the equilibrium region. Analogous to the discussion for the conservative system, we still choose the same equilibrium region \mathcal{R} determined by $\mathcal{H}_2 = h$ and $|p_1 - q_1| \leq c$ with positive h and c . Due to the coupling between the saddle projection and focus projection, the behavior in the eigenspace is complicated. When $t \rightarrow +\infty$ and $t \rightarrow -\infty$, z is dominated by the k_1^0 term and k_2^0 term, respectively. Thus, one can categorize the orbits into different groups based solely on the signs of k_1^0 and k_2^0 . However, the visualization of all the initial conditions for different types of orbits specified by a given energy is indirect. To do so, setting the initial conditions in the symplectic eigenspace as $z_0 = (q_1^0, q_2^0, p_1^0, p_2^0)$, the following relation between the symplectic and dissipative eigenspace variables is obtained:

$$\begin{pmatrix} q_1^0 \\ q_2^0 \\ p_1^0 \\ p_2^0 \end{pmatrix} = \begin{pmatrix} \vdots & \vdots & \vdots & \vdots \\ u_1 & u_2 & u_3 & u_4 \\ \vdots & \vdots & \vdots & \vdots \end{pmatrix} \begin{pmatrix} k_1^0 \\ k_2^0 \\ k_3^0 \\ k_4^0 \end{pmatrix}, \quad (2.73)$$

where the eigenvectors u_i are written as column vectors.

As discussed for the conservative system, asymptotic orbits play an important role, acting as the separatrix of transit orbits and non-transit orbits. Moreover, the size of stable asymptotic orbits determines the amount of transit orbits. A straightforward method to obtain the stable asymptotic orbits, analogous to what was done for the conservative case, is as follows. For the stable asymptotic orbits, we have $k_1^0 = 0$. Then we can use (2.73) to obtain k_i^0 ($i = 2, 3, 4$) and p_2^0 in terms of q_1^0 , q_2^0 and p_1^0 . Analogous to the situation for the conservative system in Section 2.2.1, we select the initial conditions on two sets n_1 and n_2 projecting to the line segments $p_1^0 = q_1^0 \pm c$. Substituting p_2^0 in terms of q_1^0 , q_2^0 and p_1^0 and the relation $q_1^0 = p_1^0 \mp c$ into the Hamiltonian normal form (2.1), we rewrite it in exactly the same form as in (2.67): $a_p (p_1^0)^2 + b_p p_1^0 + c_p = 0$. Note that here a_p , b_p and c_p are functions of q_{20} which are different to that in (2.67). To guarantee p_1^0 has real solutions, $\bar{\Delta} = b_p^2 - 4a_p c_p > 0$ should be true. Thus, we can obtain $q_{20}^{(l)} < q_2^0 < q_{20}^{(u)}$, where $q_{20}^{(l)}$ and $q_{20}^{(u)}$ are the lower and upper bounds for q_2^0 . For different $q_2^0 \in [q_{20}^{(l)}, q_{20}^{(u)}]$, we can obtain $p_1^0 = (-b_p \pm \sqrt{b_p^2 - 4a_p c_p}) / (2a_p)$ and thus obtain q_1^0 and p_2^0 .

Null space method. Another method to obtain the stable asymptotic orbits, here called the **null space method**, can also be utilized. The procedure is as follows: (1) using three generalized eigenvectors corresponding to the eigenvalues with negative real part (i.e., u_2, u_3, u_4), the null space of the stable eigenspace, $E^s = \text{span}\{u_2, u_3, u_4\}$, can be obtained, denoted as $u_n = (u_{n1}, u_{n2}, u_{n3}, u_{n4})^T$, with the relation $u_n \cdot u_i = 0$ ($i = 2, 3, 4$); (2) Since the initial conditions z_0 of forward asymptotic orbits (i.e., stable asymptotic orbits) should be normal to the null space, we have $u_n \cdot z_0 = 0$, which, along with the Hamiltonian function, will give the same quadratic equation, $a_p (p_1^0)^2 + b_p p_1^0 + c_p = 0$; (3) following the same manipulation as described in the previous paragraph, we obtain the same results.

Flow in the equilibrium region. Different combinations of the signs of k_1^0 and k_2^0 give nine classes of orbits which can be grouped into the same four categories as the dissipative system of the rolling ball on a stationary surface. All initial conditions on the bounding lines n_1 and n_2 for different types of orbits can be visualized based on the analysis listed below.

1. Orbits with $k_1^0 = k_2^0 = 0$ corresponds to a focus-type asymptotic orbit with motion in the (q_2, p_2) plane (see black dot at the origin of the (q_1, p_1) plane in Figure 2.12). Due

to the effect of energy dissipation, the periodic orbit does not exist.

2. Orbits with $k_1^0 k_2^0 = 0$ are saddle-type asymptotic orbits. For example, the bolded orange line on the bounding line n_1 in the saddle projection associated with the closed solid curve in the focus projection in Figure 2.12 represents all the initial conditions for the stable asymptotic orbits with initial conditions of initial energy h on n_1 . Because of the coupling between the saddle projection and focus projection, one point on the closed solid curve in the focus projection has a corresponding point on the bolded region in saddle projection which together give the initial condition for a specific asymptotic orbit of initial energy h . See the orange dots for the initial condition of the stable asymptotic orbit starting from n_1 and orange curve for the evolution. Of course, the bounding line n_2 has the behavior for the stable asymptotic orbits. Since the system just has one positive eigenvalue, the unstable asymptotic orbits just have one specific direction along each side of the saddle point. See the orange straight lines for the unstable asymptotic orbits. Four asymptotic orbits are shown in Figure 2.12 labeled A.
3. The segments determined by $k_1^0 k_2^0 < 0$ which cross \mathcal{R} from the bounding line n_1 to the bounding line n_2 in the northern hemisphere, and vice versa in the southern hemisphere, correspond to the transit orbits with initial energy h on n_1 and n_2 , respectively. See the two example orbits labeled T of Figure 2.12.
4. Finally the segments with $k_1^0 k_2^0 > 0$ which start from one hemisphere and bounce back are the non-transit orbits of initial energy h . See the two orbits labeled NT in Figure 2.12.

McGehee representation. The previous section gives the topological structure of initial conditions for different types of orbits in the dissipative system, but it still may not be intuitive. Thus, as we did in the rolling ball on a stationary surface, we introduce the McGehee representation to visualize the region \mathcal{R} for easier interpretation. Since there are many curves on the two 2-spheres, n_1 and n_2 , of initial energy h , we show the two spheres separately in Figure 2.13(c).

As mentioned in the ball rolling on a stationary surface with damping, the McGehee representation gives the spheres with the same energy h so that here the McGehee representation

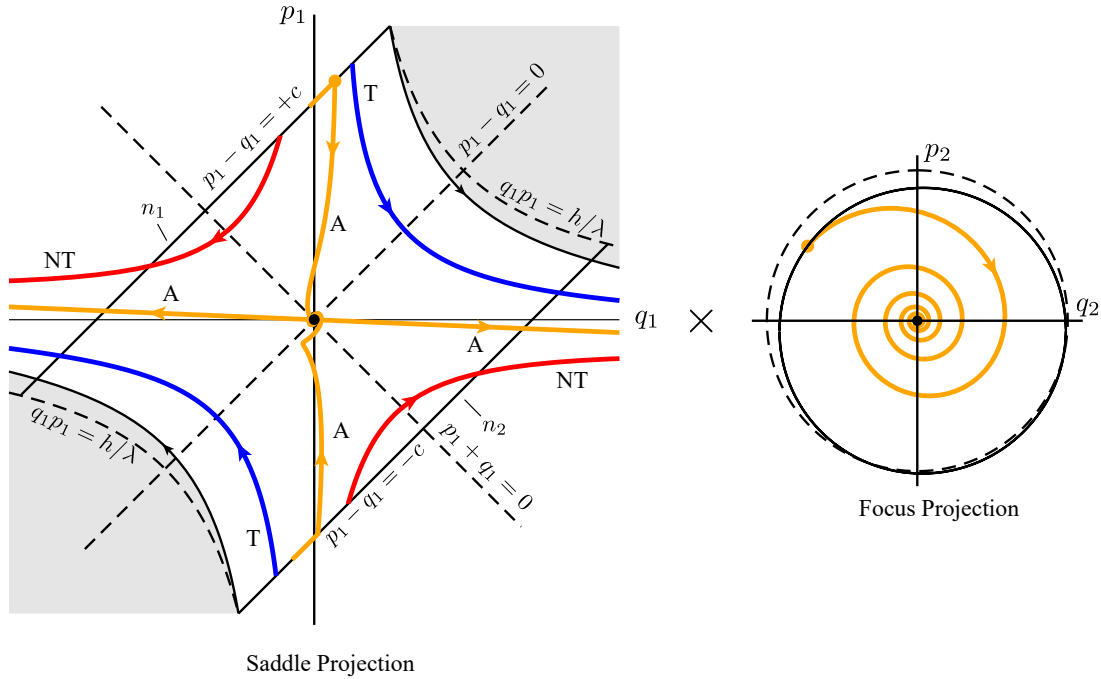


Figure 2.12: The flow in the equilibrium region \mathcal{R} projected onto (q_1, p_1) plane and (q_2, p_2) plane which are coupled has form saddle \times focus. Shown are the saddle-type asymptotic orbits (labeled A), transit orbits (labeled T) and non-transit orbits (labeled NT). The dot at the origin of (q_1, p_1) plane is the focus-type asymptotic orbits with projection only on (q_2, p_2) plane which is a damped oscillator decaying to the origin. Due to the coupling between (q_1, p_2) plane and (q_2, p_2) plane, the initial conditions for the three-dimensional stable asymptotic orbit are dependent on the angle in focus projection. The one dimensional unstable asymptotic orbits are a straight line in the saddle projection.

again just shows the initial conditions on each bounding sphere. The symbols in Section 2.2.2 have the same meaning as used here. The previous four categories of orbits are interpreted as follows.

1. There is a 1-sphere S_h^1 in the region \mathcal{R} , similar to that in the rolling ball on a stationary surface with dissipation, which is the equator of the 2-sphere given by $p_1 - q_1 = 0$. The set S_h^1 gives the initial conditions for the focus-type asymptotic orbits with initial energy h . Readers are referred to the dot in Figure 2.6(b) for interpretation.
2. There are two 1-spheres represented by the orange closed curves on each bounding sphere, denoted by a_i^+ and a_i^- on sphere n_i . They give the initial conditions for stable asymptotic orbits. Compared to the ball rolling on a stationary surface, which has

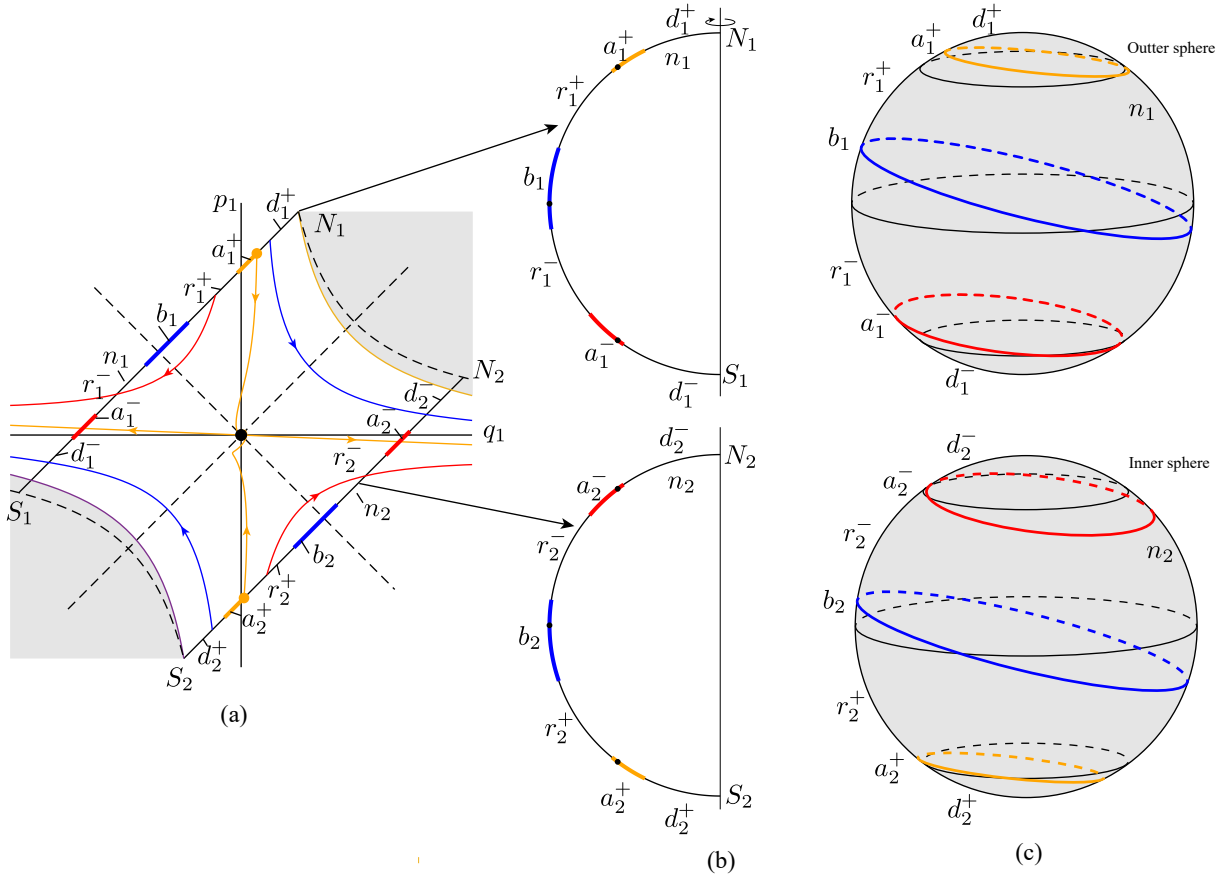


Figure 2.13: The McGehee representation of the equilibrium region for dissipative system of rolling ball on a rotating surface. (a) The projection of flow onto (q_1, p_1) plane. (b) The projection of the flow in the \mathcal{R} region of the energy surface onto a cross-section. (c) The McGehee representation of the flow on the boundaries of the \mathcal{R} region, highlighting the features on the bounding spheres n_1 and n_2 , the “inner” and “outer” spheres, respectively.

initial conditions for stable asymptotic orbits given by circles on the bounding spheres parallel to the corresponding equators, initial conditions for stable asymptotic orbits for the rotating surface are tilted. This is due to *dissipation-induced coupling* of the saddle and focus projections of the symplectic eigenspace. Note that the unstable asymptotic orbits are one-dimensional and have different energy from the bounding sphere so that they cannot be given in the McGehee representation.

3. Consider the two spherical caps on each bounding 2-sphere denoted by d_1^+ , d_1^- and d_2^+ , d_2^- . The transit orbits with initial conditions on spherical cap d_1^+ , which is in n_1^+ and

bounded by a_1^+ , enter \mathcal{R} and leave through n_2 at a different (lower) energy, due to dissipation. On the other hand, the transit orbits with initial conditions on spherical cap d_1^- in n_1^- bounded by a_1^- are leaving \mathcal{R} having entered through n_2 at a different (higher) energy. An analogous situation holds on bounding sphere n_2 .

4. There is a 1-sphere of tangency points, denoted by b , with initial conditions on which the orbits do not enter \mathcal{R} locally. To obtain the tangency points, first we need to recognize the relation along each angle θ in the focus projection, i.e. $p_2^0 = q_2^0 \tan \theta$, as well as the initial conditions on the bounding spheres n_1 and n_2 , i.e. $p_1^0 = q_1^0 \pm c$, and the tangency conditions, i.e. $\dot{p}_1^0 = \pm \dot{q}_1^0$. We then substitute such relations into the Hamiltonian normal form to yield a quadratic equation which will give two tangency points along that angle. Note that the 1-spheres here are not the equators of the bounding spheres, as they are in the non-rotating case, but are tilted by an angle compared with the conservative system, again, due to the coupling via the dissipation matrix K , from (A.18). The topological hemisphere above b_1 in n_1 is referred to as n_1^+ and below b_1 as n_1^- ; similarly for n_2 , as illustrated in Figure 2.13(c). Similar to before, the non-transit orbits with initial conditions of initial energy h on spherical zone r_i^+ , in n_i^+ bounded by a_i^+ and b_i , are entering \mathcal{R} and non-transit orbits with initial conditions on spherical zone r_i^- , in n_i^- bounded by a_i^- and b_i , are leaving \mathcal{R} .

Trajectories in the equilibrium region. Following the standard procedure to solve (2.58), we get the eigenvalues of the matrix $M + D$ (denoted as $\bar{\beta}_1, -\bar{\beta}_2, \bar{\beta}_{3,4} = -\bar{\delta} \pm i\bar{\omega}_d$, where $\bar{\beta}_1, \bar{\beta}_2, \bar{\delta}$ and $\bar{\omega}_d$ are positive real values) associated with the corresponding generalized eigenvectors (denoted as \bar{u}_i ($i = 1, 2, 3, 4$)). The general real solutions to (2.58) are,

$$\bar{z}(t) = \bar{k}_1^0 \bar{u}_1 e^{\bar{\beta}_1 t} + \bar{k}_2^0 \bar{u}_2 e^{-\bar{\beta}_2 t} + e^{-\bar{\delta} t} \text{Re} \left[\bar{k}_0 e^{-i\bar{\omega}_d t} (\bar{u}_3 - i\bar{u}_4) \right], \quad (2.74)$$

where \bar{k}_1^0 and \bar{k}_2^0 are real and $\bar{k}_0 = \bar{k}_3^0 + i\bar{k}_4^0$ is complex. By inspecting the limiting behavior of \bar{q}_1 as t tends to plus or minus infinity, we can also obtain the following four categories of orbits:

1. Orbits with $\bar{k}_1^0 = \bar{k}_2^0 = 0$ are focus-type asymptotic orbits. When dissipation is considered in the system, the periodic orbit does not exist, but these initial conditions correspond to purely focus-like dynamics, with an amplitude decreasing proportional to $e^{-\bar{\delta} t}$.

2. Orbits with $\bar{k}_1^0 = 0$ (or $\bar{k}_2^0 = 0$) are stable (or unstable) saddle-type asymptotic to the saddle equilibrium point.
3. Orbits with $\bar{k}_1^0 \bar{k}_2^0 > 0$ are transit orbits.
4. Orbits with $\bar{k}_1^0 \bar{k}_2^0 < 0$ are non-transit orbits.

Wedge of velocity and ellipse of transition. As discussed previously, for this rotating system one also obtains an *ellipse of transition* which confines the existence of transit orbits. Inside the ellipse, the transit orbits exist, while outside the ellipse transit orbits do not exist. As before, a non-empty wedge of velocity, which divides the transit orbits from the non-transit orbits, can only exist inside the ellipse of transition.

Taking $t = 0$, one obtains the relation between the initial conditions $\bar{z}_0 = (\bar{q}_1^0, \bar{q}_2^0, \bar{p}_1^0, \bar{p}_2^0)$ and the coefficients \bar{k}_i^0 with a similar form as in (2.73). For stable asymptotic orbits, i.e., $\bar{k}_1^0 = 0$, we can determine the coefficients $\bar{k}_i^0 (i = 2, 3, 4)$ and \bar{p}_{20} in terms of initial conditions $\bar{q}_{10}, \bar{q}_{20}, \bar{p}_{10}$. With the substitution of $\bar{q}_1^0, \bar{q}_2^0, \bar{p}_1^0$ and \bar{p}_2^0 into (2.60), the quadratic Hamiltonian (2.60) restricted by energy h can be rewritten as a second order algebraic equation for \bar{p}_1^0 which has exactly the same form as (2.67), but with different a_p, b_p and c_p in terms of \bar{q}_1^0 and \bar{q}_2^0 . On the one hand, for the critical condition, i.e., $\Delta = b_p^2 - 4a_p c_p = 0$, we can obtain an ellipse of transition which is different from the strips S_1 in the conservative system. The ellipse limits the location of transit orbit initial conditions. On the other hand, when the determinant satisfies $\Delta = b_p^2 - 4a_p c_p > 0$, \bar{p}_1^0 has two real solutions, $\bar{p}_1^0 = (-b_p \pm \sqrt{b_p^2 - 4a_p c_p}) / (2a_p)$, associated with two real solutions for \bar{p}_2^0 . Thus, the two pairs of results of $(\bar{p}_1^0, \bar{p}_2^0)$ will determine two bounding directions of velocity, which form the wedge of velocity.

Figure 2.14 shows the flow in the projection of the equilibrium region \mathcal{R} to position space, taking gyroscopic and dissipative effects into consideration. Due to energy dissipation, the strips which are the boundaries of asymptotic orbits in the position space of the conservative system no longer exist. In particular, the strip for the stable asymptotic orbit is replaced by the ellipse of transition. The ellipse of transition, similar to the role in the rolling ball on a stationary surface, confines the existence of transit orbits. That is, transit orbits of a given initial energy h must have initial conditions inside the ellipse of transition, while only non-transit orbit initial conditions project onto the area complementary of the ellipse. However, even if the initial condition of an orbit projects to a position inside the ellipse of transition, this alone does not guarantee the transition. This is a necessary but not a

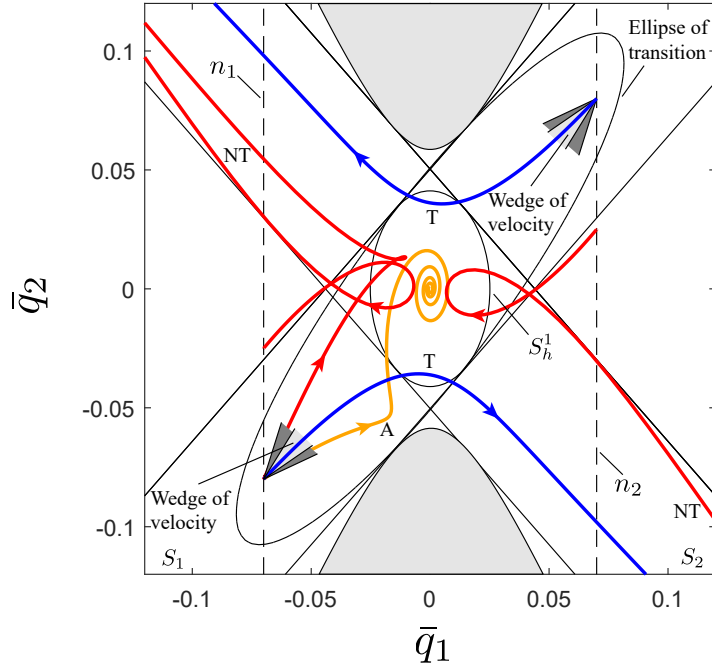


Figure 2.14: The flow in the equilibrium region \mathcal{R} of position space. Shown are the saddle-type asymptotic orbit; two transit orbits; three non-transit orbits. For the same given energy, the wedges of velocity for the dissipative system (the smaller light grey shaded wedges), restricted by the ellipse of transition, partially cover the wedges of velocity for the conservative system (the larger dark grey shaded wedges) restricted by a strip.

sufficient condition. The additional condition is that the velocity should be along certain directions. The wedge of velocity obtained above, which is non-empty only inside the ellipse, is exactly the condition providing the correct range of directions for the velocity of transit orbits. Orbits with initial conditions interior to the wedge can transit, while orbits with velocity outside the wedge cannot transit. The orbits with velocity on the boundary of the wedge are asymptotic to the equilibrium point.

The sizes of the wedge of velocity and ellipse of transition, which both represent the proportion of transit orbits compared to non-transit orbits, are dependent on the energy, h , and the amount of damping, c_h . An increase of energy gives more transit orbits, while an increase in damping reduces the proportion of transit orbits. Furthermore, different positions inside the ellipse have different sizes of wedges of velocity. The closer the position is to the boundary of the ellipse of transition, the smaller the size of the wedge of velocity will be. From

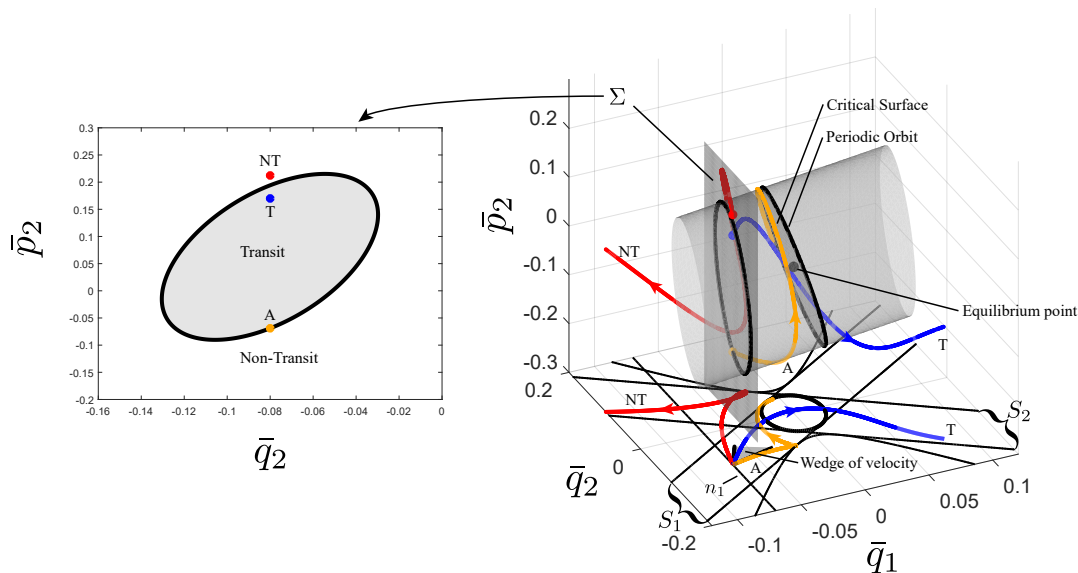


Figure 2.15: Transition tube for the ball rolling on a rotating surface. The left figure gives the region for initial conditions of transit orbits on the Poincaré section Σ with three initial conditions (the dots) for three types of orbits. The right shows the transition tube for a given energy. The critical surface playing the same role as the ball rolling on a stationary surface also exists here. Three types of orbits with initial conditions on the left figure are given.

Figure 2.14, we find that the size of the wedge shrinks (light grey) compared with that of the conservative system (dark grey) which qualitatively indicates how damping affects the wedge of velocity.

2.4.4 Transition tube and transition ellipsoid

We have discussed the flow in the position space for a rolling ball on a rotating surface near a saddle point. In this section, we will visualize the structures governing transitions in the phase space, particularly on surfaces of constant initial energy h .

For the rolling ball on a stationary surface, we obtained the transition tube and transition ellipsoid that give all the initial conditions, starting at a given initial energy h , of transit orbits for the conservative system and dissipative system, respectively. In the current problem, we have similar phase space structures governing the transition which can be obtained by the semi-analytical method mentioned before. Figure 2.15 and Figure 2.16 show the

transition tube and transition ellipsoid, respectively. As discussed in Section 2.3.3, for a specific energy all transit orbits in the conservative system and dissipative system must have initial conditions inside the transition tube and transition ellipsoid, respectively; all orbits with initial conditions outside the transition tube and transition ellipsoid are non-transit orbits. Furthermore, the critical surface divides the transition tube and transition ellipsoid into two parts. Orbits with initial conditions inside the left part will transit to the right and orbits with initial conditions inside the right part will transit to the left. Orbits on the boundary are asymptotic to the periodic orbit (respectively, equilibrium point) in the conservative (respectively, dissipative) system. Transit orbits can cross the critical surface, while non-transit orbits will bounce back before reaching the critical surface.

Figure 2.15 and Figure 2.16 also give different types of orbits with the initial conditions on the same Poincaré section in the corresponding system. This illustrates the discussion given above that transit orbits must have initial conditions inside the transition tube or transition ellipsoid. In fact, the transit orbit (initial condition marked T in Figure 2.15) in the conservative system and the non-transit orbit (initial condition marked NT in Figure 2.16) in the dissipative system have the same initial condition. This demonstrates that initial conditions corresponding to a transit orbit in the conservative system may be non-transit orbits if damping is taken into account.

It is worth noting that the topological structures in phase space controlling the transition for both the non-rotating system and rotating system are almost the same. Nevertheless, differences exist between these two systems. In the non-rotating system, the axes of the transition tube and transition ellipsoid are parallel to the position space axes, while in the rotating system, the axes of the transition tube and transition ellipsoid are not parallel to the position space axes, but are tilted by an angle.

2.5 Conclusions and future work

We have discussed the escape (or transition) geometry of a rolling ball on a stationary and rotating surface when dissipative and/or gyroscopic forces are both present. Since escape occurs through a saddle point in all of these problems, we focused on the local behavior near the equilibrium neck region around the saddle. The problems are classified into two categories based on the coupling conditions between the saddle and focus canonical planes

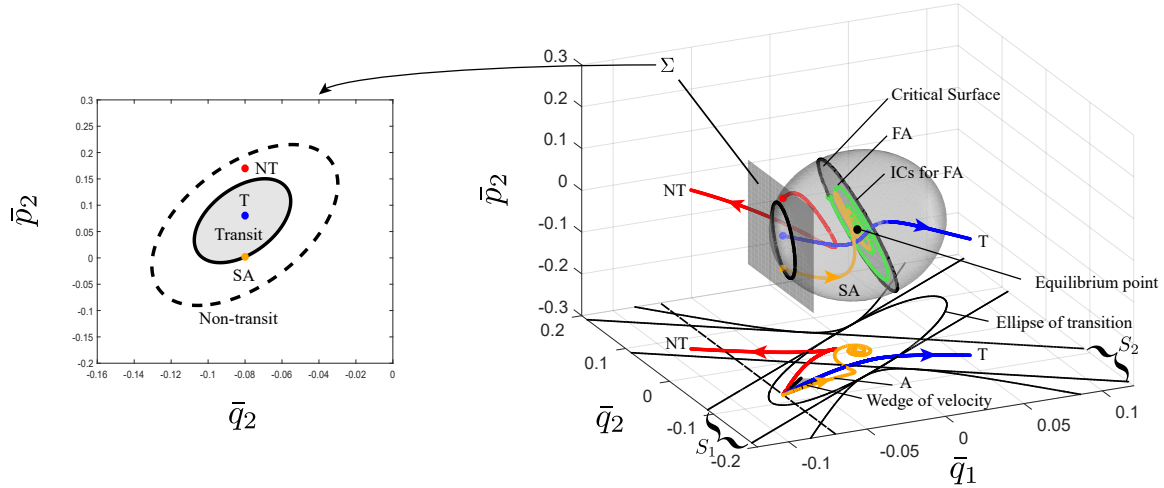


Figure 2.16: Transition ellipsoid for the dissipative system in the rolling ball on a rotating surface. The left figure shows the Poincaré section Σ , where the dots are the initial conditions for the corresponding trajectories and the solid ellipse is the boundary of initial conditions for the transit orbits. For comparison, the dashed ellipse of tube boundary for the conservative system is also given. The right figure shows the transition tube with three different types of orbits with initial conditions on the left figure.

in the symplectic eigenspace.

We define a transition region, \mathcal{T}_h , as the region of initial conditions of a given initial energy h which transit from one side of a saddle to the other. The boundary of the transition region, $\partial\mathcal{T}_h$, is a co-dimension 1 boundary on each surface of initial energy. For conservative systems $\partial\mathcal{T}_h$ is a tube (topologically, a cylinder), while for dissipative systems, $\partial\mathcal{T}_h$ is an ellipsoid (topologically, a 2-sphere). These topological results carry over to the nonlinear setting via the stable manifold theorem [30] and a theorem of Moser [31, 32], for the dissipative and conservative cases, respectively. Trajectories with initial conditions outside of $\partial\mathcal{T}_h$ do not escape from one side of the saddle to the other. The transition tube and transition ellipsoid are divided into two parts by a critical surface; trajectories with initial conditions on the left part (respectively, right part) can transit to the right part (respectively, left part). The projection of the transition tube and transition ellipsoid onto configuration space are a strip and ellipse of transition, respectively. An initial configuration within the strip (respectively, ellipse) is a necessary condition for a transit orbit. The necessary velocity conditions at a specific configuration point within the strip (respectively, ellipse) are given by a wedge of

velocity at that point.

In this study, we investigated only the local behavior around the saddle equilibrium revealing the phase space structure that governs the escape or transition, and did not consider the global behavior. A continuation of the study on escape dynamics can apply this theory to more complicated applications. However, based on the theorems given above, all the qualitative results of our discussion carry over to the full nonlinear equations, including the topology of $\partial\mathcal{T}_h$. The bisection method presented in [8] is a useful tool to find $\partial\mathcal{T}_h$ in the global setting. A more direct method is to determine the stable manifold of the saddle point, as foliated by energy, which provides another way to compute $\partial\mathcal{T}_h$. In future work, both methods will be carried out. Furthermore, higher degree of freedom systems will be considered and the topological results are expected to generalize for the dynamics across index-1 saddles; that is, the $(2N - 2)$ -dimensional boundary of transit orbits starting at same initial energy h in N degrees of freedom, $\partial\mathcal{T}_h$, which are hyper-cylinders (topology $S^{2N-3} \times \mathbb{R}$) in the conservative setting become hyper-ellipsoids in the phase space (topology S^{2N-2}) with the addition of dissipation.

Acknowledgements This work was supported in part by the National Science Foundation under award 1537349. We thank Yue Guan, Shibabrat Naik, Lawrie Virgin, and Yawen Xu for several stimulating conversations on these topics and suggestions of examples to consider. We also thank an anonymous reviewer who gave several suggestions improving the quality of the paper.

Bibliography

- [1] D. T. Greenwood, *Advanced Dynamics*, Cambridge University Press, 2006.
- [2] A. M. Bloch, P. Hagerty, A. G. Rojo, M. I. Weinstein, Gyroscopically stabilized oscillators and heat baths, *Journal of Statistical Physics* 115 (3-4) (2004) 1073–1100.
- [3] R. Krechetnikov, J. E. Marsden, Dissipation-induced instabilities in finite dimensions, *Reviews of Modern Physics* 79 (2) (2007) 519.
- [4] O. Bottema, Stability of equilibrium of a heavy particle on a rotating surface, *Zeitschrift für Angewandte Mathematik und Physik ZAMP* 27 (5) (1976) 663–669.
- [5] O. N. Kirillov, Brouwer’s problem on a heavy particle in a rotating vessel: Wave propagation, ion traps, and rotor dynamics, *Physics Letters A* 375 (15) (2011) 1653–1660.
- [6] F. Gabern, W. S. Koon, J. E. Marsden, S. D. Ross, Theory and computation of non-RRKM lifetime distributions and rates in chemical systems with three or more degrees of freedom, *Physica D: Nonlinear Phenomena* 211 (3-4) (2005) 391–406.
- [7] W. S. Koon, M. W. Lo, J. E. Marsden, S. D. Ross, *Dynamical Systems, the Three-Body Problem and Space Mission Design*, Marsden Books, ISBN 978-0-615-24095-4, 2011.
- [8] J. Zhong, L. N. Virgin, S. D. Ross, A tube dynamics perspective governing stability transitions: An example based on snap-through buckling, *International Journal of Mechanical Sciences* 149 (2018) 413–428.
- [9] S. Naik, S. D. Ross, Geometry of escaping dynamics in nonlinear ship motion, *Communications in Nonlinear Science and Numerical Simulation* 47 (2017) 48 – 70, ISSN 1007-5704.
- [10] S. D. Ross, A. E. BozorgMagham, S. Naik, L. N. Virgin, Experimental validation of phase space conduits of transition between potential wells, *Physical Review E* 98 (2018) 052214.

- [11] C. D. Murray, S. F. Dermott, *Solar System Dynamics*, Cambridge University Press, Cambridge, 1999.
- [12] V. Szebehely, *Theory of Orbits: The Restricted Problem of Three Bodies*, Academic, New York, 1967.
- [13] J. Zhong, S. D. Ross, Geometry of escape and transition dynamics in the presence of dissipative and gyroscopic forces in two degree of freedom systems, *Communications in Nonlinear Science and Numerical Simulation* 82 (2020) 105033.
- [14] S. Wiggins, L. Wiesenfeld, C. Jaffé, T. Uzer, Impenetrable barriers in phase-space, *Physical Review Letters* 86 (24) (2001) 5478.
- [15] C. Jaffé, S. D. Ross, M. W. Lo, J. Marsden, D. Farrelly, T. Uzer, Statistical theory of asteroid escape rates, *Physical Review Letters* 89 (1) (2002) 011101.
- [16] W. S. Koon, M. W. Lo, J. E. Marsden, S. D. Ross, Heteroclinic connections between periodic orbits and resonance transitions in celestial mechanics, *Chaos* 10 (2000) 427–469.
- [17] S. Wiggins, *Normally Hyperbolic Invariant Manifolds in Dynamical Systems*, Springer-Verlag, New York, 1994.
- [18] R. McGehee, Some homoclinic orbits for the restricted three-body problem, Ph.D. thesis, University of Wisconsin, Madison, 1969.
- [19] C. C. Conley, Low energy transit orbits in the restricted three-body problem, *SIAM Journal on Applied Mathematics* 16 (1968) 732–746.
- [20] A. D. Lewis, R. M. Murray, Variational principles for constrained systems: theory and experiment, *International Journal of Non-Linear Mechanics* 30 (6) (1995) 793–815.
- [21] L. N. Virgin, T. C. Lyman, R. B. Davis, Nonlinear dynamics of a ball rolling on a surface, *American Journal of Physics* 78 (3) (2010) 250–257.
- [22] Y. Xu, L. N. Virgin, S. D. Ross, On experimentally locating saddle-points on a potential energy surface from observed dynamics, *Mechanical Systems and Signal Processing* 130 (2019) 152 – 163, ISSN 0888-3270.
- [23] J. E. Marsden, T. S. Ratiu, *Introduction to Mechanics and Symmetry*, Springer, 2013.
- [24] J. D. Meiss, *Differential Dynamical Systems*, SIAM, 2007.

- [25] E. E. Zotos, Escapes in Hamiltonian systems with multiple exit channels: Part I, *Nonlinear Dynamics* 78 (2) (2014) 1389–1420.
- [26] E. E. Zotos, An overview of the escape dynamics in the Hénon-Heiles Hamiltonian system, *Meccanica* 52 (11-12) (2017) 2615–2630.
- [27] S. D. Ross, Cylindrical manifolds and tube dynamics in the restricted three-body problem, Ph.D. thesis, California Institute of Technology, 2004.
- [28] R. I. Thompson, T. J. Harmon, M. G. Ball, The rotating-saddle trap: A mechanical analogy to RF-electric-quadrupole ion trapping?, *Canadian Journal of Physics* 80 (12) (2002) 1433–1448.
- [29] L. E. J. Brouwer, The motion of a particle on the bottom of a rotating vessel under the influence of the gravitational force, H. Freudenthal (North-Holland, Amsterdam, 1975) (1918) 665–686.
- [30] S. Wiggins, Introduction to Applied Nonlinear Dynamical Systems and Chaos, vol. 2 of *Texts in Applied Mathematics Science*, Springer-Verlag, Berlin, 2nd edn., 2003.
- [31] J. Moser, On the generalization of a theorem of A. Liapounoff, *Communications on Pure and Applied Mathematics* 11 (2) (1958) 257–271.
- [32] J. Moser, *Stable and Random Motions in Dynamical Systems with Special Emphasis on Celestial Mechanics*, Princeton University Press, 1973.

Chapter 3

A tube dynamics perspective governing stability transitions: An example based on snap-through buckling

Attribution

This chapter represents part of a collaborative work with Lawrence N. Virgin and Shane D. Ross which is published in the *International Journal of Mechanical Sciences*, 149 (2018), 413-428. The online version of the article can be found at <https://doi.org/10.1016/j.ijmecsci.2017.10.040>.

Abstract

The equilibrium configuration of an engineering structure, able to withstand a certain loading condition, is usually associated with a local minimum of the underlying potential energy. However, in the nonlinear context, there may be other equilibria present, and this brings with it the possibility of a transition to an alternative (remote) minimum. That is, given a sufficient disturbance, the structure might buckle, perhaps suddenly, to another shape. This study considers the dynamic mechanisms under which such transitions (typically via saddle points) occur. A two-mode Hamiltonian is de-

veloped for a shallow arch/buckled beam. The resulting form of the potential energy—two stable wells connected by rank-1 saddle points—shows an analogy with resonance transitions in celestial mechanics or molecular reconfigurations in chemistry, whereas here the transition corresponds to switching between two stable structural configurations. Then, from Hamilton’s equations, the analytical equilibria are determined and linearization of the equations of motion about the saddle is obtained. After computing the eigenvalues and eigenvectors of the coefficient matrix associated with the linearization, a symplectic transformation is given which puts the Hamiltonian into normal form and simplifies the equations, allowing us to use the conceptual framework known as tube dynamics. The flow in the equilibrium region of phase space as well as the invariant manifold tubes in position space are discussed. Also, we account for the addition of damping in the tube dynamics framework, which leads to a richer set of behaviors in transition dynamics than previously explored.

3.1 Introduction

The nonlinear behavior of slender structures under loading is often dominated by a potential energy function that possesses a number of stationary points corresponding to various equilibrium configurations [1, 2]. Some are stable (local minima, or ‘well’), some are unstable (local maxima or ‘hill-top’), and some correspond to saddle points, i.e., a shape with opposite curvature in different directions, but still unstable, having both stable and unstable directions. Interestingly, although difficult to observe experimentally, it is these saddle points that can have a profound organizing effect on global trajectories in a dynamics context. Thus, under a nominally fixed set of loads or a given configuration we may have the situation in which a system is at rest in a position of stable equilibrium, but, given sufficiently large perturbation (input of energy) may transition to a remote stable equilibrium [3], or even collapse completely [4, 5]. The path taken during this transition is associated with the least energetic route, and this will typically correspond to a passage close to a saddle point: it is easier to take a path around a mountain than going directly over its peak.

For a single mechanical degree of freedom the transition from one potential energy minimum to another is relatively unambiguous [6, 7]. We can think of a twin-well oscillator and how it has no choice but to pass over an intermediate hilltop in transitioning to an adjacent minimum. For high-order systems trajectories have many more possible paths. But a system with two mechanical degrees of freedom (configuration space), and thus a 4 dimensional phase space, offers an intermediate situation: compelling conceptual clarity (i.e., the potential energy can be thought of as a surface or landscape), but still retaining a wider range of potential behavior over and above the aforementioned single oscillator (i.e., multiple ways of traversing and perhaps escaping from one potential well to another).

For the two degree of freedom system, the analog of the hilltop is the saddle point of the potential energy surface. The linearized dynamics near such a point yields an oscillatory mode and an exponential mode, with both asymptotically stable and unstable directions. For energies slightly above the saddle point, there is a bottleneck to the energy surface [8, 9]. Transitions from one side of the bottleneck can be understood in terms of sets of trajectories which are bounded by topological cylinders. The transition dynamics, which has in some contexts been known as tube dynamics [9, 10, 11, 12, 13, 14, 15, 16, 17, 18, 19], has been developed for studying transitions between stable states (the potential wells) in a number of disparate contexts, and here it is applied to a structural mechanics situation in which snap-through buckling [2] is the key phenomenological transition. Conditions are determined whereby the initial energy imparted to the system is characterized in terms of subsequent escape from the initial potential well.

3.2 The Paradigm: Snap-through of an Arch/Buckled Beam

A classic example of a saddle-node bifurcation in structural mechanics is the symmetric snap-through buckling of a shallow arch, in an essentially co-dimension 1 bifurcation [7]. However, if the arch (or equivalently a buckled beam) is *not* shallow then the typical mechanism of instability is an asymmetric snap-through, requiring two modes (symmetric and asymmetric) for characterization, and the instability corresponds to a subcritical pitchfork bifurcation. In both of these cases the transition is sudden and associated with a fast dynamic jump, since there is no longer any locally available stable equilibrium. This behavior is generic regardless of boundary conditions and is also exhibited by the laterally-loaded buckled beam [20, 21]. We shall focus on this latter example, for relative simplicity of introduction. The essential focus here is that the underlying potential energy of this system consists of two potential energy wells (the original unloaded equilibrium and the snapped-through equilibrium), an unstable hilltop (the intermediate, straight, unstable equilibrium) and two saddle-points. The symmetry of this system is broken by small geometric imperfections. The question is: *how does the system escape its local potential energy well* in a dynamical systems sense?

Suppose we have a moderately buckled beam. If a central point load is applied then the beam deflects initially in a purely symmetric mode, as shown by the red line in Figure 3.1(a), following the α loading path. Upon a quasi-static increase in the load P , point C is reached (a subcritical pitchfork bifurcation) and the arch quickly snaps-through (a thoroughly dynamic event) with a significant asymmetric component in the deflection and the system settles into its inverted position

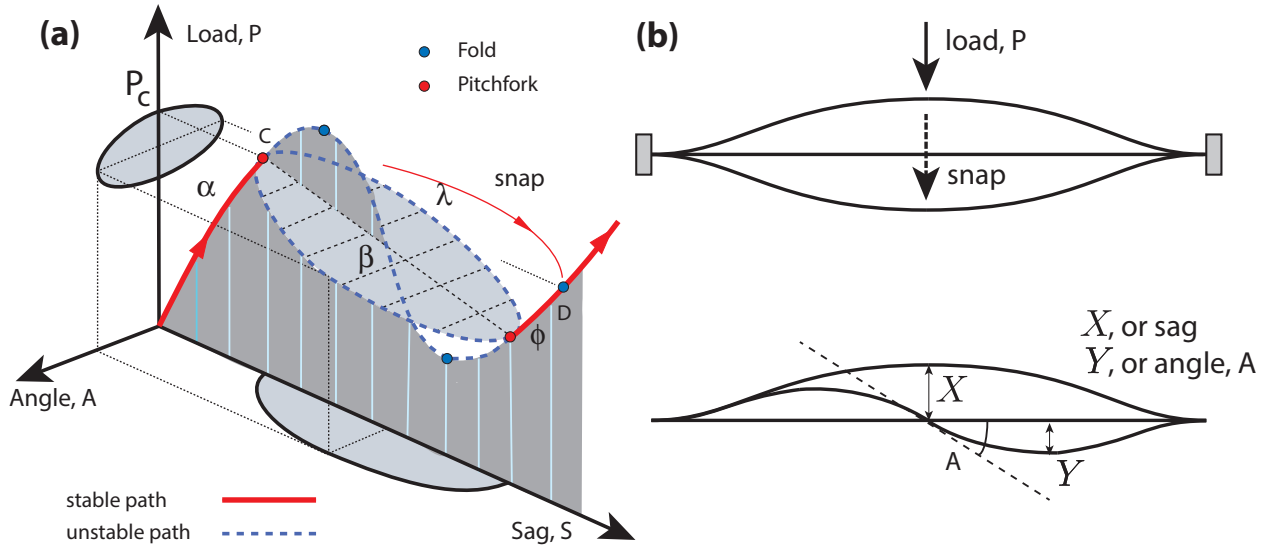


Figure 3.1: (a) A schematic load-deflection characteristic, (b) the two dominant degrees of freedom.

D [3]. This behavior is captured by considering a two-mode analysis: sag S (symmetric) and angle A (asymmetric), or alternatively we can use the harmonic coordinates X and Y , respectively, corresponding to the modes in part (b). In an approximate analysis they might be the lowest two buckling modes or free vibration modes from a standard eigen-analysis. Suppose we load the beam to a value slightly below the snap value at P_C , and fix it at that value. In this case there will be the five equilibria mentioned earlier: three equilibria purely in sag (two stable and an unstable one between them), and two saddles, with significant angular components but geometrically opposed [1]. Small geometric imperfections (in A and/or S) will break the symmetry and influence which path is more likely to be followed. In this fixed configuration we can then think of the system in dynamic terms, and consider the range of initial conditions (including velocity, perhaps caused by an impact force) that might push the system from a point on path α to a point on path ϕ .

Governing equations. In this analysis a slender buckled beam with thickness d , width b and length L is considered. A Cartesian coordinate system $o-xyz$ is established on the mid-plane of the beam in which o is the origin, x, y the directions along the length and width directions and z the downward direction normal to the mid-plane. Based on Euler-Bernoulli beam theory [1, 22], the displacement field (u_1, u_3) of the beam along (x, z) directions can be written as

$$\begin{aligned} u_1(x, z, t) &= u(x, t) - z \frac{\partial w(x, t)}{\partial x}, \\ u_3(x, z, t) &= w(x, t), \end{aligned} \quad (3.1)$$

where $u(x, t)$ and $w(x, t)$ are the axial and transverse displacements of an arbitrary point on the mid-plane of the beam. Considering the von Kármán-type geometrical nonlinearity, the total axial strain can be obtained as

$$\varepsilon_x^* = \frac{\partial u}{\partial x} - z \frac{\partial^2 w}{\partial x^2} + \frac{1}{2} \left(\frac{\partial w}{\partial x} \right)^2. \quad (3.2)$$

For a moderately buckled-beam, we need to consider the initial strain ε_0 produced by initial deflection w_0 which is

$$\varepsilon_0 = -z \frac{\partial^2 w_0}{\partial x^2} + \frac{1}{2} \left(\frac{\partial w_0}{\partial x} \right)^2. \quad (3.3)$$

Then the change in strain ε_x can be expressed as

$$\varepsilon_x = \varepsilon_x^* - \varepsilon_0 = \frac{\partial u}{\partial x} - z \left(\frac{\partial^2 w}{\partial x^2} - \frac{\partial^2 w_0}{\partial x^2} \right) + \frac{1}{2} \left[\left(\frac{\partial w}{\partial x} \right)^2 - \left(\frac{\partial w_0}{\partial x} \right)^2 \right]. \quad (3.4)$$

Here we just consider homogeneous isotropic materials with Young's modulus E , and allow for the possibility of thermal loading. The axial stress σ_x can be obtained according to the one dimensional constitutive equation, as

$$\sigma_x = E\varepsilon_x - E\alpha_x \Delta T, \quad (3.5)$$

where α_x is the thermal expansion coefficient and ΔT is the temperature increment from the reference temperature at which the beam is in a stress free state. Thermal loading is introduced as a convenient way of controlling the initial equilibrium shapes (and hence the potential energy landscape) via axial loading.

The strain energy $\mathcal{V}(x, z, t)$ is

$$\mathcal{V}(x, z, t) = \frac{b}{2} \int_0^L \int_{-\frac{d}{2}}^{\frac{d}{2}} \sigma_x \varepsilon_x dz dx. \quad (3.6)$$

Ignoring the axial inertia term, the kinetic energy $\mathcal{T}(x, z, t)$ of the buckled beam is

$$\mathcal{T}(x, z, t) = \frac{b}{2} \int_0^L \int_{-\frac{d}{2}}^{\frac{d}{2}} \rho \dot{w}^2 dz dx, \quad (3.7)$$

where ρ is the mass density. In addition, the dot over the quantity is the derivative with respect to time.

The governing equations can be obtained by the Lagrange-d'Alembert principle [23] which requires that

$$\delta \int_{t_0}^t [\mathcal{T}(x, z, t) - \mathcal{V}(x, z, t)] dt + \int_{t_0}^t \delta W_{nc} dt = 0, \quad (3.8)$$

where δ denotes the variational operator, t_0 and t the initial and current time. δW_{nc} is the variation of the virtual work done by non-conservative force (damping) which is expressed as

$$\delta W_{nc} = -c_d \dot{w} \delta w, \quad (3.9)$$

where c_d is the coefficient of (linear viscous) damping. In subsequent analysis, and related to typical practical situations, the damping will be small.

After some manipulation, the governing equations in terms of axial force N_x and bending moment M_x can be obtained as [22]

$$\begin{aligned} \frac{\partial N_x}{\partial x} &= 0, \\ \frac{\partial^2 M_x}{\partial x^2} + N_x \frac{\partial^2 w}{\partial x^2} &= \rho A \ddot{w} + c_d \dot{w}, \end{aligned} \quad (3.10)$$

where N_x and M_x are defined as

$$(N_x, M_x) = b \int_{-\frac{d}{2}}^{\frac{d}{2}} \sigma_x(1, z) dz. \quad (3.11)$$

By using (3.1), (3.4) and (3.5), the force N_x and moment M_x in (3.11) can be rewritten as

$$\begin{aligned} N_x &= EA \left[\frac{\partial u}{\partial x} + \frac{1}{2} \left(\left(\frac{\partial w}{\partial x} \right)^2 - \left(\frac{\partial w_0}{\partial x} \right)^2 \right) \right] - N_T, \\ M_x &= -EI \left(\frac{\partial^2 w}{\partial x^2} - \frac{\partial^2 w_0}{\partial x^2} \right), \end{aligned} \quad (3.12)$$

where A and I denote the cross-sectional area and moment of inertia; $N_T = EA\alpha_x \Delta T$, the axial thermal loads. Thus, EA and EI are the axial stiffness and bending stiffness, respectively.

Here we just consider a clamped-clamped beam with in-plane immovable ends. The boundary conditions are

$$x = 0, L : u = w = \frac{\partial w}{\partial x} = 0. \quad (3.13)$$

Note that from the first equation in (3.10), it is clear that the axial force N_x is constant along the axial direction. In this case, integrating the axial force along the x axis and using the boundary conditions $u(0, t) = u(L, t) = 0$, one can obtain

$$N_x = \frac{EA}{2L} \int_0^L \left[\left(\frac{\partial w}{\partial x} \right)^2 - \left(\frac{\partial w_0}{\partial x} \right)^2 \right] dx - N_T. \quad (3.14)$$

Using M_x in (3.12) and N_x in (3.14), the second equation in (3.10) can be described in terms of the transverse displacement w as [1]

$$\rho A \ddot{w} + c_d \dot{w} + EI \left(\frac{\partial^4 w}{\partial x^4} - \frac{\partial^4 w_0}{\partial x^4} \right) + \left[N_T - \frac{EA}{2L} \int_0^L \left(\left(\frac{\partial w}{\partial x} \right)^2 - \left(\frac{\partial w_0}{\partial x} \right)^2 \right) dx \right] \frac{\partial^2 w}{\partial x^2} = 0, \quad (3.15)$$

where w and w_0 are the current deflection and initial geometrical imperfection, respectively; ρ is the mass density; c_d is the damping coefficient; A and I are the area and the moment of inertia of the cross-section, respectively; E is the Young's modulus. Given the immovable ends it is natural to consider the effective externally applied axial force to be replaced by a thermal loading term: this is the primary destabilizing nonlinearity in the system.

As mentioned earlier, clamped-clamped boundary conditions are considered. Thus we make use of the vibration mode shapes

$$\begin{aligned} \phi_n &= \psi_n \left[\sinh \frac{\kappa_n x}{L} - \sin \frac{\kappa_n x}{L} + \delta_n \left(\cosh \frac{\kappa_n x}{L} - \cos \frac{\kappa_n x}{L} \right) \right], \\ \delta_n &= \frac{\sinh \kappa_n - \sin \kappa_n}{\cos \kappa_n - \cosh \kappa_n}, \\ \cos \kappa_n \cosh \kappa_n &= 1, \\ \psi_1 &= -0.6186, \quad \psi_2 = -0.6631, \end{aligned} \quad (3.16)$$

and describe the deflected shape in terms of a two-degree-of-freedom approximation

$$\begin{aligned} w(x, t) &= X(t)\phi_1(x) + Y(t)\phi_2(x), \\ w_0(x) &= \gamma_1\phi_1(x) + \gamma_2\phi_2(x), \end{aligned} \quad (3.17)$$

where the initial imperfections are given by w_0 . To obtain the ordinary differential equations, we multiply the equation of motion in (3.15) by ϕ_i and integrate over the length of the beam.

Considering the clamped-clamped boundary conditions, applying integration by parts yields

$$\begin{aligned} & \rho A \int_0^L \phi_i \ddot{w} dx + c_d \int_0^L \phi_i \dot{w} dx + EI \int_0^L \frac{\partial^2 \phi_i}{\partial x^2} \left(\frac{\partial^2 w}{\partial x^2} - \frac{\partial^2 w_0}{\partial x^2} \right) dx \\ & - \left[N_T - \frac{EA}{2L} \int_0^L \left(\left(\frac{\partial w}{\partial x} \right)^2 - \left(\frac{\partial w_0}{\partial x} \right)^2 \right) dx \right] \int_0^L \frac{\partial \phi_i}{\partial x} \frac{\partial w}{\partial x} dx = 0. \end{aligned} \quad (3.18)$$

Substituting the approximations for w and w_0 in (3.17) with specific mode shapes ϕ_i in (3.16) and noticing the mode shapes are mutually orthogonal, the nonlinear equations can be obtained as

$$\begin{aligned} M_1 \ddot{X} + C_1 \dot{X} + K_1 (X - \gamma_1) - N_T G_1 X - \frac{EA}{2L} G_1^2 (\gamma_1^2 X - X^3) - \frac{EA}{2L} G_1 G_2 (\gamma_2^2 X - XY^2) &= 0, \\ M_2 \ddot{Y} + C_2 \dot{Y} + K_2 (Y - \gamma_2) - N_T G_2 Y - \frac{EA}{2L} G_2^2 (\gamma_2^2 Y - Y^3) - \frac{EA}{2L} G_1 G_2 (\gamma_1^2 Y - X^2 Y) &= 0, \end{aligned} \quad (3.19)$$

where

$$(M_i, C_i) = (\rho A, c_d) \int_0^L \phi_i^2 dx, \quad K_i = EI \int_0^L \left(\frac{\partial^2 \phi_i}{\partial x^2} \right)^2 dx, \quad G_i = \int_0^L \left(\frac{\partial \phi_i}{\partial x} \right)^2 dx. \quad (3.20)$$

The kinetic energy and potential energy, respectively, can be represented as

$$\begin{aligned} \mathcal{T}(\dot{X}, \dot{Y}) &= \frac{1}{2} M_1 \dot{X}^2 + \frac{1}{2} M_2 \dot{Y}^2, \\ \mathcal{V}(X, Y) &= -K_1 \gamma_1 X - K_2 \gamma_2 Y + \frac{1}{2} K_1 X^2 + \frac{1}{2} K_2 Y^2 - \frac{1}{2} N_T (G_1 X^2 + G_2 Y^2) \\ &\quad - \frac{EA}{2L} G_1^2 \left(\frac{1}{2} \gamma_1^2 X^2 - \frac{1}{4} X^4 \right) - \frac{EA}{2L} G_2^2 \left(\frac{1}{2} \gamma_2^2 Y^2 - \frac{1}{4} Y^4 \right) \\ &\quad - \frac{EA}{2L} \frac{G_1 G_2}{2} (\gamma_2^2 X^2 + \gamma_1^2 Y^2 - X^2 Y^2). \end{aligned} \quad (3.21)$$

For physically reasonable coefficients we have a number of equilibrium possibilities. For small values of N_T we have an essentially linear system, dominated by the trivial (straight) equilibrium configuration, and thus an isolated center (minimum of the potential energy). This relates back to the situation in Figure 3.1 for a small value of P . But for larger values of P , for example a little below P_c , the system typically possesses a number of equilibria, some of which are stable and some of which are not. Some typical forms are shown in Figure 3.2(a) in which the five dots are the equilibrium points where W_1 and W_2 are within the two stable wells; S_1 and S_2 two unstable saddle points; H the unstable hilltop. Thus, we might have the system sitting (in equilibrium) at point W_1 . If it is then subject to a disturbance *with the right size and direction* (in the dynamical context), we might expect the system to transition to the remote equilibrium at W_2 . This might

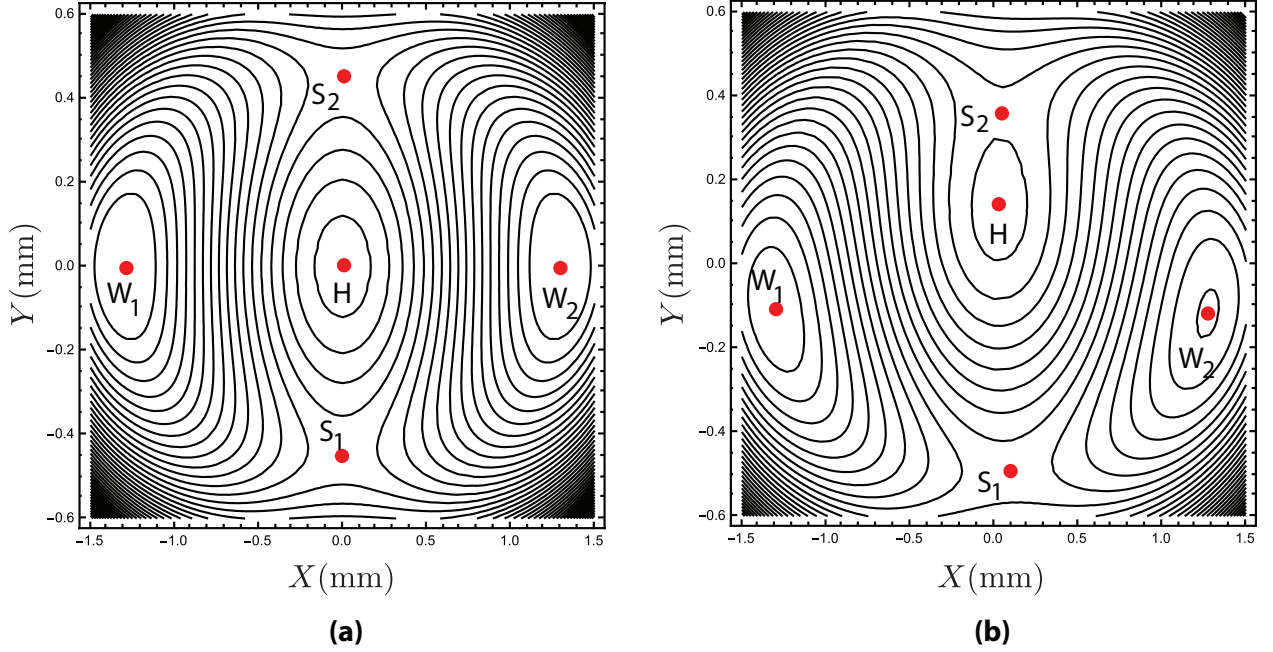


Figure 3.2: Contours of potential energy: (a) the symmetric system, $\gamma_1 = \gamma_2 = 0$, (b) with small initial imperfections in both modes, i.e., γ_1 and γ_2 are nonzero.

occur when the system is subject to a large impact force, for example [21]. It is anticipated (and will later be shown) that the typically easiest transition will be associated with (an asymmetric) passage close to S_1 or S_2 , and generally avoiding H . In Figure 3.2(b) is shown the same system but now with a small geometric imperfection in both modes (i.e., $\gamma_1 \neq 0$ and $\gamma_2 \neq 0$). In this case the symmetry of the system is broken, and given the relative energy associated with the saddle points it is anticipated (and will also be shown later) that optimal escape will tend to occur via S_1 .

Note that eqs. (3.19) can also be obtained from Lagrange's equations,

$$\frac{d}{dt} \left(\frac{\partial \mathcal{L}}{\partial \dot{q}_i} \right) - \frac{\partial \mathcal{L}}{\partial q_i} = -C_i \dot{q}_i \quad i = 1, 2, \quad (3.22)$$

when $q_1 = X$ and $q_2 = Y$, and the Lagrangian is

$$\mathcal{L}(X, Y, \dot{X}, \dot{Y}) = \mathcal{T}(\dot{X}, \dot{Y}) - \mathcal{V}(X, Y). \quad (3.23)$$

To transform this to a Hamiltonian system, one defines the generalized momenta,

$$p_i = \frac{\partial \mathcal{L}}{\partial \dot{q}_i} = M_i \dot{q}_i, \quad (3.24)$$

so $p_X = M_1 \dot{X}$ and $p_Y = M_2 \dot{Y}$, in which case, the kinetic energy is

$$\mathcal{T}(X, Y, p_X, p_Y) = \frac{1}{2M_1} p_X^2 + \frac{1}{2M_2} p_Y^2, \quad (3.25)$$

and the Hamiltonian is

$$\mathcal{H}(X, Y, p_X, p_Y) = \mathcal{T} + \mathcal{V}, \quad (3.26)$$

and Hamilton's equations (with damping) [24] are

$$\begin{aligned} \dot{X} &= \frac{\partial \mathcal{H}}{\partial p_X} = \frac{p_X}{M_1}, & \dot{Y} &= \frac{\partial \mathcal{H}}{\partial p_Y} = \frac{p_Y}{M_2}, \\ \dot{p}_X &= -\frac{\partial \mathcal{H}}{\partial X} - C_{HPX} = -\frac{\partial \mathcal{V}}{\partial X} - C_{HPX}, \\ \dot{p}_Y &= -\frac{\partial \mathcal{H}}{\partial Y} - C_{HPY} = -\frac{\partial \mathcal{V}}{\partial Y} - C_{HPY}, \end{aligned} \quad (3.27)$$

where

$$\begin{aligned} \frac{\partial \mathcal{V}}{\partial X} &= K_1 (X - \gamma_1) - N_T G_1 X - \frac{EA}{2L} G_1^2 (\gamma_1^2 X - X^3) - \frac{EA}{2L} G_1 G_2 (\gamma_2^2 X - XY^2), \\ \frac{\partial \mathcal{V}}{\partial Y} &= K_2 (Y - \gamma_2) - N_T G_2 Y - \frac{EA}{2L} G_2^2 (\gamma_2^2 Y - Y^3) - \frac{EA}{2L} G_1 G_2 (\gamma_1^2 Y - X^2 Y), \end{aligned} \quad (3.28)$$

and $C_H = C_1/M_1 = C_2/M_2$ is the damping coefficient in the Hamiltonian system which can be easily found by comparing (3.19) and (3.27), and using the relations of M_i and C_i in (3.20).

Linearization around S_1 . We assume the lower saddle point S_1 has the smaller potential energy compared to S_2 , thus the energy of S_1 is the critical energy for snap-through, and we initially focus attention on the dynamic behavior around the region of S_1 . The linearized equations of (3.27) about S_1 with position (X_e, Y_e) can be written as

$$\begin{aligned} \dot{x} &= \frac{p_x}{M_1}, & \dot{y} &= \frac{p_y}{M_2}, \\ \dot{p}_x &= A_{31}x + A_{32}y - C_{HPx}, \\ \dot{p}_y &= A_{42}x + A_{41}y - C_{HPy}, \end{aligned} \quad (3.29)$$

where $(x, y, p_x, p_y) = (X, Y, p_X, p_Y) - (X_e, Y_e, 0, 0)$ and

$$\begin{aligned} A_{31} &= -K_1 + N_T G_1 + \frac{EAG_1^2(\gamma_1^2 - 3X_e^2)}{2L} + \frac{EAG_1 G_2(\gamma_2^2 - Y_e^2)}{2L}, \\ A_{32} &= -\frac{EAG_1 G_2 X_e Y_e}{L}, \\ A_{42} &= -K_2 + N_T G_2 + \frac{EAG_2^2(\gamma_2^2 - 3Y_e^2)}{2L} + \frac{EAG_1 G_2(\gamma_1^2 - X_e^2)}{2L}. \end{aligned} \quad (3.30)$$

If we replace the position of S_1 by the position of W_1 , we can still use the linearized equations in (3.29) to obtain the natural frequencies of the shallow arch near W_1 as

$$\omega_{1,2}^{(d)} = \omega_{1,2}^{(c)} \sqrt{1 - \xi_{1,2}^2}, \quad (3.31)$$

where $\omega_{1,2}^{(c)}$ are the first two natural frequencies for the conservative system and $\xi_{1,2}$ are the viscous damping factors with the forms

$$\omega_{1,2}^{(c)} = \frac{(b_\omega \mp \sqrt{b_\omega^2 - 4c_\omega})}{2}, \quad \xi_{1,2} = \frac{C_H}{2\omega_{1,2}^{(c)}}, \quad (3.32)$$

and

$$b_\omega = -\frac{A_{31}}{M_1} - \frac{A_{42}}{M_2}, \quad c_\omega = \frac{A_{31}A_{42} - A_{32}^2}{M_1 M_2}.$$

Non-dimensional equations of motion In order to reduce the parameters, some non-dimensional quantities are introduced,

$$\begin{aligned} (L_x, L_y) &= L \left(1, \sqrt{\frac{M_1}{M_2}} \right), \omega_0 = \frac{\sqrt{-A_{32}}}{(M_1 M_2)^{\frac{1}{4}}}, \tau = \omega_0 t, (\bar{q}_1, \bar{q}_2) = \left(\frac{x}{L_x}, \frac{y}{L_y} \right), \\ (\bar{p}_1, \bar{p}_2) &= \frac{1}{\omega_0} \left(\frac{p_x}{L_x M_1}, \frac{p_y}{L_y M_2} \right), (c_x, c_y) = \frac{1}{\omega_0^2} \left(\frac{A_{31}}{M_1}, \frac{A_{42}}{M_2} \right), c_1 = \frac{C_H}{\omega_0}. \end{aligned} \quad (3.33)$$

Using the non-dimensional parameters in (3.33), the non-dimensional linearized equations are written as

$$\begin{aligned} \dot{\bar{q}}_1 &= \bar{p}_1, \quad \dot{\bar{q}}_2 = \bar{p}_2, \\ \dot{\bar{p}}_1 &= c_x \bar{q}_1 - \bar{q}_2 - c_1 \bar{p}_1, \\ \dot{\bar{p}}_2 &= -\bar{q}_1 + c_y \bar{q}_2 - c_1 \bar{p}_2. \end{aligned} \quad (3.34)$$

Written in matrix form, with column vector $\bar{z} = (\bar{q}_1, \bar{q}_2, \bar{p}_1, \bar{p}_2)$, we have

$$\dot{\bar{z}} = A\bar{z} + D\bar{z},$$

where

$$A = \begin{pmatrix} 0 & 0 & 1 & 0 \\ 0 & 0 & 0 & 1 \\ c_x & -1 & 0 & 0 \\ -1 & c_y & 0 & 0 \end{pmatrix}, \quad D = \begin{pmatrix} 0 & 0 & 0 & 0 \\ 0 & 0 & 0 & 0 \\ 0 & 0 & -c_1 & 0 \\ 0 & 0 & 0 & -c_1 \end{pmatrix} \quad (3.35)$$

are the Hamiltonian part and damping part of the linear equations, respectively.

Linearized dynamics around S_1 Chapter 2 has discussed the linearized dynamics around the index-1 saddle for an idealized ball rolling on both stationary and rotating surfaces. The linearized dynamics about the local behavior around the S_1 in both conservative and dissipative systems of a shallow arch is topologically the same as the rolling ball on a stationary surface, except the flow in position space of current problem is slightly tilted. The solution derivations of the linearized dynamics can be obtained following the rolling ball on a stationary surface in Chapter 2. For simplicity, the derivation and analysis are ignored for current problem. Readers are also referred to [25] for more details. Since in the algorithms of computing the transition tube in the full nonlinear system will use the solutions of the linearized system, here we give the symplectic matrix

$$C = \begin{pmatrix} \frac{1}{s_1} & \frac{1}{s_2} & -\frac{1}{s_1} & 0 \\ \frac{c_x - \lambda^2}{s_1} & \frac{\omega_p^2 + c_x}{s_2} & \frac{\lambda^2 - c_x}{s_1} & 0 \\ \frac{\lambda}{s_1} & 0 & \frac{\lambda}{s_1} & \frac{\omega_p}{s_2} \\ \frac{c_x \lambda - \lambda^3}{s_1} & 0 & \frac{c_x \lambda - \lambda^3}{s_1} & \frac{c_x \omega_p + \omega_p^3}{s_2} \end{pmatrix}. \quad (3.36)$$

where $s_1 = \sqrt{d_\lambda}$ and $s_2 = \sqrt{d_{\omega_p}}$, and,

$$\begin{aligned} d_\lambda &= \lambda[4 - 2(c_x - c_y)(\lambda^2 - c_x)], & d_{\omega_p} &= \frac{\omega_p}{2}[4 + 2(c_x - c_y)(\omega_p^2 + c_x)], \\ \lambda &= \sqrt{\left(c_x + c_y + \sqrt{(c_x - c_y)^2 + 4}\right)}/2, & \omega_p &= \sqrt{-\left(c_x + c_y - \sqrt{(c_x - c_y)^2 + 4}\right)}/2. \end{aligned} \quad (3.37)$$

The generalized eigenvectors for the conservative systems are given by

$$\begin{aligned} u_{\omega_p} &= (1, c_x + \omega_p^2, 0, 0), & v_{\omega_p} &= (0, 0, \omega_p, c_x \omega_p + \omega_p^3), \\ u_{+\lambda} &= (1, c_x - \lambda^2, \lambda, c_x \lambda - \lambda^3), & u_{-\lambda} &= -(1, c_x - \lambda^2, -\lambda, \lambda^3 - c_x \lambda). \end{aligned} \quad (3.38)$$

3.3 Transition Tubes

In this section, we go step by step through the numerical construction of the boundary between transit and non-transit orbits in the nonlinear system (3.27). We combine the geometric insight of linearized system with numerical methods to demonstrate the existence of ‘transition tubes’ for both the conservative and damped systems. Particular attention is paid to the modification of phase space transport as damping is increased, as this has not been considered previously.

Tube dynamics The dynamic snap-through of the shallow arch can be understood as trajectories escaping from a potential well with energy above a critical level: the energy of the saddle point S_1 . However, even if the energy of the system is higher than critical, the snap-through may not occur. The dynamical boundary between snap-through and non-snap-through behavior can be systematically understood by **tube dynamics**. Tube dynamics [9, 10, 11, 12, 13, 14, 15, 16, 17, 18, 19] supplies a large-scale picture of transport; transport between the largest features of the phase space—the potential wells. In the conservative system, the stable and unstable manifolds with a $S^1 \times \mathbb{R}$ geometry act as **tubes** emanating from the periodic orbits. While found above for the linearized system near S_1 , these structures persist in the full nonlinear system. The manifold tubes (usually called **transition tubes** in tube dynamics), formed by pieces of asymptotic orbits, separate two distinct types of orbits: transit orbits and non-transit orbits, corresponding to snap-through and non-snap-through in the present problem. The transit orbits, passing from one region to another through the bottleneck, are those inside the transition tubes. The non-transit orbits, bouncing back to their region of origin, are those outside the transition tubes. Thus, the transition tubes can mediate the global transport of states between snap-through and non-snap-through. In the dissipative system, similar transition tubes also exist. Even in systems where stochastic effects are present, the influence of these structures remains [8].

3.3.1 Algorithm for computing transition tubes

For the conservative system, Ref. [19] gives a general numerical method to obtain the transition tubes. The key steps are (1) to find the periodic orbits restricted to a specified energy using differential correction and numerical continuation based on the initial conditions obtained from the linearized system at first, then (2) to compute the manifold tubes of the periodic orbits in the nonlinear system (i.e., ‘globalizing’ the manifolds), and finally (3) to obtain the intersection of the Poincaré surface of section and global manifolds. See details in Ref. [19]. The method is effective in the conservative system, but not applicable to the dissipative system, since due to loss

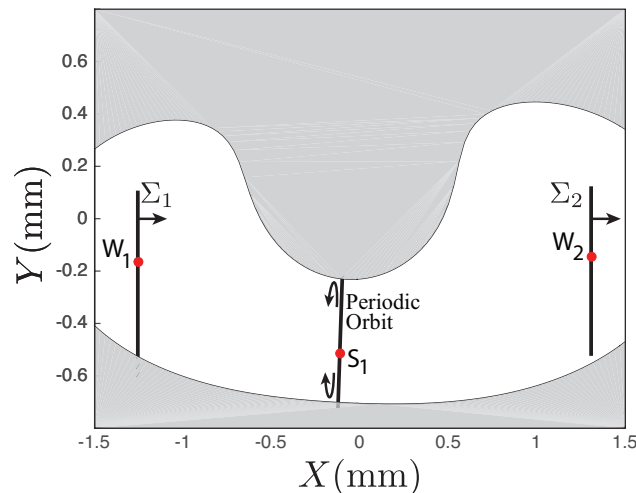


Figure 3.3: For a representative energy above the saddle point S_1 , we show the unstable periodic orbit in the neck region around S_1 . It projects to a single line going between the upper and lower energy boundary curves, and arrows are shown for convenience. We show the Poincaré sections Σ_1 and Σ_2 which are defined by X values equal to that of the two stable equilibria in the center of the left and right side wells, W_1 and W_2 , respectively. The arrows on the vertical lines indicate that these Poincaré sections are also defined by positive X momentum.

of conservation of energy, no periodic orbit exists. Thus, we provide another method as follows.

Step 1: Select an appropriate energy. We first need to set the energy to an appropriate value such that the snap-through behavior exists. Once the energy is given, it remains constant in the conservative system. In our example, the critical energy for snap-through is the energy of S_1 . Thus, we can choose an energy which is between that of S_1 and S_2 . In this case, all transit orbits can just escape from W_1 to W_2 through S_1 . Notice that the potential energy determines the width of the bottleneck and the size of the transition tubes which hence determines the relative fraction of transit orbits in the phase space. A representative energy case is shown in Figure 3.3, which also establishes our location for Poincaré sections Σ_1 and Σ_2 which are at $X = \text{constant}$ lines passing through W_1 and W_2 respectively, and with $p_X > 0$.

Step 2: Compute the approximate transition tube and its intersection on a Poincaré section. We have analyzed the flow of linearized system in both phase space and position space which classifies orbits into four classes in Chapter 2. It shows that in the conservative system the stable manifolds correspond to the boundary between transit orbits and non-transit orbits. Thus, we can choose this manifold as the starting point. We start by considering the approximation of transition tubes for the conservative system.

Determine the initial condition. The stable manifold divides the transit orbits and non-transit orbits for all trajectories headed toward a bottleneck. Thus, we can use the stable manifold to obtain the initial condition. Considering the general solutions (2.34) of the linearized equations, we can let $p_1^0 = c$, $q_1^0 = 0$, $q_2^0 = A_q$ and $p_2^0 = A_p$. Notice that

$$A_q^2 + A_p^2 = 2h/\omega_p, \quad (3.39)$$

which forms a circle in the center projection, so in the next computational procedure we should pick up N points on the circle with a constant arc length interval. Each A_q and A_p determined by these sampling points along with $p_1^0 = c$ and $q_1^0 = 0$ can be used as initial conditions. When first transformed back to the position space and then transformed to dimensional quantities, this yields an initial condition

$$\begin{pmatrix} X_0 \\ Y_0 \\ p_{X0} \\ p_{Y0} \end{pmatrix} = \begin{pmatrix} x_e \\ y_e \\ 0 \\ 0 \end{pmatrix} + \begin{pmatrix} L_x \\ L_y \\ \omega_0 L_x M_1 \\ \omega_0 L_y M_2 \end{pmatrix}^T C \begin{pmatrix} c \\ 0 \\ A_q \\ A_p \end{pmatrix}. \quad (3.40)$$

Integrate backward and obtain Poincaré section. Using the N initial conditions (3.40) yielded by varying A_q and A_p governed by (3.39) and integrating the nonlinear equations of motions in (3.27) in the backward direction, we obtain a tube, formed by the N trajectories, which is a linear approximation for the transition tube. Choosing the Poincaré surface-of-section Σ_1 is shown in Figure 3.3, corresponding to $X = X_{W_1}$ and $p_X > 0$.

Step 3: Compute the real transition tube by the bisection method. We have obtained a Poincaré section which is the intersection of the approximate transition tube and the surface Σ_1 . First pick a point (noted as p_i) which is almost the center of the closed curve. The line from p_i to each of the N points on the Poincaré map will form a ray. The point p_i inside the curve in general is a transit orbit. Then choose another point on each radius which is a non-transit orbit, noted as p_o . With the approach described above, we can use the bisection method to obtain the boundary of the transition tube on a specific radius (cf. [26]). Picking the midpoint (marked by p_m) as the initial condition and carrying out forward integration for the nonlinear equation of motion in (3.27), we can estimate if this trajectory can transit or not. If it is a transit orbit, note it as p_i , otherwise note it as p_o . Continuing this procedure again until the distance between p_i and p_o reaches a specified tolerance, the boundary of the tube on this ray is estimated. Thus, the real transition tube for the conservative system can be obtained if the same procedure is carried out for all angles. A related method is described in [27], adapting an approach of [28].

For the dissipative system, the size of the transition tubes for a given energy on Σ_1 will shrink. Using

the bisection method and following the same procedure as for conservative system, the transition tube for the dissipative system will be obtained.

3.3.2 Numerical results and discussion

To visualize the tube dynamics for the arch, several examples will be given. According to the steps mentioned above, we can obtain the transition tubes for both the conservative system and dissipative system. For all results, the geometries of the arch are selected as $b = 12.7$ mm $d = 0.787$ mm, $L = 228.6$ mm. The Young's modulus and the mass density are $E = 153.4$ GPa and $\rho = 7567$ kg m⁻³. The selected thermal load corresponds to 184.1 N, while the initial imperfections are $\gamma_1 = 0.082$ mm and $\gamma_2 = -0.077$ mm. These values match the parameters given in the experimental study [1]. For all the numerical results given in this section, the initial energy of the system is set at 3.68×10^{-4} J - above the energy of saddle point S_1 , so that the equilibrium point W_1 is inside the configuration space projection. This choice of initial energy will make it possible to compare the numerical results with the experimental results which are planned for future work.

Transition tubes for conservative system For conservative system, the Hamiltonian is a constant of motion. In Figure 3.4, we show the configuration space projection of the transition tube and the Poincaré sections on Σ_1 and Σ_2 which are closed curves. In Figure 3.4 are shown all the trajectories which form the transition tube boundary starting from Σ_1 and ending up at Σ_2 , flowing from left to right through the neck region.

Due to the the conservation of energy, the size of the transition tube is constant during evolution, which corresponds to the cross-sectional area of the transition tube. It should be noted that the areas of the tube Poincaré sections on Σ_1 and Σ_2 in Figure 3.4 are equal, due to the integral invariants of Poincaré for a system obeying Hamilton's canonical equations (with no damping). Moreover, note that the size of the transition tube, the boundary of the transit orbits, is determined by the energy. For a lower energy, the size of the transition tube is smaller or vice versa. In other words, the area of the Poincaré sections on Σ_1 and Σ_2 is determined by the energy. In fact, the cross-sectional area of the transition tube is proportional to the energy above the saddle point S_1 [29]. As mentioned before, the transition tube separates the transit orbits and non-transit orbits, which correspond to snap-through and non-snap-through. The orbit inside the transition tube can transit, while the orbit outside the transition tube cannot transit.

Transition tubes for the dissipative system Unlike the conservation of energy in the conservative system, the energy in the dissipative system is decreasing with time. Figure 3.5 shows

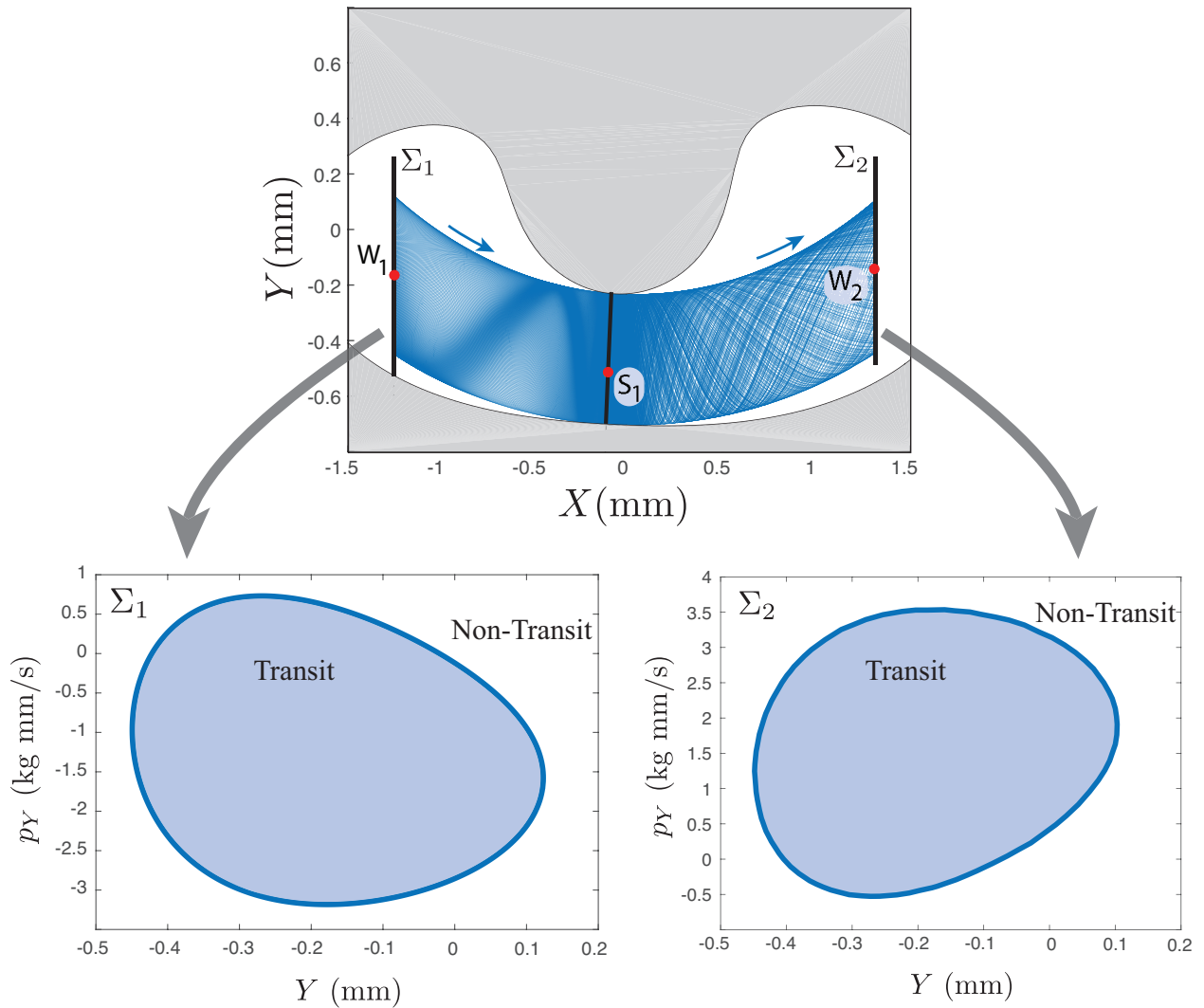


Figure 3.4: A transition tube from the left well to the right well, obtained using the method described in the text. The upper figure shows the configuration space projection. The lower left shows the tube boundary (closed curve) on Poincaré section Σ_1 , which separates transit and non-transit trajectories. The lower right shows the corresponding tube boundary (closed curve) on Poincaré section Σ_2 .

the configuration space projection of the transition tube and the Poincaré sections on Σ_1 and Σ_2 . In Figure 3.5 the transition tube starts from Σ_1 and ends up with Σ_2 flowing from left to right through the neck region, as shown previously for the conservative system. From the figure, we can observe the distinct reduction in the size of the transition tube, especially near the neck region. To show this, the scale of the Poincaré section projections is the same as in Figure 3.4. During the evolution, the energy of the system is decreasing due to damping. The trajectories spend a great amount of time crossing the neck region, resulting in the total energy decreasing dramatically (and

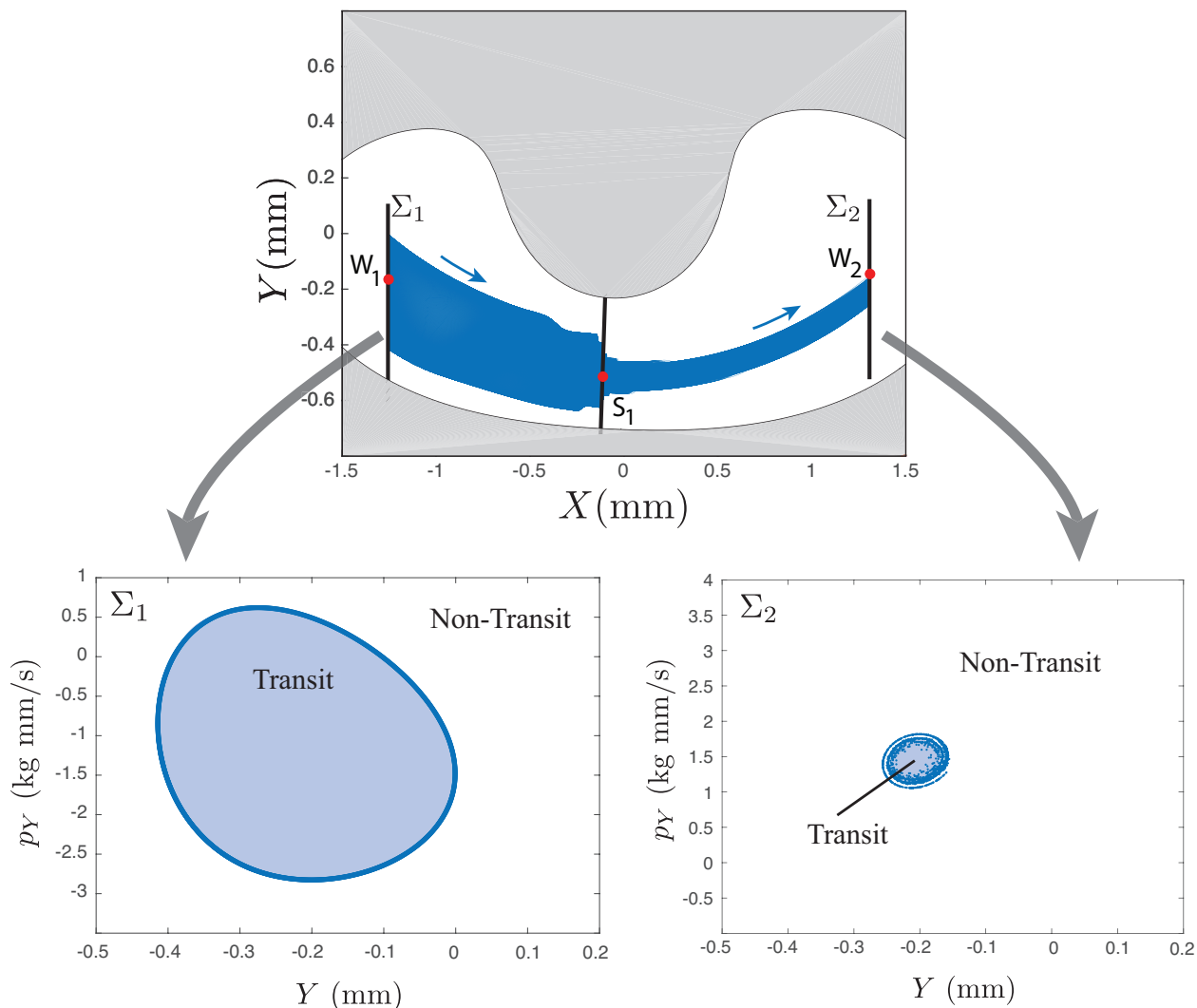


Figure 3.5: A transition tube from the left well to the right well, obtained using the method described in the text, for the case of damping. The upper figure shows the configuration space projection. The lower left shows the tube boundary (closed curve) on Poincaré section Σ_1 which separates transit and non-transit trajectories for initial conditions all with a given fixed initial energy. The lower right shows the corresponding image under the flow on Poincaré section Σ_2 . Due to the damping, and a range of times spent in the neck region, spiraling is visible in this 2D projection since trajectories which spend longer in the neck will be at lower total energies. Compare with Figure 3.4.

influencing the size of the transition tubes to the right of the neck region). Thus, the transition tube is spiraling in the neck region so that Poincaré Σ_2 is not a closed curve, nor are the trajectories at a constant energy. The Σ_2 plot is merely a projection onto the (Y, p_Y) -plane to give an idea of the actual co-dimension 1 tube boundary in the 4-dimensional phase space. Note the clear differences

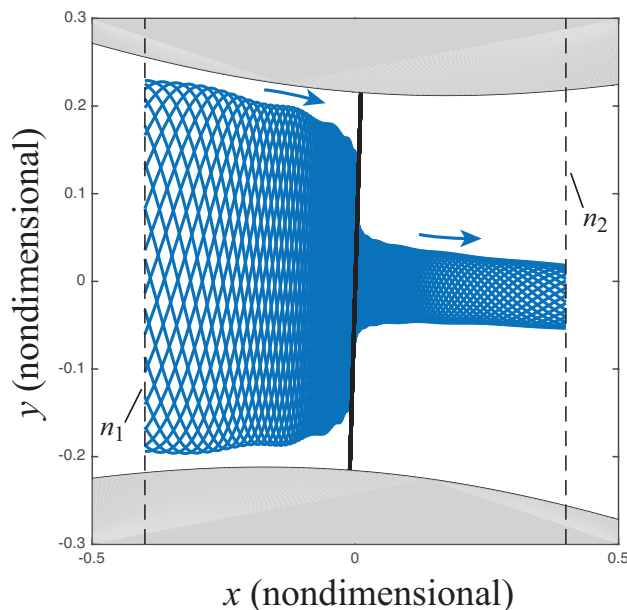


Figure 3.6: A transition tube from the left side boundary (n_1) to the right side boundary (n_2) of the equilibrium region around saddle point S_1 , obtained for the linear damped system. Notice that the shrinking of the tube is observed as in the nonlinear system, Figure 3.5, here seen in terms of the width of the projected strip onto configuration space.

between Figure 3.4 and Figure 3.5. The dramatic shrinking of tubes near the neck region is due almost entirely to the linearized dynamics near the saddle point. To confirm this, we present the linear transition tube obtained by the analytical solutions for the linearized dissipative system in Figure 3.6. See the analytical solutions for the linearized dissipative system in [25].

Effect of damping on the transition tubes In order to further quantify how damping affects the size of transition tubes, we present the tube Poincaré section on Σ_1 with different damping in Figure 3.7. In Figure 3.7(a), we can see the canonical area ($\int_{\mathcal{A}} p_Y dY$) decreases with increasing damping. Thus, the proportion of transition trajectories will be fewer if the damping increases. Note that when the damping changes, different transition tubes almost share the same center which corresponds to the fastest trajectories. Figure 3.7(b) shows the relation between the damping and the projected canonical area ($\int_{\mathcal{A}} p_Y dY$), which is related to the relative number of transit compared to non-transit orbits. It shows that an increase in damping decreases the projected area. When the damping is small, the relation between the damping and the area is linear, while when the damping is large, the relation becomes slightly nonlinear. Note that generally in mechanical/structural experiments the non-dimensional damping factor ξ_d is less than

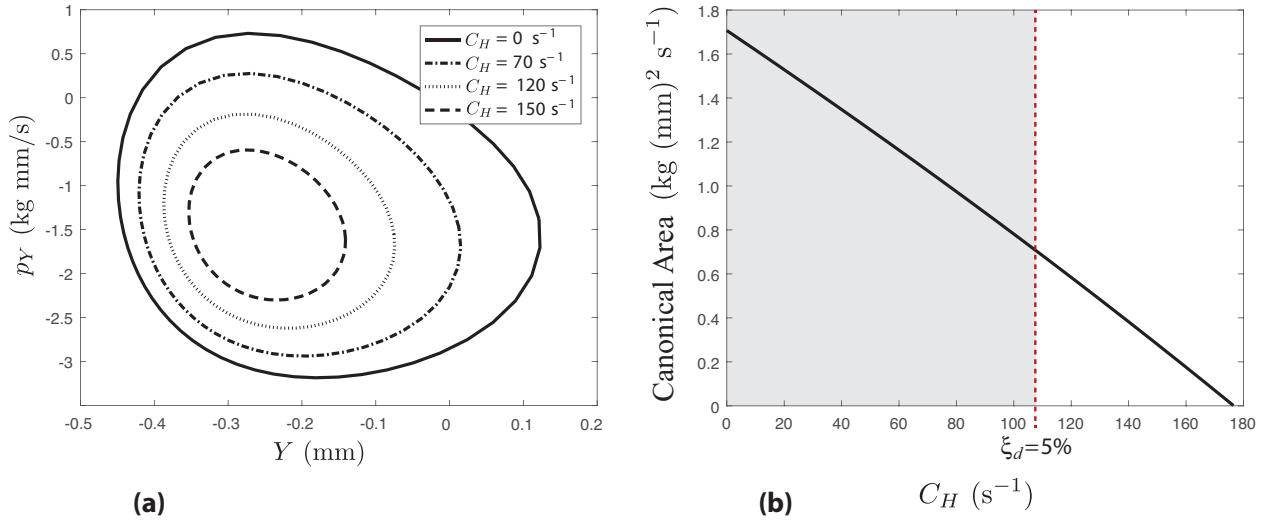


Figure 3.7: The effect of the damping coefficient C_H on the area of the transition tube on Poincaré section Σ_1 is shown. For a fixed initial energy above the saddle, the projection on the canonical plane (Y, p_Y) is shown in (a) and the area is plotted in (b). In (b), the shaded region indicates the experimentally observed range of damping coefficients, which correspond to non-dimensional damping factor ξ_d less than 5%.

5% which corresponds to a damping coefficient C_H less than 107.3 s^{-1} (see the shaded region in Figure 3.7(b)). Furthermore, note that for the initial energy depicted in Figure 3.7, there are no transit orbits starting on Σ_1 for C_H greater than about 185 s^{-1} .

Demonstration of trajectories inside and outside the transition tube To illustrate the effectiveness of the transition tubes, we choose three points on Σ_1 (see A, B and C in Figure 3.8(a)) as the initial conditions and integrate forward to see their evolution. Note that all the trajectories corresponding to these three points have the same initial energy and start from a configuration identical to the equilibrium point W_1 , but with different initial velocity directions. Figure 3.8(b) shows the trajectories A and B in the conservative system where A is outside the tube boundary and B is inside the tube boundary. In the figure, trajectory B transits through the neck region and trajectory A bounces back. Figure 3.8(c) shows trajectories B and C in the dissipative system. Like the situation in the conservative system, trajectory C which is inside the tube can transit, while trajectory B which is outside the tube cannot. Figure 3.8(d) shows the effect of damping on the transit condition for the trajectories B and B' with the same initial condition. Trajectory B is simulated using the conservative system and trajectory B' is simulated using the dissipative system. It shows that the damping changes the transit condition that a transit orbit B in the conservative system becomes non-transit orbit B' in the dissipative system, both starting from

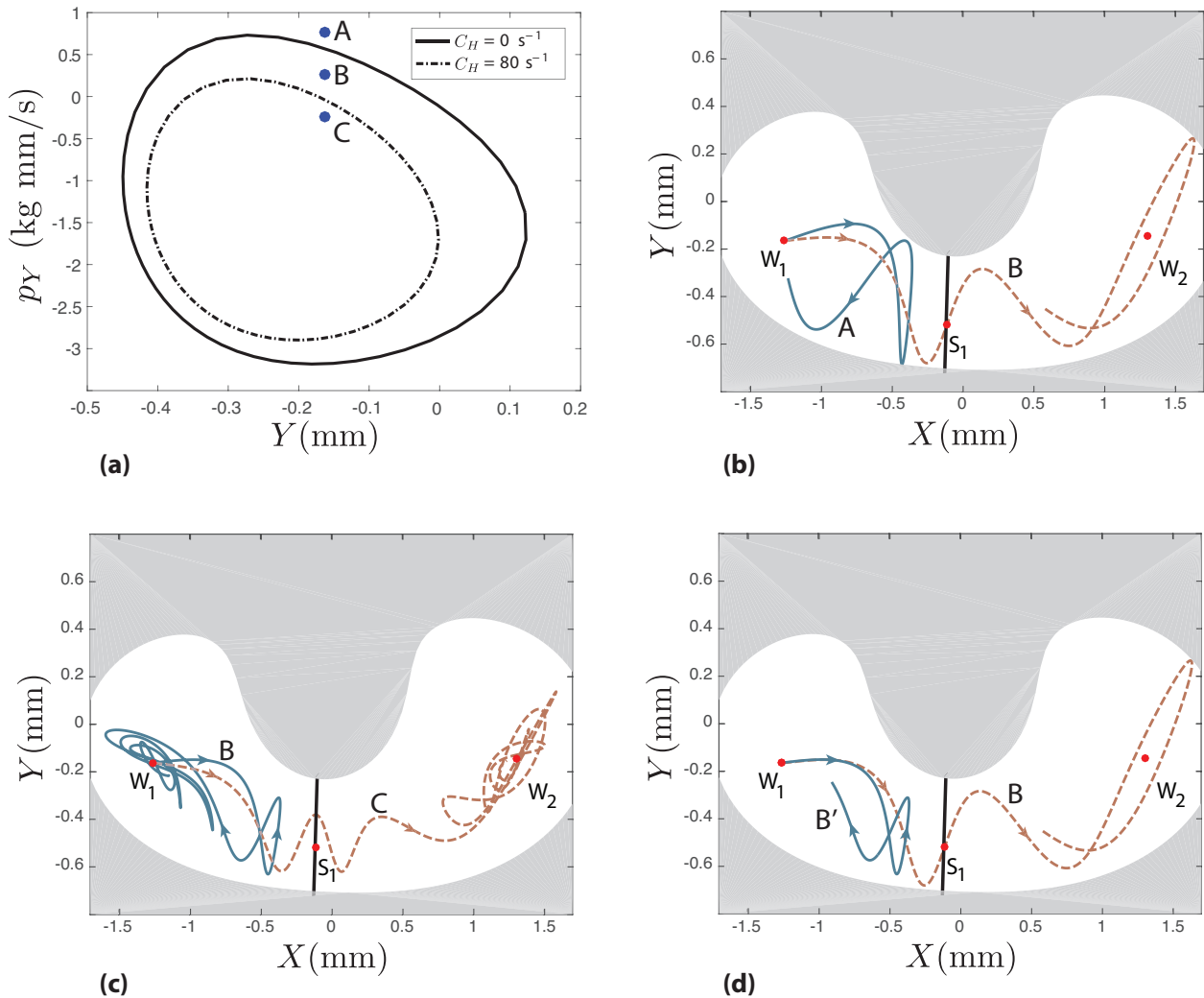


Figure 3.8: Several example trajectories are shown, starting from the stable well point W_1 . The initial conditions from Poincaré section Σ_1 are shown in (a) for a fixed initial energy, along with the transition tube boundaries for the conservative case and a damped case. In (b), we show the trajectories for points A and B, for the conservative case where A is just outside the tube boundary and B is just inside. In (c), we show the trajectories for points B and C, for the damped case where B is just outside the tube boundary and C is just inside. In (d), we illustrate the effect of damping by starting the same initial condition, B, but showing the trajectory in the conservative case as trajectory B and the damped case as trajectory B'.

the same initial condition. From Figure 3.8, we can conclude the transition tube can effectively estimate the snap-through transitions both in the conservative systems and dissipative systems.

Finally, we point out that the transition tubes are the boundary for transit orbits that transition *the first time*. For example, trajectory A in Figure 3.8(b) stays outside of the transition tube so

that it returns near the neck region at first, but, unless it happens to be on a KAM torus or a stable manifold of such a torus, it will ultimately transit as long as it does not form a periodic orbit near the potential well W_1 , since the energy is above the critical energy for transition and is conservative.

3.4 Conclusions

Tube dynamics is a conceptual dynamical systems framework initially used to study the isomerization reactions in chemistry [12, 13, 14, 15, 30] as well as other fields, like resonance transitions in celestial mechanics [9, 11, 17, 18, 31] and capsizing in ship dynamics [8]. Here we extend the application of tube dynamics to structural mechanics: the snap-through of a shallow arch, or buckled-beam. In general, slender elastic structures are capable of exhibiting a variety of (co-existing) equilibrium shapes, and thus, given a disturbance, tube dynamics sheds light on how such a system might be caused to transition between available, stable equilibrium configurations. Moreover, it is the first time, to the best of our knowledge, that tube dynamics has been worked out for a dissipative system, which increases the generality of the approach.

The snap-through transition of an arch was studied via a two-mode truncation of the governing partial differential equations based on Euler-Bernoulli beam theory. Via analysis of the linearized Hamiltonian equations around the saddle, the analytical solutions for both the conservative and dissipative systems were determined and the corresponding flows in the equilibrium region of eigenspace and configuration space were discussed. The results show that all transit orbits, corresponding to snap-through, must evolve from a wedge of velocities which are restricted to a strip in configuration space in the conservative system, and by an ellipse in the corresponding dissipative system when damping is included. Using the results from the linearization as an approximation, the transition tubes based on the full nonlinear equations for both the conservative and dissipative system were obtained by the bisection method. The orbits inside the transition tubes can transit, while the orbits outside the tubes cannot. Results also show that the damping makes the size of the transition tubes smaller, which corresponds to the degree, or amount, of orbits that transit. When the damping is small, it has a nearly linear effect on the size of the transition tubes.

Further study of the dynamic behaviors of the arch can lead to more immediate application structural mechanics. For example, many structural systems possess multiple equilibria, and the manner in which the governing potential energy changes with a control parameter is, of course, the essence of bifurcation theory. However, under nominally fixed conditions, the present study directly assesses the energy required to (dynamically) perturb a structural system beyond the confines of its

immediate potential energy well. In future work, a three-mode truncation may be introduced to study such systems. High order approximations will present higher index saddles which will modify the tube dynamics framework presented here (cf. [32, 33, 34]). Furthermore, experiments will be carried out to show the effectiveness of the present approach to prescribe initial conditions which lead to dynamic buckling.

Acknowledgments

This work was supported in part by the National Science Foundation under awards 1150456 (to SDR) and 1537349 (to SDR and LNV). The authors would like to thank Professor Raymond Plaut and an anonymous reviewer for their useful comments and suggestions. One of the authors (SDR) acknowledges enjoyable interactions during the past decade with Professor Romesh Batra, who is being honored by this issue.

Bibliography

- [1] R. Wiebe, L. N. Virgin, On the experimental identification of unstable static equilibria, *Proceedings of the Royal Society of London A: Mathematical, Physical and Engineering Sciences* 472 (2190) (2016) 20160172.
- [2] P. Collins, G. S. Ezra, S. Wiggins, Isomerization dynamics of a buckled nanobeam, *Physical Review E* 86 (5) (2012) 056218.
- [3] L. N. Virgin, Y. Guan, R. H. Plaut, On the geometric conditions for multiple stable equilibria in clamped arches, *International Journal of Non-Linear Mechanics* 92 (2017) 8–14.
- [4] K. Das, R. C. Batra, Symmetry breaking, snap-through and pull-in instabilities under dynamic loading of microelectromechanical shallow arches, *Smart Materials and Structures* 18 (11) (2009) 115008.
- [5] K. Das, R. C. Batra, Pull-in and snap-through instabilities in transient deformations of microelectromechanical systems, *Journal of Micromechanics and Microengineering* 19 (3) (2009) 035008.
- [6] B. P. Mann, Energy criterion for potential well escapes in a bistable magnetic pendulum, *Journal of Sound and Vibration* 323 (3) (2009) 864–876.
- [7] J. M. T. Thompson, G. W. Hunt, *Elastic Instability Phenomena*, Wiley, 1984.
- [8] S. Naik, S. D. Ross, Geometry of escaping dynamics in nonlinear ship motion, *Communications in Nonlinear Science and Numerical Simulation* 47 (2017) 48 – 70, ISSN 1007-5704.
- [9] W. S. Koon, M. W. Lo, J. E. Marsden, S. D. Ross, Heteroclinic connections between periodic orbits and resonance transitions in celestial mechanics, *Chaos* 10 (2000) 427–469.
- [10] C. C. Conley, Low energy transit orbits in the restricted three-body problem, *SIAM Journal on Applied Mathematics* 16 (1968) 732–746.

- [11] J. Llibre, R. Martinez, C. Simó, Transversality of the invariant manifolds associated to the Lyapunov family of periodic orbits near L2 in the restricted three-body problem, *Journal of Differential Equations* 58 (1985) 104–156.
- [12] A. M. Ozorio de Almeida, N. De Leon, M. A. Mehta, C. C. Marston, Geometry and dynamics of stable and unstable cylinders in Hamiltonian systems, *Physica D* 46 (1990) 265–285.
- [13] N. De Leon, M. A. Mehta, R. Q. Topper, Cylindrical manifolds in phase space as mediators of chemical reaction dynamics and kinetics. I. Theory, *The Journal of chemical physics* 94 (1991) 8310–8328.
- [14] N. De Leon, Cylindrical manifolds and reactive island kinetic theory in the time domain, *The Journal of chemical physics* 96 (1992) 285–297.
- [15] R. Q. Topper, Visualizing molecular phase space: nonstatistical effects in reaction dynamics, in: K. B. Lipkowitz, D. B. Boyd (Eds.), *Reviews in Computational Chemistry*, vol. 10, chap. 3, VCH Publishers, New York, 101–176, 1997.
- [16] F. Gabern, W. S. Koon, J. E. Marsden, S. D. Ross, Theory and Computation of Non-RRKM Lifetime Distributions and Rates in Chemical Systems with Three or More Degrees of Freedom, *Physica D* 211 (2005) 391–406.
- [17] F. Gabern, W. S. Koon, J. E. Marsden, S. D. Ross, T. Yanao, Application of tube dynamics to non-statistical reaction processes, *Few-Body Systems* 38 (2006) 167–172.
- [18] J. E. Marsden, S. D. Ross, New methods in celestial mechanics and mission design, *Bulletin of the American Mathematical Society* 43 (2006) 43–73.
- [19] W. S. Koon, M. W. Lo, J. E. Marsden, S. D. Ross, *Dynamical Systems, the Three-Body Problem and Space Mission Design*, Marsden Books, ISBN 978-0-615-24095-4, 2011.
- [20] K. D. Murphy, L. N. Virgin, S. A. Rizzi, Experimental snap-through boundaries for acoustically excited, thermally buckled plates, *Experimental Mechanics* 36 (1996) 312–317.
- [21] R. Wiebe, L. N. Virgin, I. Stanciulescu, S. M. Spottswood, T. G. Eason, Characterizing Dynamic Transitions Associated with Snap-Through: A Discrete System, *Journal of Computational and Nonlinear Dynamics* 8.
- [22] J. Zhong, Y. Fu, Y. Chen, Y. Li, Analysis of nonlinear dynamic responses for functionally graded beams resting on tensionless elastic foundation under thermal shock, *Composite Structures* 142 (2016) 272–277.

- [23] A. M. Bloch, P. Krishnaprasad, J. E. Marsden, R. M. Murray, Nonholonomic mechanical systems with symmetry, *Archive for Rational Mechanics and Analysis* 136 (1) (1996) 21–99.
- [24] D. T. Greenwood, *Advanced Dynamics*, Cambridge University Press, 2003.
- [25] J. Zhong, L. N. Virgin, S. D. Ross, A tube dynamics perspective governing stability transitions: An example based on snap-through buckling, *International Journal of Mechanical Sciences* 149 (2018) 413–428.
- [26] R. L. Anderson, R. W. Easton, M. W. Lo, Isolating blocks as computational tools in the circular restricted three-body problem, *Physica D: Nonlinear Phenomena* 343 (2017) 38 – 50, ISSN 0167-2789.
- [27] K. Onozaki, H. Yoshimura, S. D. Ross, Tube dynamics and low energy Earth-Moon transfers in the 4-body system, *Advances in Space Research* 60 (2017) 2117–2132.
- [28] E. S. Gawlik, J. E. Marsden, P. C. Du Toit, S. Campagnola, Lagrangian coherent structures in the planar elliptic restricted three-body problem, *Celestial Mechanics and Dynamical Astronomy* 103 (2009) 227–249.
- [29] R. S. MacKay, Flux over a saddle, *Physics Letters A* 145 (1990) 425–427.
- [30] C. Jaffé, D. Farrelly, T. Uzer, Transition state in atomic physics, *Physical Review A* 60 (1999) 3833–3850.
- [31] C. Jaffé, S. D. Ross, M. W. Lo, J. E. Marsden, D. Farrelly, T. Uzer, Theory of asteroid escape rates, *Physical Review Letters* 89 (2002) 011101.
- [32] P. Collins, G. S. Ezra, S. Wiggins, Index k saddles and dividing surfaces in phase space with applications to isomerization dynamics, *The Journal of chemical physics* 134 (24) (2011) 244105.
- [33] G. Haller, T. Uzer, J. Palacian, P. Yanguas, C. Jaffe, Transition state geometry near higher-rank saddles in phase space, *Nonlinearity* 24 (2) (2011) 527.
- [34] Y. Nagahata, H. Teramoto, C.-B. Li, S. Kawai, T. Komatsuzaki, Reactivity boundaries for chemical reactions associated with higher-index and multiple saddles, *Physical Review E* 88 (2013) 042923.

Chapter 4

On the invariant manifold governing transition in snap-through buckling

Attribution

This chapter represents a collaborative work with Shane D. Ross. This work has not been published yet.

Abstract

Invariant manifold plays an essential rule in organizing local and global dynamical behaviors. For example, we notice that in multi-well conservative systems where the potential wells are usually connected by an index-1 saddle, the motion between potential wells is governed by the invariant manifold of a periodic orbit around the saddle. In this chapter, we use the concept of the invariant manifold to study the transition boundary of a given energy using the snap-through of a shallow arch as an example. Since the computation of the invariant manifold of a periodic orbit in the conservative systems is well developed, our focus will be on the invariant manifold of a saddle point in a dissipative system. We present a boundary-value problem (BVP) approach to compute such manifold. The boundary conditions on one end are selected on a hyper-sphere in the stable subspace of the linearized system about the saddle and the boundary conditions on the other end are determined by the energy. The algorithms are implemented in a MATLAB-based continuation package COCO. We find that the results obtained by the current method match well with the

results predicted by the bisection method in the previous chapter.

4.1 Introduction

From the study of the linearized dynamics in Chapter 2, we found the transition boundary of a specific given initial energy goes from a cylindrical tube in the conservative system to an ellipsoid in the dissipative system, named as transition tube and transition ellipsoid, respectively. The transition tube and transition ellipsoid are the invariant manifold of the periodic orbit and the index-1 saddle in the conservative and dissipative systems, respectively. In Chapter 3, a bisection method was proposed to compute the transition boundary on a specific Poincaré section for both conservative and dissipative systems. It is regretful that the structure of the transition boundary in the full phase space that governs the transition was not discussed, although it can be obtained by selecting a bunch of Poincaré sections. This method is versatile but sometimes is time-consuming if too many Poincaré sections are considered. It will even fail if the shape of the transition boundary on a Poincaré section is irregular and distorted. In this chapter, we aim to present a boundary-value problem (BVP) approach to compute the transition boundary in a full nonlinear sense from the perspective of the invariant manifold.

In dynamical systems, the invariant manifold is critical to know the global dynamical structure. In general, the global invariant manifold in a nonlinear system can not be obtained analytically. Thus, numerical computational algorithms are necessary. Suppose we have a dynamical system written as

$$\frac{dx}{dt} = f(x), \quad (4.1)$$

where $x \in \mathbb{R}^n$ and the vector field $f: \mathbb{R}^n \mapsto \mathbb{R}^n$ is sufficiently smooth. Here the dot over the quantity is the derivative with respect to time. The system is assumed to have a hyperbolic equilibrium point at $x = x_e$ that satisfies $f(x_e) = 0$. Its Jacobian matrix $Df(x_e)$ has k eigenvalues with negative real part and $n - k$ eigenvalues with positive real part. The eigenvectors corresponding to the eigenvalues with negative and positive real parts are denoted by \mathbf{u} and \mathbf{v} , respectively. Thus, the spaces spanned by \mathbf{u} and \mathbf{v} are referred to as the stable and unstable subspaces of the linearized system, denoted by E_s and E_u , which are defined as

$$\begin{aligned} E_s &= \text{span}\{u_1, u_2, \dots, u_k\}, \\ E_u &= \text{span}\{v_1, v_2, \dots, v_{n-k}\}. \end{aligned} \quad (4.2)$$

From the Theorem of Local Stable and Unstable Manifold [1, 2, 3], there exists a k -dimensional invariant local stable manifold and a $(n - k)$ -dimensional invariant unstable manifold, denoted by

$W_{loc}^s(x_e)$ and $W_{loc}^u(x_e)$, which are tangent to E_s and E_u at x_e , respectively. After the local stable and unstable invariant manifolds are established, the global stable and unstable invariant manifold can be grown from the corresponding local invariant manifold [1, 2, 3, 4] which are defined by

$$\begin{aligned} W^s(x_e) &= \left\{ x \in \mathbb{R}^n \mid \lim_{t \rightarrow \infty} \phi_t(x) = x_e \right\} = \bigcup_{t \geq 0} \phi_t(W_{loc}^s(x_e)), \\ W^u(x_e) &= \left\{ x \in \mathbb{R}^n \mid \lim_{t \rightarrow -\infty} \phi_t(x) = x_e \right\} = \bigcup_{t \leq 0} \phi_t(W_{loc}^s(x_e)), \end{aligned} \tag{4.3}$$

where ϕ_t is the flow of the nonlinear system given in (4.1). From the definitions of the invariant manifolds in (4.3), it is intuitive to compute the global invariant manifold by numerical integration using a batch of initial conditions on a $(k - 1)$ -dimensional hyper-sphere with a small radius δ centered at x_e in the corresponding subspace. This idea works well for the one dimensional invariant manifold of the equilibrium point embedded in any dimensional space [5]. However, some challenges [6] may appear when computing the higher dimensional invariant manifold, like the large aspect ratios of the manifold surface due to the significant difference in real part of the eigenvalues and the trajectories on the manifold will be attracted to the most stable direction [7]. In this case, growing the invariant manifold directly from the local initial sphere is impractical. Other methods can be found in a review paper [4] about computing the global invariant manifolds and interested readers are referred to it for more details.

[6] presents an idea of solving a suitable two-point boundary-value problem to compute the global invariant manifold as a family of orbit segments. It has been applied to some examples to compute the two dimensional manifold formed by a family of geodesic level sets. Starting from another perspective similar to the well known cell-mapping method, a special box covering technique [8, 9] was developed to compute the invariant manifolds. A subdivision algorithm is used to produce the local invariant manifold first and then a box-oriented continuation technique is applied to extend it to the global manifold with larger parts. Theoretically, this technique is applicable to compute the invariant manifold of arbitrary dimension. However, due to the large number of boxes used in high dimensional systems that will slow down the computation, only moderate dimensional problems are considered to be practical. The Lagrangian descriptor (LD) [10, 11] is a trajectory-based diagnostic method, initially developed in the context of transport in fluid mechanics, to detect the invariant manifold [12, 13]. It measures the geometrical properties of particle trajectories, such as the arc-length, within a fixed forward and backward time starting at given initial conditions. Since it is an integration method, its computational expenses still need to be examined.

In this chapter, we present an idea of computing the transition boundary of initial conditions subjected to a given energy by computing the invariant manifold by solving two-point boundary

value problems applied to the snap-through of a shallow arch (or buckled beam) with energy dissipation. The algorithm is implemented in a MATLAB-based package COCO [14]. From our results, it is found that the boundary of initial conditions for the transit orbits of a fixed initial energy is the transition tube and transition ellipsoid in the conservative and dissipative systems, respectively, which is an extension of the linearized dynamics around the saddle in Chapter 2.

4.2 Algorithms for computing the invariant manifolds

4.2.1 Invariant manifold of a periodic orbit

In this part, we aim to discuss the invariant manifold of a periodic orbit. It has two separate parts, the first part about the algorithm to compute a periodic orbit, and the second part about the computation of stable and unstable manifolds of the periodic orbit.

Periodic orbits. A solution of the dynamical system (4.1) is a periodic orbit [15] if there exists a least time interval $T > 0$ which satisfies $x(t + T) = x(t)$ for all t . Multiple methods have been developed to compute the periodic orbits, such as the method of multiple scales [16, 17], incremental harmonic balance method [18, 19], differential correction (or shooting method) [5, 20, 21], to name but a few. In the following, we will introduce another efficient BVP approach which can compute the periodic orbits very accurately. Before discussing this approach, we rescale the time by introducing the linear transformation, $\tau = t/T$, so that the period T appears explicitly in the equations of motion. Thus, the equations in (4.1) can be rewritten as

$$\frac{dx}{d\tau} = Tf(x), \quad 0 \leq \tau \leq 1, \quad (4.4)$$

where T is the unknown period. For the periodic orbits, we have the periodicity condition,

$$x(0) = x(1). \quad (4.5)$$

However, (4.4) and (4.5) do not uniquely determine the periodic solution, since if $x(t)$ is a periodic solution, so is $x(t + \delta)$. To avoid the arbitrary phase shift δ , the following integral phase condition [14, 15, 22] is widely used,

$$\int_0^T [x(t) - x^*(t)]^T f(x(t)) dt = \int_0^1 [x(\tau) - x^*(\tau)]^T f(x(\tau)) d\tau = 0, \quad (4.6)$$

where $x^*(t)$ is a known nearby solution. Now the boundary value problem is ready to be solved. For the complexity of the nonlinearity in the system, some numerical methods are needed. For such numerical process, there exists several software tools, such as AUTO [23], MATCONT [24], and COCO [14]. COCO is a MATLAB continuation package that embeds the algorithm described here for computing the periodic orbits to a *po* toolbox which uses the collocation method and pseudo-arclength method for numerical continuation. In this chapter, we will apply COCO to compute the periodic orbits.

Invariant manifold of the periodic orbits. As mentioned in the Introduction, the general way of computing the global invariant manifold is to globalize the local invariant manifold of the corresponding linearized system. Thus, here we can first find the local approximations of the manifold of the periodic orbit from the eigenvectors of the monodromy matrix and then grow the linear approximations by integrating the nonlinear equations of motion (4.1). The procedure is known as globalization of the manifolds. Before growing the invariant manifold of the periodic orbit, we need to compute the state transition matrix $\Phi(t)$ along the periodic orbit which can be obtained by numerically solving the following variational equations from time 0 to T ,

$$\dot{\Phi}(t, t_0) = Df(\bar{x}(t))\Phi(t, t_0), \quad \Phi(t_0, t_0) = I_n \quad (4.7)$$

Once the monodromy matrix $M = \Phi(T)$ is obtained, its eigenvalues can be computed numerically. For the two-mode Hamiltonian system for the shallow arch discussed in the previous chapter, we can conclude from [20] that the four eigenvalues of M include one real pair and one pair equal to unity,

$$\lambda_1 > 1, \quad \lambda_2 = \frac{1}{\lambda_1}, \quad \lambda_3 = \lambda_4 = 1. \quad (4.8)$$

From [20], we know the eigenvector associated with λ_1 is in the unstable direction, while the eigenvector associated with eigenvalue λ_2 is in the stable direction. Denote the stable and unstable eigenvectors by $Y^s(X_0)$ and $Y^u(X_0)$, respectively, normalized to unity. In this setting, we can obtain the initial guesses for the stable and unstable manifolds, denoted by $X^s(X_0)$ and $X^u(X_0)$, at X_0 along the periodic orbit written in the following form

$$\begin{aligned} X^s(X_0) &= X_0 + \epsilon Y^s(X_0), \\ X^u(X_0) &= X_0 + \epsilon Y^u(X_0), \end{aligned} \quad (4.9)$$

where ϵ is a small displacement amplitude from X_0 . The magnitude of ϵ should be small enough so that the linear estimate can satisfy the accuracy, yet not so small that the time to obtain the global manifold becomes large due to the asymptotic behavior of the stable and unstable manifolds.

Once we obtain the initial guess for the stable and unstable manifolds at X_0 , it is straightforward to globalize the manifold. By numerically integrating the unstable vector forwards in time, using both ϵ and $-\epsilon$, we generate the trajectories shadowing the two branches, W^{u+} and W^{u-} , of the unstable manifold of the periodic orbit. Similarly, by integrating the stable vector backwards, we generate a trajectory shadowing the stable manifold, $W^{s\pm}$. For the manifold at $X(t)$, we can simply use the state transition matrix to transport the eigenvectors from X_0 to $X(t)$:

$$Y^s(X(t)) = \Phi(t, 0)Y^s(X_0). \quad (4.10)$$

Since the state transition matrix does not preserve the norm, the resulting vector must be renormalized.

4.2.2 Invariant manifold of an equilibrium point

In the previous section, we discussed the approach to compute a periodic orbit and its stable and unstable invariant manifold in the conservative system. The invariant manifold is the boundary of the initial conditions for those trajectories that will soon escape. After clarifying this, it is intuitive to think about what the phase space structure will be that governs the transition in the dissipative system. In this part, we address this concern by computing the invariant manifold of an equilibrium point in a dissipative system.

We use the same general form of a dynamical system in (4.1) to define the dissipative system with equilibrium point denoted by \mathbf{x}_e . The Jacobian $Df(\mathbf{x}_e)$ of the equilibrium point has k eigenvalues with negative real part. The real parts of the k eigenvalues and the corresponding generalized eigenvectors are written as λ_i^s and \mathbf{u}_i ($i = 1, \dots, k$), respectively. Thus, the saddle has a k -dimensional local, stable invariant manifold, denoted by $W_{loc}^s(\mathbf{x}_e)$, which is tangent to the respective invariant stable subspaces, E^s , of the linearized system about the saddle spanned by the stable eigenvectors \mathbf{u}_i .

After we determine the local stable manifold, it can be globalized to obtain the global k -dimensional stable manifold $W^s(\mathbf{x}_e)$ [4]. The direct way to obtain the manifold is to select an initial condition in the stable subspace with a small distance from the equilibrium point and integrate backward in time so that one orbit segment on the stable manifold can be obtained. The continuation by using the orbit as a starting solution might give the global manifold. However, some challenges [6] may appear, such as the large aspect ratios of the manifold surface due to the tremendous difference in the real part of the eigenvalues and the great distortion of the initial conditions after a long period of integration due to the nonlinearity of the system. To solve these problems, new mesh points on

the hyper manifold surface is needed which is also challenging.

Another way of obtaining the stable manifolds is solving a proper two-point boundary-value problem (BVP) [22] which can control the endpoints of the trajectories on the manifold. Before describing the process, we need to rescale the time by $t = T\tau$ which puts (4.1) into the same form as (4.4) where τ varies from 0 to 1. It should be mentioned that, compared to the period T of a periodic orbit in the conservative system, T here in the dissipative case is the time length of a trajectory on the invariant manifold of the saddle. We can consider T as either a parameter or a function whose derivative with respect to τ is zero, i.e., $dT/d\tau = 0$. Here we will use the latter one. To form a complete BVP set-up, we still need some boundary conditions. The boundary conditions at $\tau = 0$ can be selected on the initial hyper-sphere on the stable subspace given by

$$\mathbf{x}(0) = \mathbf{x}_e + r_0 \sum_{i=1}^k a_i \mathbf{u}_i, \quad (4.11)$$

where a_i are parameters controlling the direction of the velocity; r_0 is the radius of the initial sphere centered at the equilibrium point. The value of r_0 should be appropriately selected, neither too small nor too large.

In the following, we will take the snap-through of a shallow arch with damping as an example. The equations for the boundary-value problem to compute the invariant manifold of the rank-1 saddle are,

$$\begin{aligned} \dot{X} &= \frac{p_X}{M_1}, & \dot{Y} &= \frac{p_Y}{M_2}, \\ \dot{p}_X &= -\frac{\partial \mathcal{V}}{\partial X} - C_{HPX}, & \dot{p}_Y &= -\frac{\partial \mathcal{V}}{\partial Y} - C_{HPY}, & \dot{T} &= 0. \end{aligned} \quad (4.12)$$

where $\partial \mathcal{V}/\partial X$ and $\partial \mathcal{V}/\partial Y$ are given in (3.27).

In the dissipative system, the rank-1 saddle has a three-dimensional stable invariant manifold. Thus, the boundary conditions at the initial points can be selected on the 2-sphere with radius r_0 given by

$$\mathbf{x}(0) = \mathbf{x}_e + r_0 (\sin \theta \sin \phi \mathbf{u}_1 + \sin \theta \cos \phi \mathbf{u}_2 + \cos \theta \mathbf{u}_3) \quad (4.13)$$

where θ and ϕ are the two parameters. Notice that there are 4 boundary conditions in (4.13). We still need one more boundary condition at $\tau = 1$. We can have several choices, such as the energy, arclength or time of the trajectories. In current problem we want to find out the transition boundary of the dissipative system subjected to a specific energy, h . Thus, the best way is to assign the given energy to the endpoint at $\tau = 1$. The boundary condition there is given by,

$$E[\mathbf{x}(1)] = \mathcal{H}[X(1), Y(1), p_X(1), p_Y(1)] = h, \quad (4.14)$$

After we set up the boundary-value problem, we can apply numerical continuation to obtain the invariant manifold of the system. Before solving the boundary-value problem, we need to specify r_0 and h , so we have 5 variables (X , Y , p_X , p_Y , and T) and 2 parameters (θ and ϕ). On the other hand, we have 5 boundary conditions in (4.13) and (4.14). Thus, the BVP set-up is a two-parameter continuation. To simplify the continuation process, we want to reduce the system to a one-parameter continuation.

For the three stable eigenvectors \mathbf{u}_1 , \mathbf{u}_2 , and \mathbf{u}_3 , we assume the eigenvalue associated with \mathbf{u}_1 has the largest absolute value. Thus, \mathbf{u}_1 is in the most stable direction. In fact, \mathbf{u}_1 is a stable direction without any focus component. It has the largest possibility to escape from the potential well. If we take $\theta = \phi = \pi/2$ in (4.13) and use it as an initial condition to numerically integrate (4.12) backward in time until the trajectory reaching the specific energy h , we can reach the end of the nonlinear transition ellipsoid. Since this trajectory is approaching the saddle in forward time along the most stable direction, it is the fastest stable asymptotic orbit to the saddle. We refer it to as the *fastest trajectory*. In the following, we will use it as a reference trajectory to determine the Poincaré section.

Let \mathbf{r} denote the position vector of an arbitrary point on the fastest trajectory in X - Y - p_Y space. We can obtain the tangent vector $\boldsymbol{\tau}$ of that point along the fastest trajectory,

$$\boldsymbol{\tau} = \frac{\partial \mathbf{r}}{\partial s} = \frac{\partial X}{\partial s} \mathbf{e}_X + \frac{\partial Y}{\partial s} \mathbf{e}_Y + \frac{\partial p_Y}{\partial s} \mathbf{e}_{p_Y} = \frac{\dot{X}}{\dot{s}} \mathbf{e}_X + \frac{\dot{Y}}{\dot{s}} \mathbf{e}_Y + \frac{\dot{p}_Y}{\dot{s}} \mathbf{e}_{p_Y}, \quad (4.15)$$

where \mathbf{e}_X , \mathbf{e}_Y , and \mathbf{e}_{p_Y} are the corresponding basis vectors. Here s is the arclength of the reference trajectory in X - Y - p_Y space defined by

$$s(\tau) = \int_0^\tau \sqrt{\dot{X}^2 + \dot{Y}^2 + \dot{p}_Y^2} d\tau. \quad (4.16)$$

For a specific point (X_0, Y_0, p_{Y0}) on the fastest trajectory, we can choose a plane at that point vertical to $\boldsymbol{\tau}$ as the Poincaré section. The mathematical expression of such plane is given by

$$\tau_x(X(1) - X_0) + \tau_y(Y(1) - y_0) + \tau_{p_y}(p_Y(1) - p_{Y0}) = 0, \quad (4.17)$$

where τ_X , τ_Y , and τ_{p_Y} are the components of the tangent vector $\boldsymbol{\tau}$ along X , Y , and p_Y axes, respectively. In this case, we have one more algebraic equation which reduces the problem to a one-parameter continuation. Figure 4.1 shows the process of selecting proper Poincaré sections and the way to do the continuation on such Poincaré sections. The whole process of solving the BVP continuation will be implemented in COCO again to compute the invariant manifold of the saddle. In this way we can obtain the transition boundary in the dissipative system.

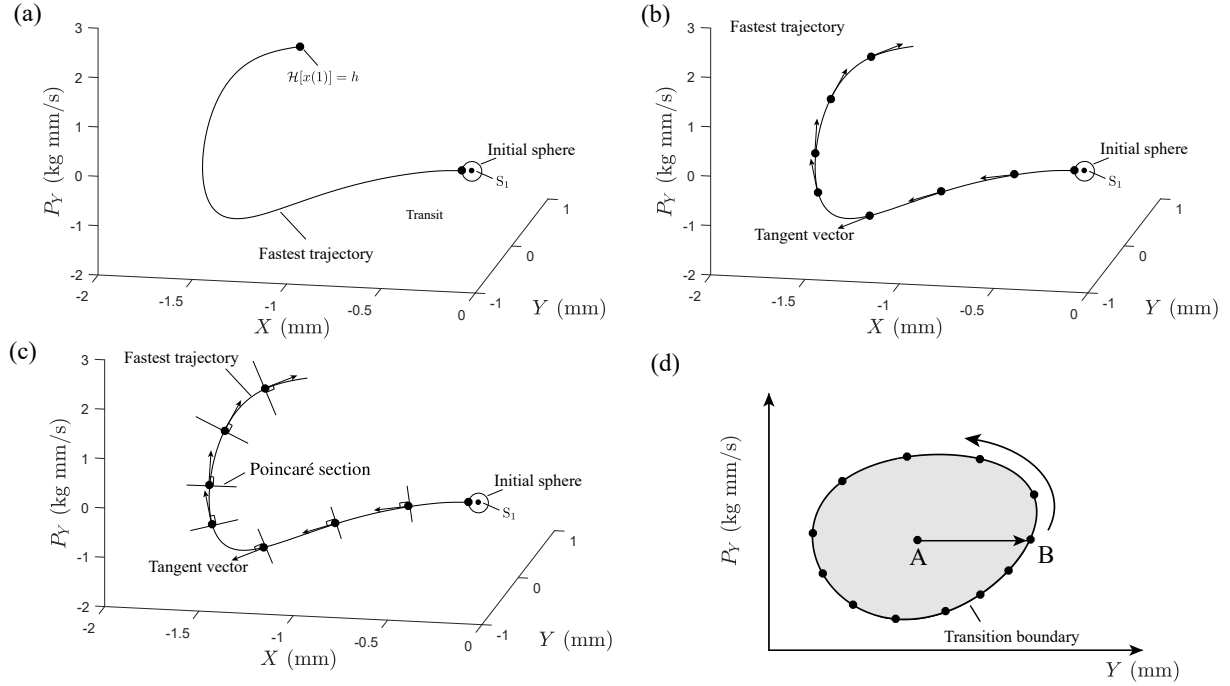


Figure 4.1: Illustration of selecting an extra Poincaré section to reduce the two-parameter continuation to a one-parameter continuation: (a) Select the initial condition of the fastest trajectory on the initial sphere (with radius r_0) in the stable subspace of the linearized system and numerically integrate the nonlinear equations until the trajectory reaches the given energy h . For the selection of the points, the easiest way is meshing by arc-length. Of course, for the area with large curvature, more points can be selected; (2) Select some points on the fastest trajectory and compute the tangent vector at each point along the fastest trajectory; (3) Finally the plane normal to the tangent vector at each point can be selected as the Poincaré section; (4) After we determine the Poincaré sections, we can obtain the intersection of the fastest trajectory on one Poincaré section, labeled by A. In general point A has lower energy than the given energy h . We can fix p_Y and commit the continuation along Y direction until the Hamiltonian reaches h so that we can obtain point B on the transition boundary. Then we can use Point B as the starting solution and do the continuation by fixing the Hamiltonian as h by which we can obtain the transition boundary on the Poincaré section.

4.3 Numerical results

In this section, we will give the geometry of escape dynamics in the nonlinear snap-through of a shallow arch in both the conservative and dissipative systems. As discussed in Section 4.2, the periodic orbit and the invariant manifold of a saddle are obtained by BVP approaches. Such BVP

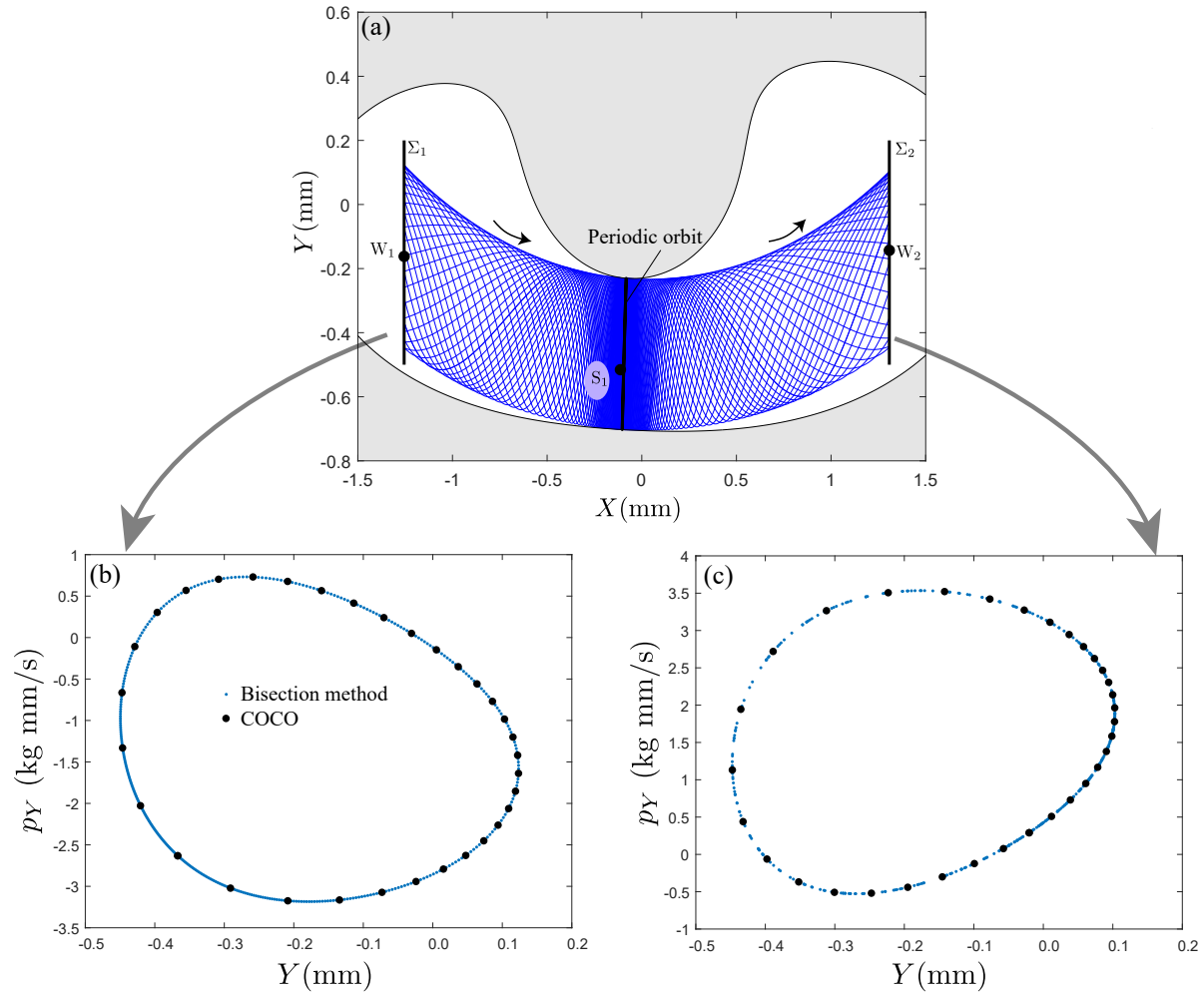


Figure 4.2: A transition tube from the left well to the right well in the conservative system obtained by the BVP approach: (a) shows the transition tube projected onto configuration space. (b) and (c) give the transition boundaries on the Poincaré sections Σ_1 and Σ_2 in the conservative systems. In order to compare the efficiency of the current method, we also present the transition boundary obtained by the bisection method.

approaches are implemented in COCO [14]. In the corresponding examples, the geometrical and material parameters are selected as the same as Chapter 3: the geometries of the beam are selected as $b = 12.7$ mm $d = 0.787$ mm, $L = 228.6$ mm; the Young's modulus and the mass density are $E = 153.4$ GPa and $\rho = 7567$ kg m⁻³; moreover, the selected thermal load corresponds to 184.1 N, while the initial imperfections are $\gamma_1 = 0.082$ mm and $\gamma_2 = -0.077$ mm.

4.3.1 Conservative systems

In this part, we give some examples about the nonlinear dynamics in the conservative system. For the convenience of discussing the energy, we will use the excess energy ΔE [12] rather than the total energy E , where the excess energy is the difference of the total energy E_t and the critical energy E_c of the saddle point S_1 defined by $\Delta E = E_t - E_c$. For positive excess energy, the bottleneck region around the saddle is open, and the trajectories have a chance to escape from the potential well. Otherwise, it is closed and no transition is allowed.

Figure 4.2 gives a transition tube of excess energy $\Delta E = 3.68 \times 10^{-4}$ J in the conservative system obtained by the BVP approach. As already pointed out in Chapter 3, due to the conservation of the energy, the cross-sectional area of the transition tube keeps constant along the invariant manifold. Moreover, the size of the cross-sectional area of the transition tube is decided by the initial energy applied to the system. Larger energy input will give a larger transition tube. From the transition boundaries on the Poincaré sections Σ_1 and Σ_2 obtained by the BVP approach and the bisection method given in Figure 4.2(b) and Figure 4.2(c), we notice the two approaches predict very close results. It implies that two methods are both accurate. However, the BVP approach is much faster than the bisection method.

4.3.2 Dissipative systems

In this section, we focus on presenting the results of the transition boundary in the dissipative system of the snap-through of a shallow arch. In the conservative system, the energy keeps constant for all motions. However, in the dissipative system the energy is keeping decreasing. The topology of the phase space structure that governs the transition in the dissipative system will be different from that in the conservative system. For the numerical results in the dissipative system, if there is not specific mention, the damping is taken as $C_H = 80 \text{ s}^{-1}$. Moreover, around the saddle, we also give the periodic orbit.

Figure 4.3 shows the two transition ellipsoids with initial excess energy $\Delta E = 1.0 \times 10^{-4}$ J and $\Delta E = 1.0 \times 10^{-4}$ J, respectively. The corresponding configuration space projections are given on the right. It shows that the transition ellipsoid becomes bigger when the initial energy given to the system increases. Due to the presence of nonlinear effect in the system, the transition ellipsoids do not appear in a standard form as in the linearized system. However, their topologies are the same as those in linearized systems. In Figure 4.3, we also give the periodic orbits with the same energy. We notice that the periodic orbits are exactly on the boundary of the transition ellipsoids. In fact, the points on the periodic orbits are the initial conditions of the focus-type asymptotic

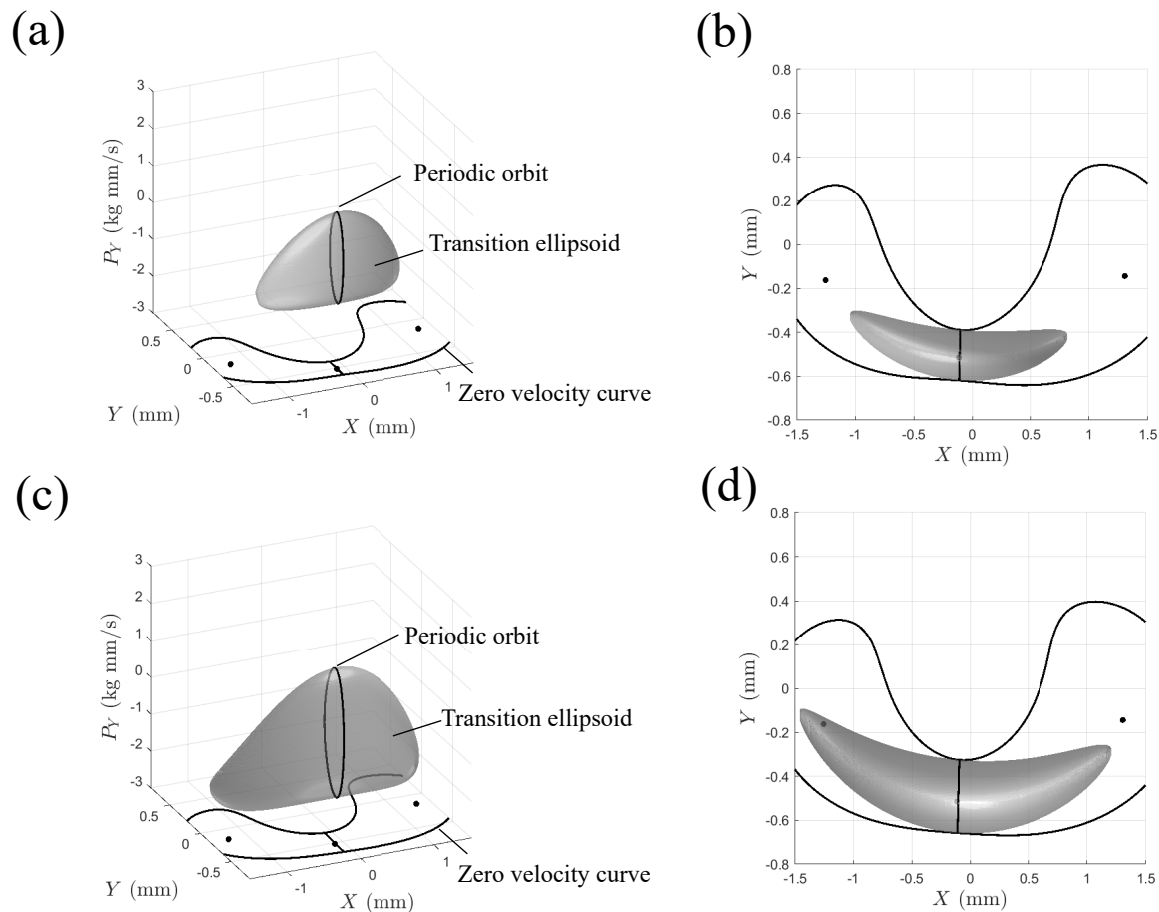


Figure 4.3: Transition ellipsoids in dissipative system obtained by the BVP approach: (a) and (c) show the three-dimensional transition ellipsoids with excess energy $\Delta E = 1.0 \times 10^{-4}$ J and $\Delta E = 2.0 \times 10^{-4}$ J, respectively; (b) and (d) show the corresponding configuration space projections.

orbits discussed in Chapter 2. Each periodic orbit divides the corresponding transition ellipsoid into two parts. The left part of the transition ellipsoid gives the initial conditions for the transit orbits moving from the left well to the right well, while the right part gives the initial conditions for the transit orbits moving from the right well to the left well.

Demonstration of transit and non-transit trajectories. In this part, we illustrate the effectiveness of the transition ellipsoid. We select two initial conditions on the Poincaré section Σ_1 , one inside and the other outside of the Poincaré section Σ_1 . After integrating the initial conditions

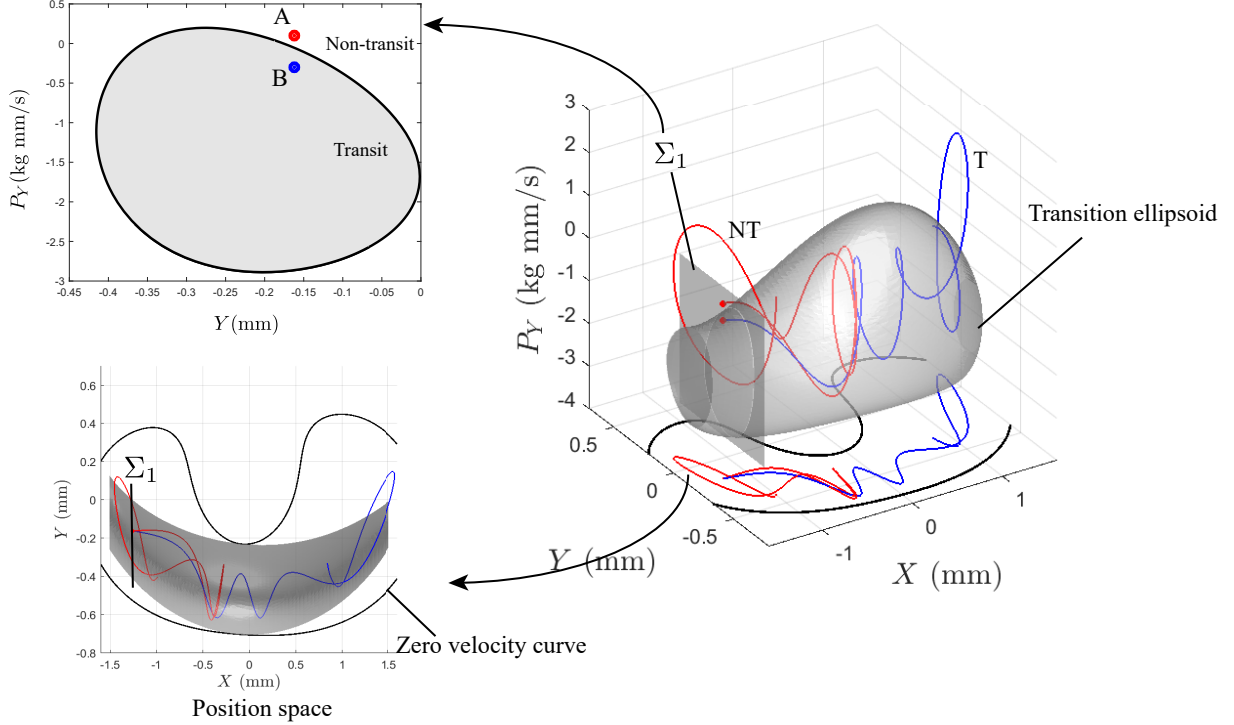


Figure 4.4: A transition ellipsoid in the dissipative system obtained by the BVP approach: the right figure shows the transition ellipsoid; the lower left shows the configuration space projection; the upper left shows the transition boundary, a closed curve, on the Poincaré section Σ_1 which separates the initial conditions with a given fixed energy for the transit and non-transit trajectories. A transit orbit and a non-transit trajectory starting with initial conditions labeled by A and B are shown, which are inside and outside of the transition boundary on the Poincaré section Σ_1 , respectively.

forward in time, we can obtain two trajectories. Figure 4.4 shows the transition ellipsoid and two trajectories with excess energy $\Delta E = 3.68 \times 10^{-4}$ J. From the figure, we find that trajectory B with the initial condition inside of the transition boundary escapes from the potential well W_1 and moves to the other potential well W_2 , while trajectory A with the initial condition outside of the transition boundary bounces back to the region of origin before crossing the bottleneck around the saddle. From Figure 4.4, we can conclude that the transition ellipsoid obtained by the BVP approach can accurately predict the snap-through transition with energy dissipation.

4.4 Conclusion

In this chapter, we seek to compute the transition boundaries in both the conservative and dissipative systems from the perspective of the invariant manifold of a periodic orbit and an index-1 saddle, respectively. Such invariant manifolds can be found numerically by solving proper boundary-value problems.

In the conservative system, the computational process about the invariant manifold has two steps, including the computation of the periodic orbit by solving a proper boundary-value problem and the globalization of the manifold. In the dissipative system, we compute the invariant manifold of a rank-1 saddle by another BVP continuation. First, we compute the stable subspace of the linearized system about the saddle. Then the points on an initial sphere selected in the subspace centered at the saddle and the energy at the other endpoint are used as the boundary conditions so that the invariant manifold of the saddle can be numerically obtained. The initial BVP set-up for the dissipative system is a two-parameter continuation. To reduce the difficulty of committing such continuation, extra Poincaré sections are introduced so that the problem becomes a one-parameter continuation. By using such approaches, we obtain the transition tube and transition ellipsoid for both the conservative and dissipative systems, respectively, which are topologically the same as those we obtained in Chapter 2 for the linearized dynamics. We conclude that the boundary-value problem approaches to compute the transition boundary in the nonlinear systems are effective.

Bibliography

- [1] J. D. Meiss, *Differential Dynamical Systems*, SIAM, 2007.
- [2] S. Wiggins, *Introduction to applied nonlinear dynamical systems and chaos*, vol. 2, Springer Science & Business Media, 2003.
- [3] L. Perko, *Differential equations and dynamical systems*, vol. 7, Springer Science & Business Media, 2013.
- [4] B. Krauskopf, H. M. Osinga, E. J. Doedel, M. E. Henderson, J. Guckenheimer, A. Vladimírsky, M. Dellnitz, O. Junge, A survey of methods for computing (un) stable manifolds of vector fields, in: *Modeling And Computations In Dynamical Systems: In Commemoration of the 100th Anniversary of the Birth of John von Neumann*, World Scientific, 67–95, 2006.
- [5] T. S. Parker, L. Chua, *Practical numerical algorithms for chaotic systems*, Springer Science & Business Media, 2012.
- [6] B. Krauskopf, H. M. Osinga, Computing geodesic level sets on global (un) stable manifolds of vector fields, *SIAM Journal on Applied Dynamical Systems* 2 (4) (2003) 546–569.
- [7] H. M. Osinga, Understanding the geometry of dynamics: The stable manifold of the Lorenz system, *Journal of the Royal Society of New Zealand* 48 (2-3) (2018) 203–214.
- [8] M. Dellnitz, A. Hohmann, A subdivision algorithm for the computation of unstable manifolds and global attractors, *Numerische Mathematik* 75 (3) (1997) 293–317.
- [9] M. Dellnitz, A. Hohmann, The computation of unstable manifolds using subdivision and continuation, in: *Nonlinear dynamical systems and chaos*, Springer, 449–459, 1996.
- [10] J. J. Madrid, A. M. Mancho, Distinguished trajectories in time dependent vector fields, *Chaos: An Interdisciplinary Journal of Nonlinear Science* 19 (1) (2009) 013111.

- [11] C. Mendoza, A. M. Mancho, Hidden geometry of ocean flows, *Physical review letters* 105 (3) (2010) 038501.
- [12] S. Naik, S. Wiggins, Finding normally hyperbolic invariant manifolds in two and three degrees of freedom with Hénon-Heiles-type potential, *Physical Review E* 100 (2) (2019) 022204.
- [13] A. M. Mancho, S. Wiggins, J. Curbelo, C. Mendoza, Lagrangian descriptors: A method for revealing phase space structures of general time dependent dynamical systems, *Communications in Nonlinear Science and Numerical Simulation* 18 (12) (2013) 3530–3557.
- [14] H. Dankowicz, F. Schilder, *Recipes for continuation*, vol. 11, SIAM, 2013.
- [15] R. Seydel, *Practical bifurcation and stability analysis*, vol. 5, Springer Science & Business Media, 2009.
- [16] A. H. Nayfeh, D. T. Mook, *Nonlinear oscillations*, John Wiley & Sons, 2008.
- [17] A. H. Nayfeh, B. Balachandran, *Applied nonlinear dynamics: analytical, computational, and experimental methods*, John Wiley & Sons, 2008.
- [18] S. Lau, Y. Cheung, Amplitude incremental variational principle for nonlinear vibration of elastic systems, *Journal of Applied Mechanics* 48 (4) (1981) 959–964.
- [19] Y. Fu, J. Hong, X. Wang, Analysis of nonlinear vibration for embedded carbon nanotubes, *Journal of Sound and Vibration* 296 (4-5) (2006) 746–756.
- [20] W. S. Koon, M. W. Lo, J. E. Marsden, S. D. Ross, *Dynamical Systems, the Three-Body Problem and Space Mission Design*, Marsden Books, ISBN 978-0-615-24095-4, 2011.
- [21] P. Sundararajan, S. Noah, *Dynamics of forced nonlinear systems using shooting/arc-length continuation method application to rotor systems* .
- [22] B. Krauskopf, H. M. Osinga, J. Galán-Vioque, *Numerical continuation methods for dynamical systems*, Springer, 2007.
- [23] E. J. Doedel, T. F. Fairgrieve, B. Sandstede, A. R. Champneys, Y. A. Kuznetsov, X. Wang, *AUTO-07P: Continuation and bifurcation software for ordinary differential equations* .
- [24] A. Dhooge, W. Govaerts, Y. A. Kuznetsov, *MATCONT: a MATLAB package for numerical bifurcation analysis of ODEs*, *ACM Transactions on Mathematical Software (TOMS)* 29 (2) (2003) 141–164.

Chapter 5

Conclusion and future work

5.1 Summary

The research in this dissertation aims to study the escape dynamics in two degree of freedom systems in the presence of dissipative and gyroscopic forces. This dissertation presents a complete theoretical-computational framework that can deal with the motion between potential wells in both the conservative and dissipative systems.

In Chapter 2, we study the linearized dynamics of the escape in the system of an idealized ball rolling on both stationary and rotating surfaces. The analytical solutions of the transition boundary are obtained for both the conservative and dissipative systems. The results reveal that the transition tube and transition ellipsoid, which are the stable invariant manifold of a periodic orbit and a rank-1 saddle, govern the boundary of the initial conditions of a given energy for the trajectories that can escape from potential wells in the conservative and dissipative systems: the trajectories with initial conditions inside the boundary can escape, while the trajectories with initial conditions outside the boundary can not escape.

In Chapter 3, we extend the linearized dynamics of escape to the nonlinear case. We develop a bisection method applied to the snap-through buckling of a shallow arch. A two-mode Hamiltonian is developed for the shallow arch. Following the analysis in the rolling ball system, the analytical solutions for the systems can be obtained which will be used as approximations in the bisection method. By applying the bisection method, we can compute the transition boundary on a specific Poincaré section for both the conservative and dissipative systems. From the results, we find that an increase of the damping will reduce the transition boundary which corresponds to the amount

of the trajectories that can escape from the potential wells.

In Chapter 4, the boundary-value problem approaches are developed to study the transition boundary in the nonlinear system from the perspective of the invariant manifold of a periodic orbit and an equilibrium point in the conservative and dissipative systems, respectively. The results validate the transition tube and transition ellipsoid obtained from linear dynamics for the conservative and dissipative systems, respectively, in Chapter 2. The results show that the transition tube and transition ellipsoid in the nonlinear system do exist. Due to the nonlinearity considered in the system, the corresponding phase space structures do not appear as the standard forms obtained in the linear dynamics, but they are qualitatively the same.

5.2 Future work

Although this dissertation addressed some concerns in transition and escape dynamics, other concerns are still remaining. Based on the study in this dissertation, the following research directions are valuable to study.

In Chapter 4, we present a boundary-value problem approach to compute the transition boundary in the dissipative systems from the perspective of the invariant manifold. Initially, the problem is a two-parameter continuation. To simplify the computation, one Poincaré section should be considered to give an extra boundary condition, so that the problem can be reduced to a one-parameter continuation. However, if the input of the energy to the system is large, the transition ellipsoid will be distorted, special attention is needed to give proper Poincaré sections. To better capture the nonlinear transition ellipsoid, we might consider developing better two-parameter continuation strategies. Some set-oriented path following algorithms [1, 2, 3] can also be applied to compute the invariant manifold.

The theoretical-computational framework developed in this dissertation just works for the prediction of escape dynamics in two degree of freedom systems. Some studies [4, 5, 6] were carried out to compute the transition boundary in higher degree of freedom systems and algorithms were developed to study the escape dynamics in the conservative systems. However, the computational approaches dealing with dissipative systems are still lacking, not to mention what the phase space structures that govern the transition in the dissipative systems. Thus, the next future work can be focused on developing computational tools for computing the transition boundary in higher degree of freedom systems and establish the corresponding transition criteria in such systems.

Finally, this dissertation mainly focuses on the theoretical and computational aspects of the escape

dynamics. No experiments are implemented to prove the numerical results. Recently, an experiment [7] about a rolling ball on a four-well surface was carried out in which good agreement between the experiments and theory was observed. However, this experiment merely considers short-time dynamics, and the conservation of energy is considered. We still do not know what the situation is in long-time transition in the dissipative systems. Moreover, the experiment should be extended to structural mechanics, such as the snap-through of a shallow arch, to present experimental validation of the algorithms developed in this dissertation.

Bibliography

- [1] M. Dellnitz, A. Hohmann, The computation of unstable manifolds using subdivision and continuation, in: *Nonlinear dynamical systems and chaos*, Springer, 449–459, 1996.
- [2] M. Dellnitz, A. Hohmann, A subdivision algorithm for the computation of unstable manifolds and global attractors, *Numerische Mathematik* 75 (3) (1997) 293–317.
- [3] M. Dellnitz, O. Junge, On the approximation of complicated dynamical behavior, *SIAM Journal on Numerical Analysis* 36 (2) (1999) 491–515.
- [4] G. Gómez, W. S. Koon, M. Lo, J. E. Marsden, J. Masdemont, S. D. Ross, Connecting orbits and invariant manifolds in the spatial restricted three-body problem, *Nonlinearity* 17 (5) (2004) 1571.
- [5] S. Naik, V. J. García-Garrido, S. Wiggins, Finding NHIM: Identifying high dimensional phase space structures in reaction dynamics using Lagrangian descriptors, *Communications in Nonlinear Science and Numerical Simulation* 79 (2019) 104907.
- [6] S. Naik, S. Wiggins, Finding normally hyperbolic invariant manifolds in two and three degrees of freedom with Hénon-Heiles-type potential, *Physical Review E* 100 (2) (2019) 022204.
- [7] S. D. Ross, A. E. BozorgMagham, S. Naik, L. N. Virgin, Experimental validation of phase space conduits of transition between potential wells, *Physical Review E* 98 (2018) 052214.

Appendices

Appendix A

Derivations and coefficients for the rolling ball on a rotating surface

Substituting the surface function $H(x, y)$ defined in (2.12), one can obtain the Lagrangian equations from (2.15) as,

$$\begin{aligned}
 & I(1 + k_1^2 x^2) \ddot{x} + Ik_1 k_2 x y \ddot{y} + Ik_1^2 x \dot{x}^2 - 2I\omega \dot{y} + Ik_1 k_2 x \dot{y}^2 - I\omega^2 x + gk_1 x \\
 & + c_d [(1 + k_1^2 x^2) \dot{x} + k_1 k_2 x y \dot{y}] = 0, \\
 & Ik_1 k_2 x y \ddot{x} + I(1 + k_2^2 y^2) \ddot{y} + 2I\omega \dot{x} + Ik_1 k_2 y \dot{x}^2 + Ik_2^2 y \dot{y}^2 - I\omega^2 y + gk_2 y \\
 & + c_d [(1 + k_2^2 y^2) \dot{y} + k_1 k_2 x y \dot{x}] = 0.
 \end{aligned} \tag{A.1}$$

Once the Lagrangian system is obtained, one can transform it to the Hamiltonian system by use of the Legendre transformation defined in (2.18) which gives the generalized momenta,

$$p_x = \frac{\partial \mathcal{L}}{\partial \dot{x}} = \dot{x} - y\omega + H_{,x}^2 \dot{x} + H_{,x} H_{,y} \dot{y}, \quad p_y = \frac{\partial \mathcal{L}}{\partial \dot{y}} = \dot{y} + x\omega + H_{,x} H_{,y} \dot{x} + H_{,y}^2 \dot{y}, \tag{A.2}$$

and the Hamiltonian function,

$$\begin{aligned}
 \mathcal{H} = & \frac{1}{2(1 + H_{,x}^2 + H_{,y}^2)} [p_x^2 (1 + H_{,y}^2) - 2p_x p_y H_{,x} H_{,y} + p_y^2 (1 + H_{,x}^2) \\
 & + 2p_x \omega (y + x H_{,x} H_{,y} + y H_{,y}^2) - 2p_y \omega (x + y H_{,x} H_{,y} + x H_{,x}^2) \\
 & - (y H_{,x} - x H_{,y})^2 \omega^2] + gH,
 \end{aligned} \tag{A.3}$$

where p_x and p_y are the momenta conjugate to x and y , respectively, and the dependence of H on

x and y is understood.

The general form of Hamiltonian equations with damping is given by (2.21). For simplicity, the specific form of the Hamiltonian equations are not listed here. Following the same procedure as for the ball rolling on a stationary surface, we linearize the equations of motion around the equilibrium point at the origin which gives the linearized Hamiltonian equation as,

$$\begin{aligned} \dot{x} &= \omega y + p_x/I, & \dot{y} &= -\omega x + p_y/I, \\ \dot{p}_x &= -gk_1x + \omega p_y - c_d(\omega y + p_x/I), \\ \dot{p}_y &= -gk_2y - \omega p_x - c_d(-\omega x + p_y/I), \end{aligned} \quad (\text{A.4})$$

written in matrix form,

$$\begin{pmatrix} \dot{x} \\ \dot{y} \\ \dot{p}_x \\ \dot{p}_y \end{pmatrix} = \tilde{M} \begin{pmatrix} x \\ y \\ p_x \\ p_y \end{pmatrix} + \tilde{D} \begin{pmatrix} x \\ y \\ p_x \\ p_y \end{pmatrix}, \quad (\text{A.5})$$

where,

$$\tilde{M} = \begin{pmatrix} 0 & \omega & 1/I & 0 \\ -\omega & 0 & 0 & 1/I \\ -gk_1 & 0 & 0 & \omega \\ 0 & -gk_2 & -\omega & 0 \end{pmatrix}, \quad \tilde{D} = c_d \begin{pmatrix} 0 & 0 & 0 & 0 \\ 0 & 0 & 0 & 0 \\ 0 & -\omega & -1/I & 0 \\ \omega & 0 & 0 & -1/I \end{pmatrix}. \quad (\text{A.6})$$

The corresponding quadratic Hamiltonian is,

$$\mathcal{H}_2(x, y, p_x, p_y) = \frac{1}{2I} (p_x^2 + p_y^2) + \omega p_x y - \omega p_y x + \frac{g}{2} (k_1 x^2 + k_2 y^2). \quad (\text{A.7})$$

Using the same re-scaled parameters as in (2.23), the equations of motion can be rewritten in a re-scaled form as,

$$\begin{aligned} \dot{\bar{q}}_1 &= \omega \bar{q}_2 + \bar{p}_1, & \dot{\bar{q}}_2 &= -\omega \bar{q}_1 + \bar{p}_2, \\ \dot{\bar{p}}_1 &= c_x \bar{q}_1 + \omega \bar{p}_2 - c_h \omega \bar{q}_2 - c_h \bar{p}_1, \\ \dot{\bar{p}}_2 &= c_y \bar{q}_2 - \omega \bar{p}_1 + c_h \omega \bar{q}_1 - c_h \bar{p}_2, \end{aligned} \quad (\text{A.8})$$

which can be written in matrix form (2.58).

The characteristic polynomial of the matrix M , the conservative part of the dynamics, from (2.59), which appears in the linear ODE, (2.61), is,

$$p(\beta) = \beta^4 + (2\omega^2 - c_x - c_y) \beta^2 + \omega^4 + \omega^2 c_x + \omega^2 c_y + c_x c_y. \quad (\text{A.9})$$

Let $\alpha = \beta^2$, then the roots of $p(\alpha) = 0$ are as follows,

$$\alpha_{1,2} = \frac{1}{2} \left(c_x + c_y - 2\omega^2 \pm \sqrt{(c_x - c_y)^2 - 8(c_x + c_y)\omega^2} \right). \quad (\text{A.10})$$

For the parameters listed in (2.12), one can conclude that $\alpha_1 > 0$ and $\alpha_2 < 0$. Here we define $\lambda = \sqrt{\alpha_1}$ and $\omega_p = \sqrt{-\alpha_2}$. Now, we want to find the eigenvectors of M in (2.59) and use them to construct a symplectic linear change of variables which changes (2.61) into its simpler form (2.3). Denote the matrix $M - \beta I_4$ by M_β , then,

$$M_\beta = \begin{pmatrix} \bar{M}_\beta & I_2 \\ B & \bar{M}_\beta \end{pmatrix}, \quad \bar{M}_\beta = \begin{pmatrix} -\beta & \omega \\ -\omega & -\beta \end{pmatrix}, \quad B = \begin{pmatrix} c_x & 0 \\ 0 & c_y \end{pmatrix}, \quad (\text{A.11})$$

where I_k is the $k \times k$ identity matrix.

Substituting the complex eigenvalues $\pm i\omega_p$ as β into (A.11), one obtains a pair of complex eigenvectors with the form $u_{\omega_p} \pm iv_{\omega_p}$. Separating the real and imaginary parts, it gives two generalized eigenvectors,

$$\begin{aligned} u_{\omega_p} &= (0, \omega_p^2 + c_x + \omega^2, \omega\omega_p^2 - \omega c_x - \omega^3, 0), \\ v_{\omega_p} &= (-2\omega\omega_p, 0, 0, \omega_p^3 + \omega_p c_x - \omega^2\omega_p). \end{aligned} \quad (\text{A.12})$$

Moreover, the remaining eigenvectors associated with eigenvalues $\pm\lambda$ can also be obtained similarly,

$$\begin{aligned} u_{+\lambda} &= (\lambda^2 - c_y - \omega^2, -2\lambda\omega, \lambda^3 - \lambda c_y + \lambda\omega^2, -\omega\lambda^2 - \omega c_y - \omega^3), \\ u_{-\lambda} &= (-\lambda^2 + c_y + \omega^2, -2\lambda\omega, \lambda^3 - \lambda c_y + \lambda\omega^2, \omega\lambda^2 + \omega c_y + \omega^3). \end{aligned} \quad (\text{A.13})$$

Initially, we consider the change of variables defined in (2.29). To find out whether the matrix C is symplectic or not, we check $C^T J C = J$. After some algebra, we can find that,

$$C^T J C = \begin{pmatrix} 0 & \bar{D} \\ -\bar{D} & 0 \end{pmatrix}, \quad \bar{D} = \begin{pmatrix} d_\lambda & 0 \\ 0 & d_{\omega_p} \end{pmatrix}, \quad (\text{A.14})$$

where,

$$\begin{aligned} d_\lambda &= 2\lambda [(c_x - c_y - 4\omega^2)\lambda^2 - c_x c_y + c_y^2 - c_x \omega^2 - 3c_y \omega^2 - 4\omega^4], \\ d_{\omega_p} &= \omega_p [(c_x - c_y + 4\omega^2)\omega_p^2 + c_x^2 - c_x c_y - 3c_x \omega^2 - c_y \omega^2 - 4\omega^4]. \end{aligned} \quad (\text{A.15})$$

This implies that we need to apply some scaling on the columns of C in order to have a symplectic change. Since it can be shown that $d_\lambda > 0$ and $d_{\omega_p} > 0$, the scaling is given by the factors $s_1 = \sqrt{d_\lambda}$

and $s_2 = \sqrt{d_{\omega_p}}$. Thus, the final change is given by the symplectic matrix,

$$C = \begin{pmatrix} \frac{\lambda^2 - c_y - \omega^2}{s_1} & 0 & \frac{-\lambda^2 + c_y + \omega^2}{s_1} & \frac{-2\omega\omega_p}{s_2} \\ \frac{-2\lambda\omega}{s_1} & \frac{\omega_p^2 + c_x + \omega^2}{s_2} & \frac{-2\lambda\omega}{s_1} & 0 \\ \frac{\lambda^3 - \lambda c_y + \lambda\omega^2}{s_1} & \frac{\omega\omega_p^2 - \omega c_x - \omega^3}{s_2} & \frac{\lambda^3 - \lambda c_y + \lambda\omega^2}{s_1} & 0 \\ \frac{-\omega\lambda^2 - \omega c_y - \omega^3}{s_1} & 0 & \frac{\omega\lambda^2 + \omega c_y + \omega^3}{s_1} & \frac{\omega_p^3 + \omega_p c_x - \omega^2 \omega_p}{s_2} \end{pmatrix}. \quad (\text{A.16})$$

By using the change of variables with the symplectic matrix in (A.16), one obtains the Hamiltonian equations written in the simple standard form (2.3) with the Hamiltonian function in a normal form (2.1) whose solutions are given in (2.4). The corresponding results and discussion can be found in Section 2.2 which will not be repeated here.

Some coefficients. The parameters in equation (2.67) are,

$$\begin{aligned} a_p &= \frac{s_2^2 \left[(1 + c_x)^2 + \lambda^2 \omega_p^2 \right]}{8\omega_p (1 + c_x)^2 (\lambda^2 + \omega_p^2)}, \\ b_p &= \frac{s_2^2 \left[(1 + c_x)^2 \left(\bar{q}_2^0 - (-1)^i \bar{q}_1^0 \lambda \right) - (-1)^i \lambda \omega_p^2 \left(\bar{q}_1^0 + \bar{q}_1^0 c_x + (-1)^i \bar{q}_2^0 \lambda \right) \right]}{4\omega_p (1 + c_x)^2 (\lambda^2 + \omega_p^2)}, \\ c_p &= \frac{s_2^2 \left[(1 + c_x)^2 \left(\bar{q}_2^0 - (-1)^i \bar{q}_1^0 \lambda \right)^2 + \omega_p^2 \left(\bar{q}_1^0 + \bar{q}_1^0 c_x + (-1)^i \bar{q}_2^0 \lambda \right)^2 \right]}{8\omega_p (1 + c_x)^2 (\lambda^2 + \omega_p^2)} - h. \end{aligned} \quad (\text{A.17})$$

Here $i = 1, 2$ are for stable ($q_1^0 = 0$) and unstable ($p_1^0 = 0$) asymptotic orbits, respectively.

The matrix K from (2.71) has components given as follows,

$$\begin{aligned} K_{11} &= \frac{2}{S} - \frac{1}{2}, & K_{12} &= -\frac{1 + c_y}{S\lambda} \sqrt{\frac{2(1 + c_x)}{\lambda\omega_p}}, & K_{13} &= \frac{c_y - c_x}{2S}, \\ K_{14} &= \sqrt{\frac{2\omega_p(1 + c_x)}{S^2\lambda}}, & K_{21} &= \frac{\lambda}{S} \sqrt{\frac{2\omega_p\lambda}{1 + c_x}}, & K_{22} &= -\frac{1}{2} + \frac{c_x - c_y - 4}{2S}, \\ K_{23} &= K_{21}, & K_{24} &= 0, & K_{31} &= K_{13}, & K_{32} &= K_{12}, & K_{33} &= K_{11}, & K_{34} &= -K_{14}, \\ K_{41} &= -\frac{1}{S} \sqrt{\frac{2\lambda(1 + c_x)}{\omega_p}}, & K_{42} &= 0, & K_{43} &= -K_{41}, & K_{44} &= -\frac{1}{2} - \frac{c_x - c_y + 4}{2S}, \end{aligned} \quad (\text{A.18})$$

where,

$$S = \sqrt{(c_x - c_y)^2 - 8(c_x + c_y)}.$$